NASA Contractor Report 3844

Deformation Measurements of Composite Multi-Span Beam Shear Specimens by Moire Interferometry

Daniel Post, Robert Czarnek,
Duksung Joh, and Judy Wood

GRANT NAG1-359
NOVEMBER 1984

NASA Contractor Report 3844

Deformation Measurements of Composite Multi-Span Beam Shear Specimens by Moire Interferometry

Daniel Post, Robert Czarnek,
Duksung Joh, and Judy Wood
Virginia Polytechnic Institute and State University
Blacksburg, Virginia

Prepared for
Langley Research Center
under Grant NAG1-359

National Aeronautics
and Space Administration

**Scientific and Technical
Information Branch**

1984

CONTENTS

ABSTRACT

Experimental analyses were performed for determination of in-plane deformations and shear strains in unidirectional and quasi-isotropic graphite-epoxy beams. Forty-eight-ply beams were subjected to 5-point and 3-point flexure. Whole-field measurements were recorded at load levels from about 20% to more than 90% of failure loads.

Contour maps of U and W displacement fields were obtained by moire interferometry, using reference gratings of 2400 lines/mm or 60,960 ℓ/in. Clearly defined fringes with fringe orders exceeding 1000 were obtained. Whole-field contour maps of shear strains were obtained by a method developed for these tests.

Various anomalous effects were detected in the displacement fields. Their analysis indicated excess shear strains in resin-rich zones in regions of shear tractions; free-edge shear strains in quasi-isotropic specimens in regions of normal stresses; and shear stresses associated with cyclic shear compliances of quasi-isotropic plies in regions of shear tractions. Their contributions could occur independently or in superposition.

Qualitative analyses addressed questions of relaxation; influence of contact stress distribution; specimen failure; effect of specimen overhang; nonlinearity; and qualities of 5- and 3-point flexure tests.

INTRODUCTION

The objective of this research was detailed measurement of deformations and shear strains in graphite-epoxy beams. The investigation is a continuation of the study of Williams and Rhodes [1] in which they determined that multi-span beam shear test results correlate well with damage tolerance trends found by impact tests. Forty-eight-ply specimens were subjected to 5-point and 3-point flexure. Unidirectional 0° and quasi-isotropic laminates were tested. In-plane displacements of the free edge were measured by high-sensitivity moire interferometry, using reference gratings of 2400 lines/mm (60,960 ℓ/in.). Whole-field displacement patterns were recorded for a series of load levels up to nearly the failure load.

A special method was developed to produce whole-field contour maps of shear strains. Shear strain contours were exhibited for each specimen. In addition, conventional methods were used to determine shear strains along selected lines for various load levels. Nonlinear behavior was observed.

Various anomalous effects were observed and interpreted. Experimental analysis of these geometries and materials was reasonably comprehensive and provides data for specimen assessments and for comparison of theoretical analyses.

SPECIMEN AND LOADING

Table I specifies the specimen material, stacking sequence, dimensions, loading and failure load for each of the six specimens analyzed in these experiments. The specimens were provided by NASA Langley Research Center, cut to finished length and width. Their surfaces were made flat and parallel at VPI&SU by surface grinding. Only the minimum thickness necessary to assure flat planes in the loading zones was removed from each side; however, more than one ply was ground off each side in some parts of the specimens.

Figure 1 illustrates the loading conditions for the three specimen sizes. The horizontal distance between each loading point was 0.50 in. (13 mm), or about twice the specimen thickness. Loads were applied by hardened steel rods of 0.250 in. (6.35 mm) radius. Tiny flats were ground on the rods at their horizontal tangents to assure that their contact zones on the specimen were coplanar.

Figure 2 illustrates the loading fixture designed for these experiments. Loads were applied by turning the screw to translate the upper wedge horizontally. The lower anvil rests on a hardened steel ball to accommodate any slight non-parallelism of the specimen surfaces. The fixture is steel, 1 in. (25 mm) thick; the wedges are hardened. Electric resistance strain gages were applied to the narrow columns and used to indicate the total load on the specimen. Two gages, one with vertical filaments and one with horizontal filaments were cemented to each side of each column. For each column, the gages were wired to a 4-arm bridge in such sequence that temperature and bending effects are cancelled. The fixture was calibrated to 11,000 pounds (48.9 kN) in a 20,000 pound (89 kN) Instron testing machine. Output from each column was read separately to ascertain whether the loads were applied symmetrically to the specimens. The loading fixture was fabricated and strain gaged by NASA Langley Research Center.

MOIRE INTERFEROMETRY

Moire interferometry is a whole-field optical method using coherent laser light to measure in-plane displacements. A comprehensive description appears in Ref. 2. Briefly, a high frequency crossed-line diffraction grating is replicated on the specimen surface using a special mold, as illustrated in Fig. 3. The result is a thin --0.001 in. (0.025 mm)-- reflective phase grating firmly adhered to the specimen, which deforms together with the

specimen surface. The specimen grating is observed in an optical arrangement illustrated in Fig. 4. Two beams of light incident at angles α and $-\alpha$ form a virtual reference grating. Its frequency is $f = (2 \sin \alpha)/\lambda$, where λ is the wavelength of the light. This reference grating interacts with the specimen grating to form the two-beam interference pattern viewed in the camera. The pattern is a contour map of displacements governed by the relationship

$$U = \frac{1}{f} N_x \tag{1}$$

where U is the in-plane x-component of displacement at any point, and N_x is the fringe order at that point in the fringe pattern, obtained when the reference grating lines are perpendicular to the x-axis.

In this work, the grating was applied in the xz plane with lines perpendicular to the x- and z-axes. In-plane displacements, W, in the z-direction are obtained from fringe orders, N_z, obtained from the orthogonal grating by

$$W = \frac{1}{f} N_z \tag{2}$$

Frequency f was 60,960 lines/in. (2400 ℓ/mm), which gave a sensitivity of U and W measurements of 16.4 μin. (0.417 μm) per fringe order. An argon ion laser was used at wavelength 20.3 μin. (0.514 μm) and 100 mW power. The optical arrangement used in these experiments had two additional mirrors which were used to produce a virtual reference grating perpendicular to that of Fig. 4; individual patterns of N_x or N_z were obtained by blocking the light of the alternate virtual reference grating.

SHEAR STRAIN CONTOURS

A method developed in the course of this work to determine shear strain contours is reported in Ref. 3. For small strains, shear strain γ_{zx} is

related to displacements U and W by

$$\gamma_{zx} = \frac{\partial U}{\partial z} + \frac{\partial W}{\partial x} \approx \frac{\Delta U}{\Delta z} + \frac{\Delta W}{\Delta x} \qquad (3)$$

The finite interval form shown at the right is an approximation. It is an approximation in the same sense that strain gages, and also the computational finite element method, approximate conditions at a material point. The method depends, firstly, on an optical technique to obtain whole-field fringe patterns of the cross-derivatives; it is called mechanical differentiation [3]. It depends, secondly, on the fact that contours of the sum of the index numbers of two systems of parametric curves can be drawn through their intersections (see Fig. 5). Figures from Ref. 3 will be instructive for this report and they are duplicated here. Figure 6 illustrates the specimen and loading conditions used in that work. The specimen was an isotropic beam of epoxy. Note that the in-plane coordinates are designated x and y in Ref. 3 and in these excerpts, and the corresponding displacement components are U and V. Fringe patterns of N_x and N_y are shown in Fig. 7 for a small applied load. Figure 8 shows the result of mechanical differentiation, using displacement patterns for a load about 7 times greater. They represent the cross-derivatives of Eq. 3 since $\Delta U = (1/f)\Delta N_x$, etc.; finite increments Δx and Δy were 0.010 in. (0.25 mm). These contours are traced and overlaid in Fig. 9, where their fringe orders, or index numbers, are labeled. Curves were drawn through each series of intersections for which the sum of index numbers is a constant, 0, 1, 2, ..., with the result shown in Fig. 10. The bold curves are contours of the sum of the cross-derivatives. They are contours of shear strain γ_{xy} when their numerical values are multiplied by $1/(f\Delta x)$, or 0.00167 m/m. At the center of the bay, where the contour number is 5.5, the shear strain is 0.0092 m/m.

Mechanical differentiation can be applied, too, for direct derivatives and contours of normal strains. Patterns of ε_x and ε_y are shown in Fig. 11 for the identical state of deformation as Fig. 10. The same multiplication factor applies. The maximum tensile strain in the lower right corner is ε_x = 4.2 x 0.00167 or 0.0070 m/m.

EXPERIMENTAL PROCEDURE

A preliminary series of tests was performed on one each of the six types of specimens to measure their failure loads. These values were used as expected failure loads for the subsequent tests.

For each subsequent test, a high-frequency crossed-line grating was applied to the specimen edge. The specimen was installed in the loading frame, the first load increment was applied and photographs of the two displacement fields, two cross-derivatives and two direct derivatives were taken for one bay adjacent to the central load. The applied load was increased in a series of steps and the same series of photographs was taken for each step, except the derivative patterns were omitted for the highest load levels. The planned load steps were approximately 40, 80 and 90% of the expected failure load for each specimen; 20% loads were added for four specimens. Each specimen was loaded to failure and the failure load, P_f, is reported in Table I. The load steps for each specimen, normalized against the actual failure loads, can be deduced from a graph of shear strain vs. load, which is presented later in Fig. 19.

The U and W patterns and the derivative patterns were photographed at a magnification of 5.5X. Only a small but important portion of the beam appeared in these photographs. In addition, photographs of U and W patterns were made at 2X magnification for all but the highest load levels. These

showed at least half of each specimen, extending to one end of the specimen in every case.

The derivative patterns were optically filtered to enhance their contrast.

RESULTS

The primary results are shown in Figs. 12a-j through 17a-j. These figures are compiled in Table II, which shows that a separate figure number pertains to results from each of the six specimens. The figure letters, e.g. 12a,b,c,d,e,f,g,h,i,j, pertain to specified fringe patterns, graphs or contour maps for the corresponding specimen. The load level for each figure is given by the numbers in Table II, where the load is shown as a percentage of the failure load. All the figures except those of column c show results for the region or bay adjacent to the central load. This bay is indicated by the dashed box in the figures of column a, Figs. 12a, 13a, --- 17a. Vertical lines seen in the fringe patterns (except those of Fig. 12) are index lines scribed on the specimen at positions approximately in line with the loading points.

The U and W fringe patterns exhibit anomalous effects, manifest as irregular (non-smooth) fringes, which will be discussed later. These irregularities were smoothed for the shear strain contour maps and graphs in Figs. 12-17. They do not show the actual behavior at each point in the specimen, but instead, they show average behavior wherein data was integrated across a broad zone surrounding each point. Periodic anomalous effects are especially noticeable for the quasi-isotropic specimens and severe smoothing was performed on the data.

Contours of γ_{zx} were obtained from the mechanical differentiation photographs using Δz (and Δx) = 0.010 in. (0.25 mm), except for Fig. 16d

where the increment was only 0.005 in. (0.013 mm). Fewer contours appear in Fig. 16d for this reason; the scale for ΔN_{x+z} in Figs. $16e_1$ and $16e_2$ differs from that in other corresponding figures for the same reason. The shear strain graphs (column e) were determined from data taken directly from U and W fringe patterns. Fringe gradients $\Delta N_x/\Delta z$ and $\Delta N_z/\Delta x$ were obtained from measurements on the U and W photographs, either by counting the fringes that cross an increment Δz (or Δx), or by measuring the distance between a given number of fringes. The symbol ΔN_{x+z} in Figs. 12-17e is meant to represent $\Delta N_x + \Delta N_z$, which for $\Delta x = \Delta z$, is proportional to γ_{zx}.

Figure 18 shows the graph of γ_{zx} across the quasi-isotropic specimen of Fig. 16, but here the periodic anomalous effect was not smoothed. Dramatic undulations of shear strains are evident.

In addition to these graphs, data was taken at the center point of the bay from U and W patterns for all the load levels recorded. Clear fringe patterns were obtained with much greater density of fringes than shown here, for loads within a few percent of failure. The results are given in Fig. 19, normalized with respect to failure loads. The points plotted for $P/P_f = 0$ were obtained by noting on non-normalized graphs of γ_{zx} v.s. P (not included here) that the curves were linear between zero and the first load level. Accordingly, these two points must lie on the same horizontal line in the normalized graph.

Figure 20 shows photographs of the six specimens after failure. Figure 21 shows microphotographs of a cross-section of the unidirectional specimen that had been subjected to 5-point bending; the section was from an unbroken portion of the specimen near the overhang. The microphotographs will be used to support the explanation for anomalous features seen in the fringe pattern of Fig. 12a for the same specimen.

ANALYSIS

I. Force Distribution, Approximate

Traditional moment and vertical shear diagrams are drawn in Fig. 22 for the 5-point and 3-point beam loadings. Being statically indeterminant, load distributions on the 5-point beams are not known a priori. The moment diagram was drawn, however, after noting that $\varepsilon_x = 0$ (and $\sigma_x = 0$) occurs at about 41% and 45% of the bay length from the central load, for the unidirectional and quasi-isotropic specimens, respectively. These positions are denoted by A-A in Figs. 12a and 15a; they are easily determined from the corresponding U-displacement fields as the locations along the extreme fibers where the fringes are horizontal, i.e., where $\partial U/\partial x = 0$. At Section A-A, the bending moment is zero and the problem becomes statically determinant. The loads were apportioned accordingly and, to a first approximation, the diagrams are in proper scale. The central load is about 3.5 times the outermost loads. The scale for the 3-point beam is drawn for equal maximum vertical shear, which prescribes that the central loads be equal for the 3-point and 5-point configurations.

II. Anomalous Effects

A. Resin-Rich Zones

1. Observations

Zig-zag and nearly discontinuous U-displacement fringes can be seen in Fig. 12a. These represent real effects, as distinguished from noise in the experimental technique. Extremely narrow horizontal fringes appear in a large region of the bay. They will be called striations. The striations are responsible for the zig-zag and irregular appearance of fringes in the pattern. Referring to Fig. 12d, it is clear that the striations do not occur

in regions where shear strain γ_{zx} is zero, and their incidence is sparse where γ_{zx} is small. They profilerate where γ_{zx} is moderate and large.

The striations represent abrupt changes in U-displacements. Careful inspection shows that $\Delta U/\Delta z$ is positive across all these abrupt changes. This is consistent with the direction of internal shear forces -- or shear stresses τ_{zx} -- that occur on all horizontal planes in this region, as illustrated in Fig. 23.

2. Explanation

An argument for the occurrance of the striations depends on the existence of thin resin-rich layers between the graphite-epoxy plies of the laminate. The explanation calls for non-constant thickness of the resin-rich layers, wherein thickness may vary along any given layer and thicknesses may be different from layer-to-layer.

Under these circumstances, thin horizontal layers of relatively high compliance material exist in the laminate. Their deformation in response to the horizontal shear stresses is much greater than that of the surrounding stiffer composite material. Large horizontal displacements (U) occur in these resin-rich layers in comparison to those in the composite plies.

In the composite plies, the displacement gradient $\Delta U/\Delta z$ may be positive or negative, as seen in Fig. 12a, in response to the combination of normal and shear stresses in any region. The finding that shear strain component $\Delta U/\Delta z$ in the compliant layer is always positive indicates that the striations are generated by the shear stresses, with little influence from the normal stresses, and also that the strains in the compliant layers are much larger than the strains in the composite layers.

Consistent with this explanation, the high shearing deformation in resin-rich zones must be an effect that exists throughout the width of the specimen,

not merely on its free edges. The through-the-thickness shear modulus of the laminate must be substantially reduced by the resin-rich layers, compared to the modulus of a hypothetical uniform plate with properties equal to these at the interior of the composite plies. Whether the shear modulus of the laminate is also degraded in comparison to a hypothetical plate with the same overall content of fiber and matrix uniformly distributed throughout the plate cannot be inferred.

The transverse displacements, W, are not measureably affected by the resin-rich layers, as seen in Fig. 12b. Similarly, the resin-rich layers do not affect deformations caused by normal stresses σ_x and σ_z. This is inferred from the smoothness of fringes in Fig. 12a in certain regions, that is, where γ_{zx} is zero or small but where normal strains and stresses are large. Such regions occur at the left end of the bay and near the horizontal edges of the specimen, where striations are absent.

3. Corroboration

A chart was made of the position of each clearly defined striation in Fig. 12a. Striations at 24 different levels were observed and they were found to lie at regularly spaced intervals, concentrated in the central region where the shear strains were large.

The average ply thickness was determined by dividing 48 plies into the (average) original specimen thickness given in Table I. The ply thickness was determined as 0.00569 in. (0.145 mm) and 45.3 plies were determined to lie in the finished specimen thickness. When the height of the pattern of Fig. 12a was divided by 45.3, the equivalent (average) ply thickness on the photograph matched the average interval between striations within 2%.

Dramatic corroboration of the existence of resin-rich layers between plies in the specimen of Fig. 12a is seen in the microphotographs of Figs. 21a and b. These compliant layers vary in thickness and the change of U across the layer depends upon the layer thickness as well as the shear tractions. The striations vary correspondingly.

4. Generality

The unidirectional specimens of Figs. 13a and 14a exhibit striations in the areas of high shear strains, too. They are less profuse than the striations of Fig. 12a, which indicates that there were fewer resin-rich layers in these specimens. As before, their spacing matches the ply spacing. The quasi-isotropic specimen of Fig. 15a also exhibits some features that appear to be striations, although other anomalous features of quasi-isotropic laminates make the observation inconclusive. The quasi-isotropic specimens of Figs. 16a and 17a do not show a significant number of features that could be interpreted as striations. If horizontal striations exist in these patterns, they are masked by other anamolous effects.

Evidence for the existence of high shear strains γ_{zx} in very narrow resin-rich layers is compelling. They occur in regions of shear tractions and they are independent of normal tractions. This applies to unidirectional laminates. For quasi-isotropic laminates, the evidence in these tests is inconclusive.

B. Anomalous Fringe Features in Quasi-Isotropic Specimens

1. Observations

The quasi-isotropic specimens exhibit U-displacement fields that have a strong cyclic component. At the left end of the bay in Fig. 15a, below the central load where nominal loading symmetry exists, the zero fringe and its

neighbors exhibit an anomalous waviness. The same is true in Figs. 16a and 17a. The waves have a period equal to the width of 4 plies -- the group of 45°, 0°, -45° and 90° plies. Elsewhere in Figs. 16a and 17a the waviness degenerates into a cyclic alternation of more closely and less closely spaced fringes; the cyclic period of 4 plies thickness persists. The shear strain distribution of Fig. 18 is a manifestation of this anomaly.

Spot checks of Fig. 17a showed that normal strain ε_x was independent of the waviness. Smooth curves were obtained from plots of $\Delta N/\Delta x$ vs. z. While the waviness may give a different impression, the horizontal distances between more closely and less closely spaced fringes is a smooth function of vertical distance z.

2. Free-Edge Effects

A strong component of the cyclic variations of shear strains γ_{zx} appears to be free-edge effects of the type known in tension specimens [4,5]. Figure 24 is an example of the U-displacement field on the free edge of an angle-ply laminate in tension. Similar effects exist in quasi-isotropic laminates. It is shown in Ref. 5 that the interlaminar shear strain γ_{zx}, for the tensile specimen, is related to the fringe pattern and normal strain ε_x by

$$\gamma_{zx} = \varepsilon_x \tan\phi \tag{4}$$

where ϕ is the angle of the tangent to the fringe (in Fig. 24) at the interface between nonparallel plies, where the angle is measured with respect to the z axis. Equation 4 depends only on the condition that ε_x and γ_{zx} are independent of x.

This condition is satisfied at the vertical centerline of the bending specimens and consequently, Eq. 4 applies there, too. Well formed free-edge effect fringes appear in the lower-left zones of Figs. 15a and 16a; they are

less well formed in Fig. 17a because the U-displacement field is not sufficiently symmetrical in that figure*. They do not extend into the upper-left zones because of the local disturbance introduced by the applied load. Measurements of ϕ and ε_x ($\approx \Delta U/\Delta x$) from Fig. 16a in the lower-left corner permit calculation of γ_{zx} by Eq. 4. Results of this calculation at several angle-ply interfaces were found to agree reasonably well with values of γ_{zx} calculated by Eq. 3.

The interlaminar shear strains attributable to free-edge effects persist in multidirectional laminates wherever ε_x is nonzero. Topography of the contour map of U-displacements will change, however, as the result of additional strains and rigid body rotations. This combination of effects leads to the cyclic alternation of more closely and less closely spaced fringes elsewhere in the quasi-isotropic specimens.

Shear strains γ_{zx} attributable to free edge effects are caused by mismatch of material properties in adjacent layers, in the presence of axial strain ε_x. These shear strains are confined to a narrow volume of material. They occur at the free edge, but attenuate rapidly and become zero in the interior of the specimen [4,5]. While γ_{zx} may be quite large at the free edge, most of the interior volume of the specimen is free of shear strains caused by ε_x (or σ_x), i.e., shear strains attributable to free edge effects.

The undulations of γ_{zx} in Fig. 18 is partly caused by free edge effects, but not entirely. Free edge shear strain γ_{zx} should be zero on the neutral axis of the beam, where $\varepsilon_x = 0$. Figure 18 shows the undulations decreasing in magnitude near the center of the beam, but remaining unmistakably nonzero.

* Comparison of Figs. 17a and c show that rigid body rotation was inadvertently introduced in Fig. 17a. With the optical system employed here, this does not influence determination of shear strains; fringe gradients $\partial U/\partial z$ and $\partial W/\partial x$, caused by specimen rotation, have opposite signs and cancel in the calculation of shear strains.

The cyclic shear strains in this zone is attributed to cyclic shear compliance, discussed in the following section.

3. Cyclic Shear Compliance

Cyclic variations of fringe orders are evident in Figs. 15a, 16a and 17a near the center of the respective bay, i.e., in the region surrounding the intersection of vertical and horizontal centerlines. These anomalous effects are caused, according to the present hypothesis, by cyclic variations of shear compliances of the layers of the quasi-isotropic laminate.

The diagram of Fig. 23 applies for this central region; shear stresses τ_{zx} are generated in response to the external forces. These shear stresses may reasonably be assumed to be nearly constant in this region, varying slowly with z and x coordinates. The constitutive equation for shear at the free edge of the specimen, where shear stress τ_{yz} is zero, is

$$\gamma_{zx} = \frac{\tau_{zx}}{G_{zx}} \tag{5}$$

for the problem under consideration. Thus, the cyclic variation of shear strain shown in Fig. 18 should correspond, near the midplane, to the variation of $1/G_{zx}$.

In quasi-isotropic laminates, the shear modulus G_{zx} of individual layers varies from a maximum for 0° layers to a minimum for 90° layers; it has an intermediate value for ± 45° layers. Figure 18 indicates that, near the center of the bay, the maximum shear strain is greater than the minimum value by a factor of 1.52. The explanation, according to the present hypothesis, is that the ratio of maximum to minimum shear moduli, G_{zx}, is also 1.52. This requires that G_{zx} for 0° layers is 1.52 times that for 90° layers.

Published values of G_{zx} for 0° and 90° layers are scarce. Only one reference has been found [6] for graphite-epoxy T300-5208. This provided a ratio of 1.95, or 22% higher than 1.52. The deviation is acceptable, however, when two factors are considered: the published values come from ultrasonic measurements, which are thought to be less dependable than mechanical measurements; and the fiber volume fractions for the specimens of Ref. 6 and the current beam shear specimens might not have been equal to each other.

Figures 16 and 18 pertain to the same specimen. Because the average shear strains along B-B in Fig. 16d are largest at the midplane and diminish toward the top and bottom of the specimen, the contribution of cyclic shear compliance is largest at the midplane. It reduces to zero at the top and bottom, but there, the contributions from free edge effects are largest and reduce to zero at the midplane. This explanation is satisfactory to explain the results of Fig. 18.

Corroborating evidence for a relationship between shear strain undulations and cyclic shear compliance was found in Fig. 15a. Figure 25 shows a graph of fringe order across the vertical section A-A of Fig. 15a, the section where ε_x is zero at the top and bottom. Normal strain ε_x is nearly zero across the entire line and it is assumed it would be exactly zero in the absence of anomalous effects. The graph of Fig. 25 shows a cyclic variation of $\Delta N_x/\Delta z$ (or $\partial U/\partial z$) near the center. (Higher frequency disturbances in Fig. 25 appear to be the effect of striations and they are disregarded in favor of the dashed portion of the curve.) Since $\gamma_{zx} = \partial U/\partial z + \partial W/\partial x$ (Eq. 3), and since $\Delta N_z/\Delta x$ (or $\partial W/\partial x$) is seen in Fig. 15b to be constant in this region, the graph of Fig. 25 prescribes cyclic variations of γ_{zx}. Considering that two 90° plies lie at the center of the symmetrical laminate, periods of $\delta_1 = 4$ plies and $\delta_2 = 4.5$ plies thickness are required for corroboration. Figure 25

gives that result with remarkable fidelity. In addition, the magnitude of the shear undulation corresponding to these cyclic U-displacements was calculated. The average of maximum gradients $\Delta N_x/\Delta z$ of waves in Fig. 25 was used; seven gradients were averaged. The result gave an undulation $\Delta\gamma_{zx}$ of 0.0044 m/m. While this is in remarkable agreement with that needed to explain the excess cyclic shear strains at the center of Fig. 18, the measurements for Figs. 18 and 25 are from different specimens. The result means that rough agreement is achieved.

The undulations in Fig. 25 do not represent free-edge effects, because $\varepsilon_x \approx 0$ in this region. They are explained as the result of cyclic variations in shear compliance; they corroborate the hypothesis of the existence of cyclic shear compliance effects in Fig. 18, where $\varepsilon_x \neq 0$. Taken in total, the evidence offers a compelling argument for the hypothesis that undulating shear strains in regions of strong shear tractions are caused by cyclic shear compliance of the material.

The cyclic variations observed on the free edge in Fig. 25 extend through the width (y-direction) of the specimen. In Fig. 18, too, the shear strain undulations that occur at the free edge near the midplane of the specimen extend through the width of the specimen.

C. Summary of Anomalous Effects

Striations occur in unidirectional composites subjected to shear tractions applied parallel to the ply surfaces. They indicate localized zones where shear strains γ_{zx} significantly exceed those in the surrounding region. They are caused by thin layers of compliant resin-rich material between the plies. Normal stresses and strains do not cause or contribute to the striations, i.e., to the excess shear strains. Only a few striations were

observed in the quasi-isotropic laminates under shear tractions and their interpretation is inconclusive.

Quasi-isotropic laminates exhibit free-edge effects in zones of normal strains ε_x acting parallel to the plies. In 3- and 5-point bending, they contribute large shear strains γ_{zx} near the extreme fibers of the beam, and none at the neutral axis. In addition, cyclic variations of shear compliance of the plies contributes large shear strains γ_{zx} near the neutral axis, where shear tractions are large. Excess shear strains from the anomalous effects of striations and cyclic shear compliance do not occur exclusively near the free edge of the beam. They occur, too, through the interior of the specimen. Shear strains caused by free-edge effects are largest at the free edge, but attenuate rapidly to zero in the interior of the beam.

III. RELAXATION

For all specimens, the load relaxed with time after load application. Near 40% of failure load, the drop in load during the first hour was in the range of 1 to 3% of the initial load. Near 80% of failure load, the load relaxed by a few percent in the first minute. After 10 minutes, relaxation diminished to roughly 2% per hour.

Superposition of photographic negatives of W-displacement fields showed extremely small changes of displacements with time. The specimen of Fig. 13 showed a change of W of 1 fringe order in the bay in the interval of 3-29 minutes after load application. The load dropped 1.8% in the same interval. This was at 38% of failure load. At 85% of failure load, the change of W was about 10 fringes in the interval from 4 to 40 minutes after loading; the load dropped 4% in the same interval. It is clear from Fig. 13b that these changes of deformation represent tiny fractions of the total specimen deformations.

Similarly, for the specimen of Fig. 16 at 85% of failure load, the decrease of W was 2 1/2 fringes in a 2 minute interval, while the drop in load was 1.5%. The sign of W displacement changes was analyzed, and it was confirmed that the deformation decreased with time. The percentage relaxation of load was several times greater than the percentage relaxation of deflection.

The loading fixture was very stiff. Displacement attributable to the narrow columns is about 1 fringe per 100 pounds (0.45 kN) change of load. Other elastic deformations would be small. Some creep of the lubricants is possible, but since substantially higher loads were applied prior to these measurements, excess lubricant had probably already escaped and the lubricant film had probably reached a fixed thickness. This probability is corroborated by the disproportionately small decrease in specimen displacements with decrease in loads.

Progressive crushing of material at the contact zones (occurring at a nominally fixed load) would be accompanied by substantial decreases of the specimen deformation. Since this did not occur, the load relaxation is attributed primarily to nonlinear properties of the composite material.

IV. EFFECT OF CONTACT STRESSES

The contour maps of Figs. 12-17d show that (averaged) shear strains γ_{zx} are not largest at the center of the bay, but instead, they are largest in the region of influence of the contact stresses near loading points. It may be possible to reverse this condition and establish maximum shear strains at the center of the bay.

Figure 10 suggests one possible approach for reducing the shear stresses near the points of load application. The shear strain does not peak near the central load. In this case, shallow cylindrical recesses were machined in the

specimen to engage the cylindrical loading bars (Fig. 6). It appears that this was successful in distributing the contact pressures at the center load sufficiently well to avoid high shear strains in the surrounding region. The recess was not successful in avoiding high shear strains, however, in the lower-right corner. This is thought to result from movement of the deformed specimen that shifted the recess laterally and prevented the recess from distributing the contact pressures.

Redesign of the contact conditions is suggested for distributing contact pressures. One possibility is the arrangement shown in Fig. 26 in which steel plates engage the specimen to spread the contact zone and steel rollers minimize horizontal components of forces that would otherwise be introduced by friction. Additional tests are required to determine whether peak shear strains could be restricted to the center of the bay. In this ideal condition, the contour of largest γ_{zx} would be a closed loop surrounding the center point of the bay.

V. SPECIMEN FAILURE

All failures showed limited local crushing near the zones of load applications, but the load carrying capacity was not seriously diminished by this damage. Generalized specimen failure occurred at the maximum load level, P_f. It was characterized by cracks spreading across the specimen parallel to the plies. Figure 20 shows the distribution of cracks, which suggest shear failures. The unidirectional 5-point beam (Fig. 20a, top) was cut apart and the fracture surface showed matrix failure without apparent fiber damage.

A possible scenario of the failure process is as follows. A crack developed at a point 10 to 25% below the central load and to the left or right of center. As seen, for example, in Figs. 12d, i and j, the shear strain γ_{zx}

was higher at that location than at the center, normal strain ε_x was positive, and normal strain ε_y was compressive. Although even larger shear strains were present closer to the point of load application, the compressive strains ε_y may have impeded nucleation of a crack. Even if nucleated, a shear crack might not tend to propagate in zones very close to the top of the beam, because there the average shear strains diminish rapidly with horizontal distance from the loading point. The crack propagated to the end of the bay and arrested (Fig. 20b, top) in the zone of relatively low shear strain. Subsequently, with further displacement of loading points of the loading fixture, the crack continued to propagate to the end of the specimen. Additional displacement of the loading points generated and propagated more cracks, each initiating in a new zone of high shear in the (weakened) specimen.

In this scenario, the free-edge effects in quasi-isotropic laminates can play an important role, because failures begin 10 to 25% below the central load, where ε_x is significant. As a result of free-edge effects in normal strain regions, γ_{zx} is elevated on the free surfaces and adds an extra contribution to shear strains otherwise present. Failures would be expected to initiate and propagate first along the free surface and then propagate into the interior.

VI. EFFECT OF OVERHANG

Figure 1 shows the geometrical configurations of these specimens, wherein two geometries have long overhangs. While a long overhang might be assumed to reduce shear strains in the specimen, the results show minimal effect -- at least for the lower load levels up to about 40% of failure loads.

Figures 12c, 13c, 15c and 16c show that fringes of the U-displacement field rapidly become parallel and uniformly spaced as they proceed away from the main body of the specimen and into the overhang. This means that a state of zero strain and stress is rapidly attained, and only rigid body rotation remains. Figures 14c and 17c show that an overhang of half the specimen thickness is not quite adequate to assure uniformly spaced fringes at the ends. Some modest strains remain to the right of the loading point. This is seen, too, from the shear strain contours of Figures 14d and 17d. However, these are not qualitatively different from the shear strain contours of Figs. 13d and 16d, which apply for the case of the long overhang.

The overhangs used in these tests were about 1/2 and 4 times the specimen thickness. The results suggest that an overhang equal to one specimen thickness would be sufficient to provide the same strain distributions as the long overhang, and an overhang of 1/2 the thickness achieves nearly the same condition.

These observations pertain to the load levels of the whole-field patterns cited. Whether strain distributions near the overhang change significantly at the highest load levels has not been investigated. Failure loads for the 3-point bending specimens with long overhangs were higher than those without long overhangs. This suggests a beneficial effect at high load levels, but too few tests were involved for generalization.

VII. NONLINEARITY

Figures 19a and b show the shear strains (at the center of the bay) per unit load vs. load on the specimen. Both variables are normalized by the failure load. A constant value of $\gamma_{zx}(P_f/P)$ would indicate a linear relationship between shear strain and load. The results show that the

unidirectional beams are strongly nonlinear, while the quasi-isotropic beams are weakly nonlinear.

For the unidirectional beams, results for the two cases of 3-point loading show essentially equal behaviors. They are significantly different, however, for the quasi-isotropic beams. The latter behavior is unexpected for the lower load levels, since evidence already mentioned indicates that the overhang has minimal influence on the strain distribution in the beam. The same disparity appears as seemingly large differences in deformations and strains exhibited in Figs. 16 and 17. A search for errors in the data reduction uncovered none. The results mean that the stiffness of the quasi-isotropic beam with overhang was exceptionally low, that of the beam without overhang was exceptionally stiff, or both. While properties of nominally equal composite specimens are known to vary, this explanation is not offered with strong confidence.

VIII. COMPARISON: 5-POINT AND 3-POINT LOADINGS

Five-point loading provides the advantage of a specimen having both high shear strains and minimal normal strains over a substantial region of the specimen. It offers an interesting possibility for experiments requiring measurements in shear fields. On the other hand, the applied load distribution and consequent stresses and strains are not known a priori and they are highly sensitive to the uniformity of thickness of the specimen and flatness of its surfaces.

Three-point bending is suitable for experiments in which the presence of normal strains does not hamper the development and observation of specimen performance associated with shear strains. Shear-induced failures might fall into this category. The load and stress distributions are much less sensitive

to variations of specimen thickness and flatness than the case of 5-point loading. The loading conditions are more easily reproduced. Comparison of normal strains ε_x and ε_z from Figs. 12i,j and 17i,j shows much larger ε_x near the center of the bay for 3-point flexure than 5-point flexure. At the same time, comparison of Figs. 12d and 17d shows shear strains of similar magnitudes. The 5-point load arrangement provides a large zone near the center of the specimen where shear strains are large and normal strains are small, which might make it a useful arrangement for studying transverse shear failure.

CONCLUSIONS

Detailed whole-field measurements of in-plane displacements and shear strains were obtained for composite beams under 5-point and 3-point flexure. Dramatic anomalous effects were observed. Analysis indicated their cause as resin-rich layers in regions of shear tractions; free-edge effects in quasi-isotropic specimens in regions of normal strains; and cyclic shear compliance of quasi-isotropic plies in regions of shear tractions. Substantially elevated shear strains γ_{zx} resulted from each of these causes. Their contributions could occur independently or in superposition. Shear strains attributed to resin-rich layers and cyclic shear compliance extend through the interior of the beam, but free edge effects produce anomalous shears on the edge of the beam which attenuate rapidly to zero in the interior.

The 5-point bending arrangement produces a central zone where shear strains are high while normal strains are low. The long overhang has minimal benefical effect for both 5-point and 3-point loadings, at least at lower load levels. The specimen material exhibits relaxation and the specimen exhibits nonlinear stiffness with load.

The highest shear stains do not occur near the center of the beam thickness, but closer to a point of load application. Modifications of the loading fixture to distribute the contact pressures are suggested. The intent is to restrict maximum shear strain to the center of the specimen, thereby reducing the uncertainty of its magnitude and forcing failure to occur in this region. It would also minimize the influence of free-edge shear strains, which increase with distance from the beam neutral axis.

Moire interferometry is well suited for detailed deformation analysis of composites. It provides subwavelength sensitivity, extensive range with load-induced fringe orders exceeding 1000, and excellent spatial resolution. A special method for determining whole-field contours of shear strains was developed and it proved to be effective and practical.

ACKNOWLEDGEMENT

The authors are grateful to Carl T. Herakovich of VPI & SU for his helpful discussions and important contributions. Professor Herakovich provided information on G_{zx} in connection with the section on Cyclic Shear Compliance and we especially acknowledge and appreciate this help.

REFERENCES

1. Williams, J. G., and Rhodes, M. D., The Effect of Resin on the Impact Damage Tolerance of Graphite/Epoxy Laminates, Composite Materials: Testing and Design (Sixth Conference), ASTM STP 787, I. M. Daniel, Ed., American Society for Testing and Materials, 1982, pp. 450-480.

2. Post, D., Moire Interferometry at VPI&SU, Experimental Mechanics, 23(2), June 1983, pp. 203-211.

3. Post, D., Czarnek, R., and Joh, D., Shear Strain Contours From Moire Interferometry, Proc. 5th International Congress on Experimental Mechanics, Montreal, Canada, June 10-15, 1984.

4. Czarnek, R., Post, D., and Herakovich, C., Edge Effects in Composites by Moire Interferometry, Experimental Techniques, 7(1), Jan. 1983, pp. 18-21.

5. Herakovich, C. T., Post, D., Buczek, M., and Czarnek, R., Free-Edge Strain Concentrations in Real Composite Laminates, CCMS-84-10 (also VPI-84-24), VPI & SU, Blacksburg, VA 24061, July 1984.

6. Kriz, R. D. and Stinchcomb, W. W., Elastic Moduli of Transversely Isotropic Graphite Fibers and Their Composites, Experimental Mechanics, 19(2), Feb. 1979, pp. 41-49.

Table I

SPECIMENS

NASA specimen no.	Laminate* stacking sequence	Dimensions length x width x thickness	Original thickness, inches min. / max	Loading conditions — P_f, Failure load pounds (kN)
W 36-5	$[0]_{48}$ unidirectional	4 x 1 x 0.258 in. 102 x 25 x 6.55 mm	0.269 / 0.276	5-point 11,360 (50.5)
W 36-21		3 x 1 x 0.280 in. 76 x 25 x 7.11 mm	0.282 / 0.289	3-point w/overhang 5,940 (26.4)
W 36-47		1 1/4 x 1 x 0.242 in. 32 x 25 x 6.35 mm	0.281 / 0.285	3-point 5,480 (24.4)
W 54-3-4	$[45/0/-45/90]_{6s}$ quasi-isotropic	4 x 1 x 0.242 in. 102 x 25 x 6.15 mm	0.251 / 0.254	5-point 5,480 (24.4)
W 54-3-12		3 x 1 x 0.241 in. 76 x 25 x 6.12 mm	0.250 / 0.256	3-pt. w/overhang 3,840 (17.1)
W 54-3-9		1 1/4 x 1 x 0.245 in. 32 x 25 x 6.22 mm	0.250 / 0.258	3-point 3,770 (16.8)

* Material: graphite-epoxy T300-5208

Table II

PRIMARY RESULTS - LIST OF FIGURES

				Load Level P/P_f, Percent of Failure Load									
Figure Letter:				a	b	c	d	e	f	g	h	i	j
Fig. No.	Matl.	Load	Over-hang	U	W	U*	γ_{zx} Contour	γ_{zx} Graphs	$\frac{\Delta U}{\Delta z}$	$\frac{\Delta W}{\Delta x}$	$\frac{\Delta U}{\Delta z}$, $\frac{\Delta W}{\Delta x}$	ε_x	ε_z
12	0°	5-pt.	Yes	50	50	50	50	50,84	50	50	50	50	50
13	0°	3-pt.	Yes	38	38	19	38	38,86					
14	0°	3-pt.	No	42	42	42	42	42,80					
15	Quasi	5-pt.	Yes	50	50	29	50	50,99				50	50
16	Quasi	3-pt.	Yes	38	38	19	38	38,85					
17	Quasi	3-pt.	No	36	36	18	36	36,82	36	36	36	36	36

* Multiple bays; all other figures show one bay adjacent to central load.

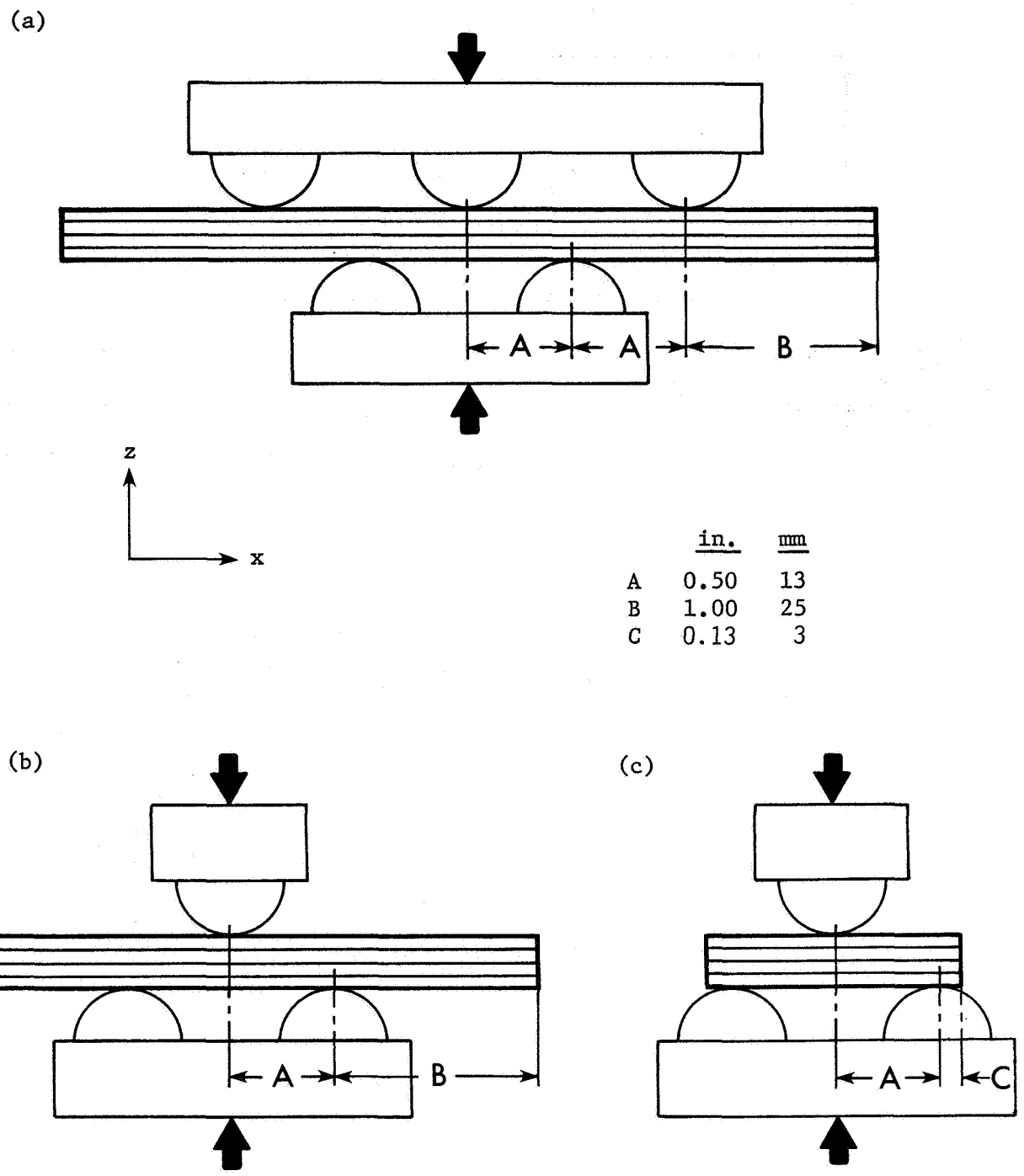

	in.	mm
A	0.50	13
B	1.00	25
C	0.13	3

Fig. 1 Schematic diagram of loading conditions.
(a) 5-point loading
(b) 3-point loading with specimen overhang
(c) 3-point loading

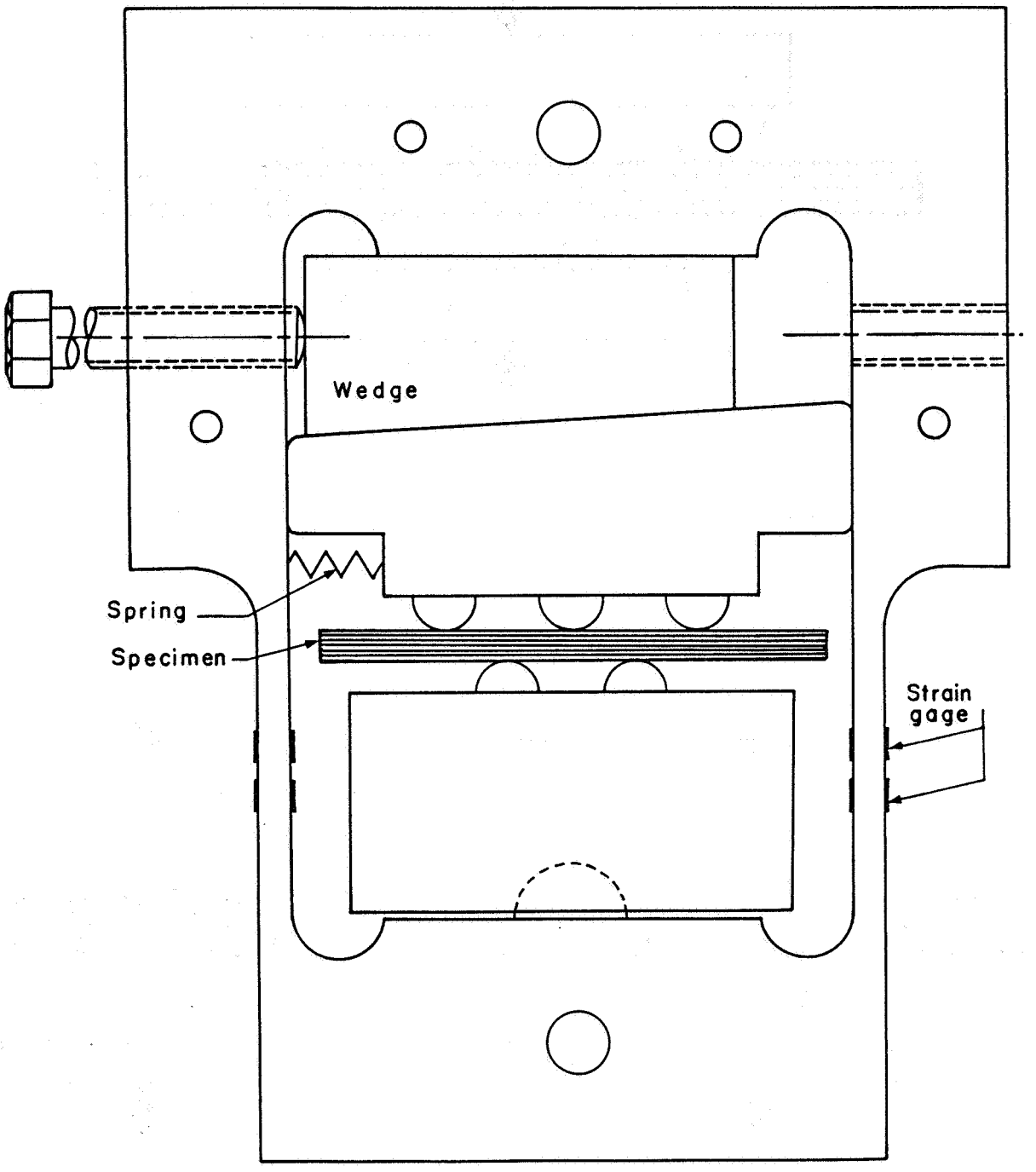

Fig. 2 Loading fixture.

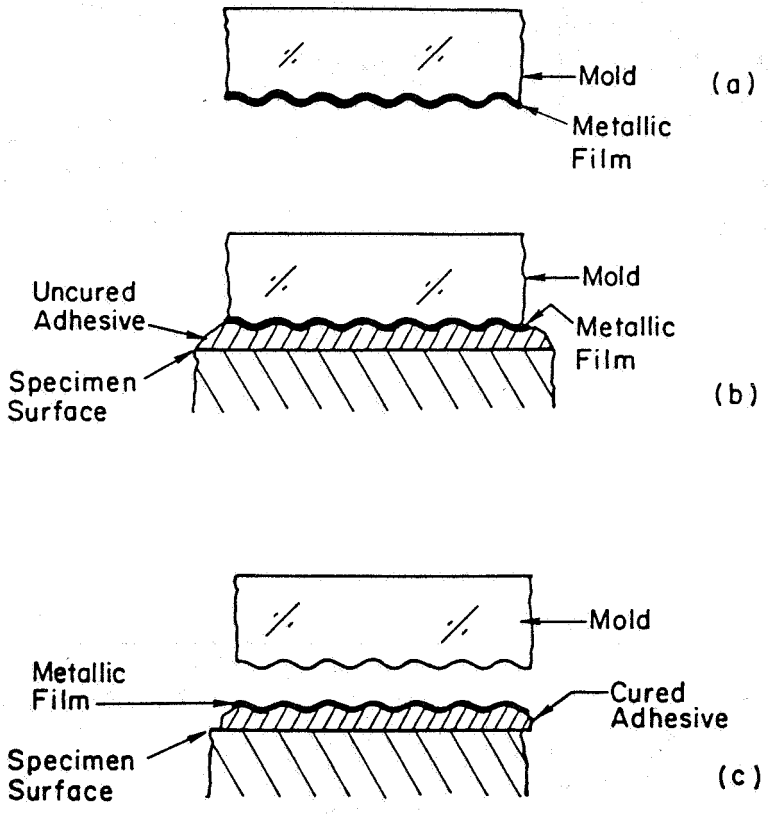

Fig. 3 Technique to form a high-frequency, high reflectance grating on the specimen.

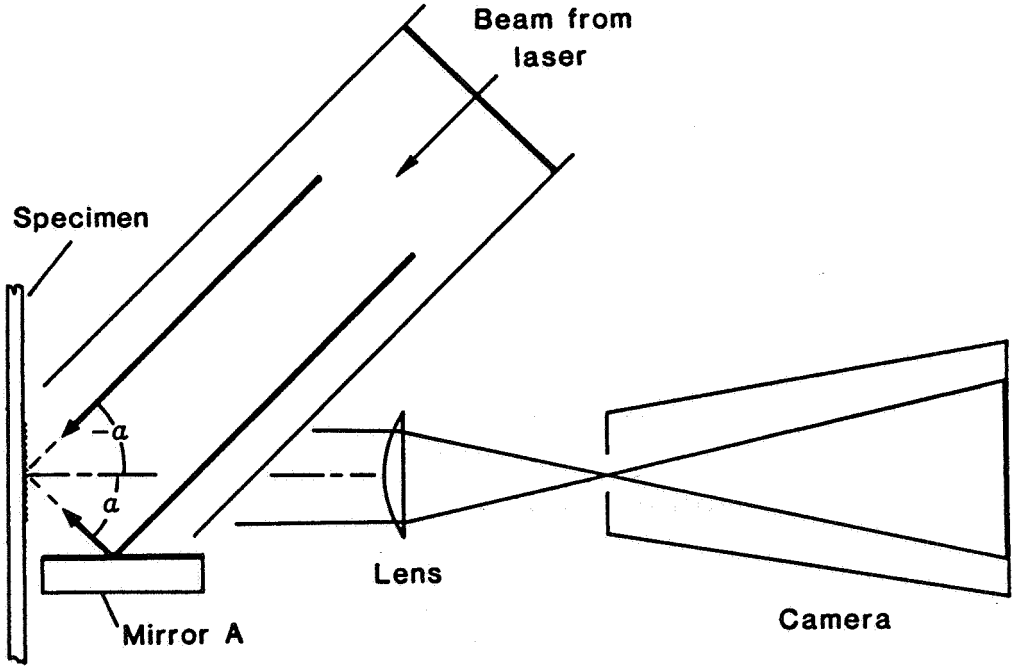

Fig. 4 Optical arrangement for U displacement field.

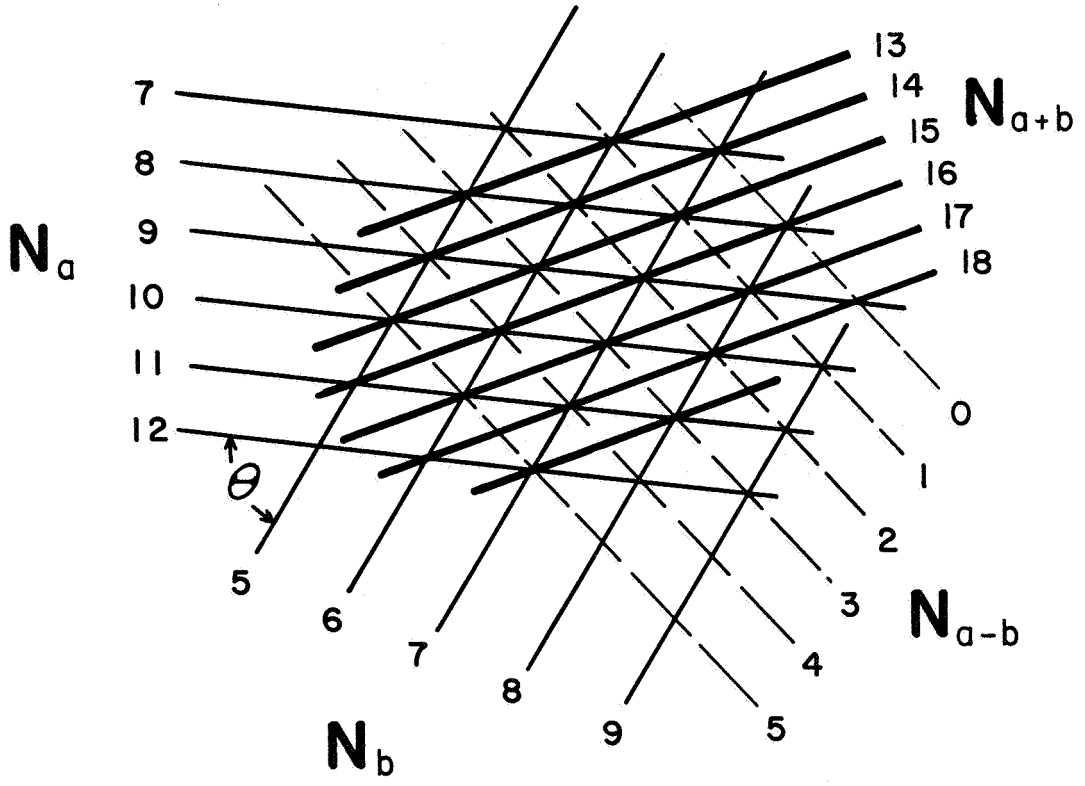

Fig. 5 Diagonals through two families of parametric curves yield new families of their sum and difference.

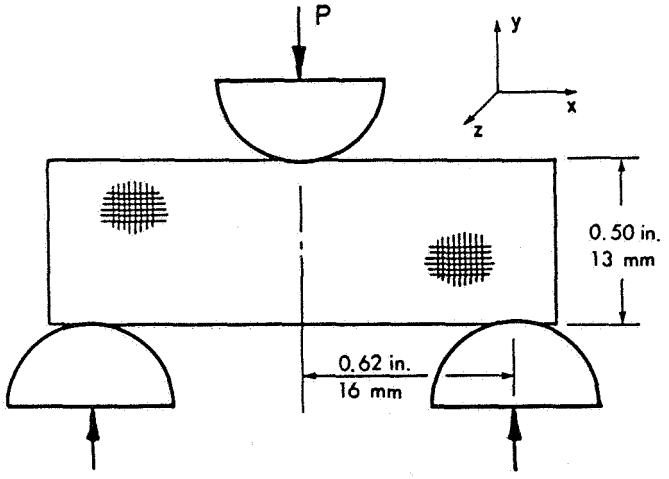

Fig. 6 Specimen geometry and loading. Material: epoxy. Width (perpendicular to page): 1 in. (25.4 mm).

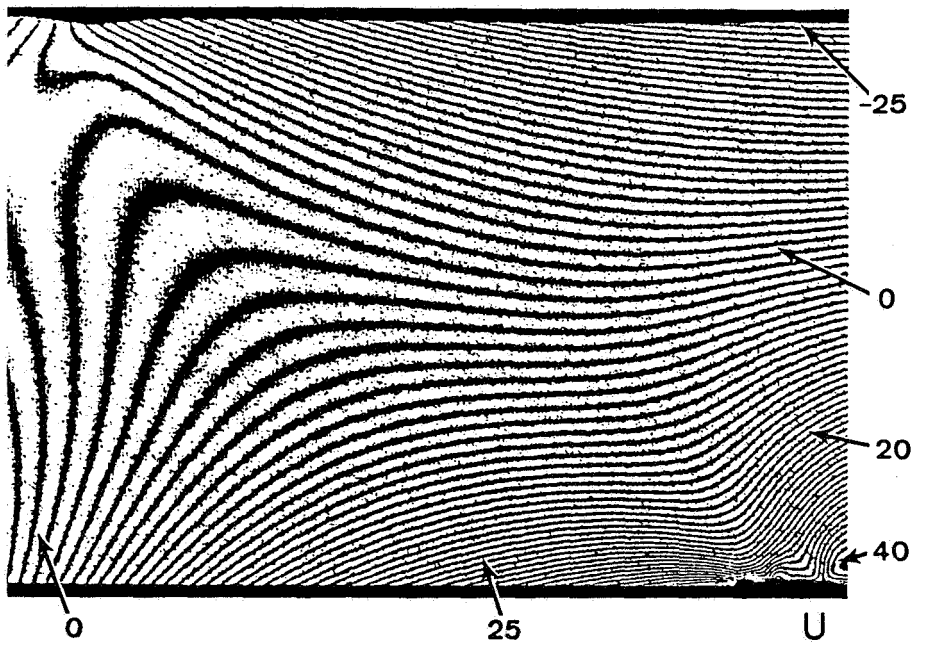

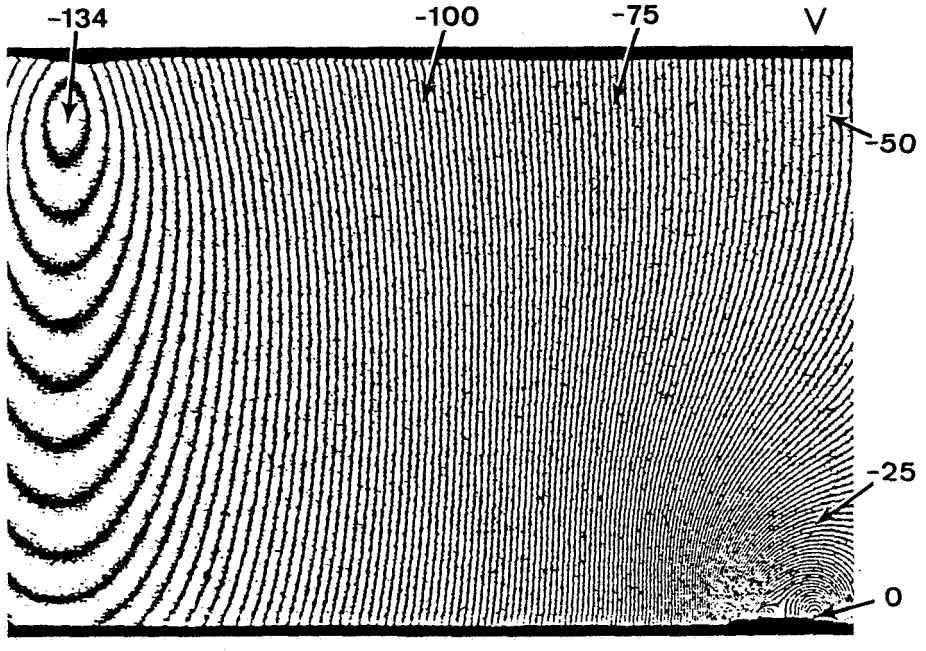

Fig. 7 Fringe patterns of N_x and N_y, depicting displacement fields U and V, respectively, for right side of beam. P = 69 lb. (0.307 kN).

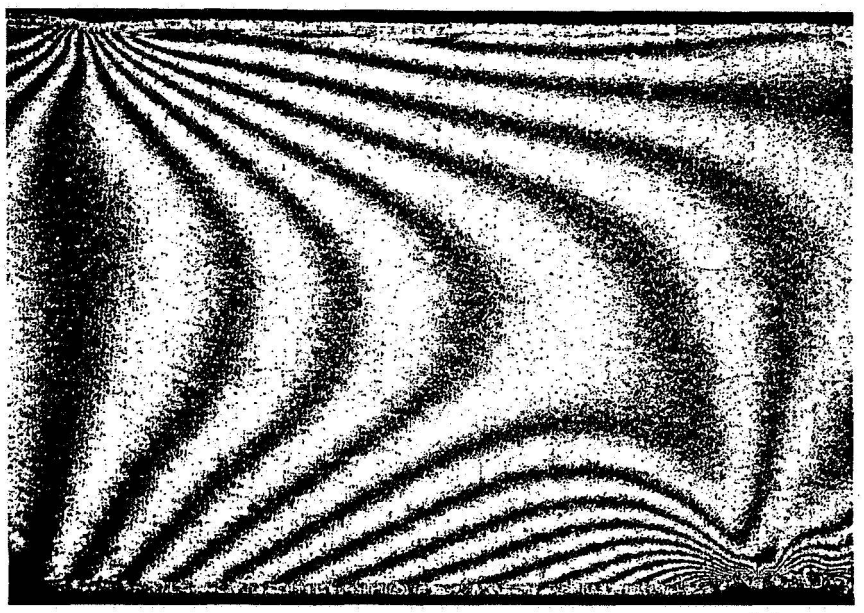

ΔN_x

ΔN_y

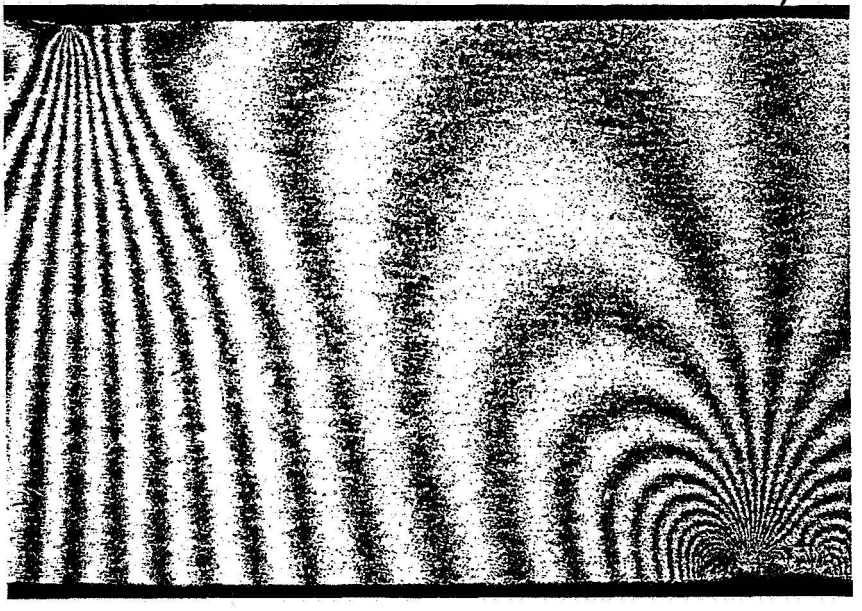

Fig. 8 Pattern of ΔN_x and ΔN_y from mechanical differentiation and optical filtering. They depict the cross-derivatives $\partial U/\partial y$ and $\partial V/\partial x$, respectively. P = 468 lb. (2.08 kN); $\Delta x = \Delta y$ = 0.010 in. (0.25 mm).

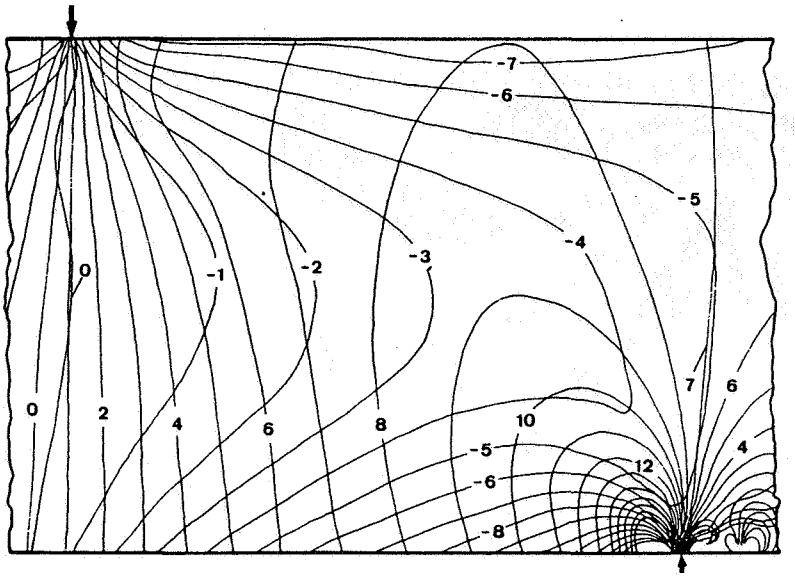

Fig. 9 Tracings of fringe centerlines from patterns of Fig. 8.

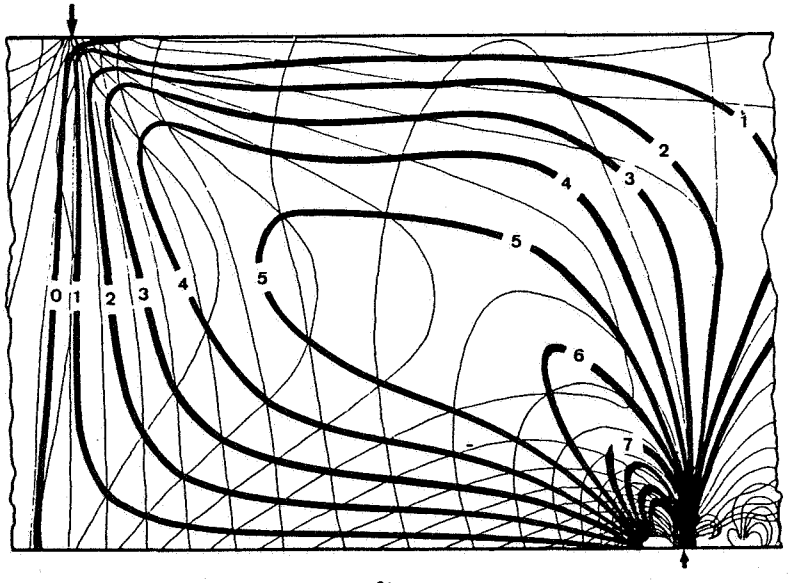

γ_{xy}

Fig. 10 Contours of ΔN_{x+y}, depicting the shear strain field γ_{xy}.

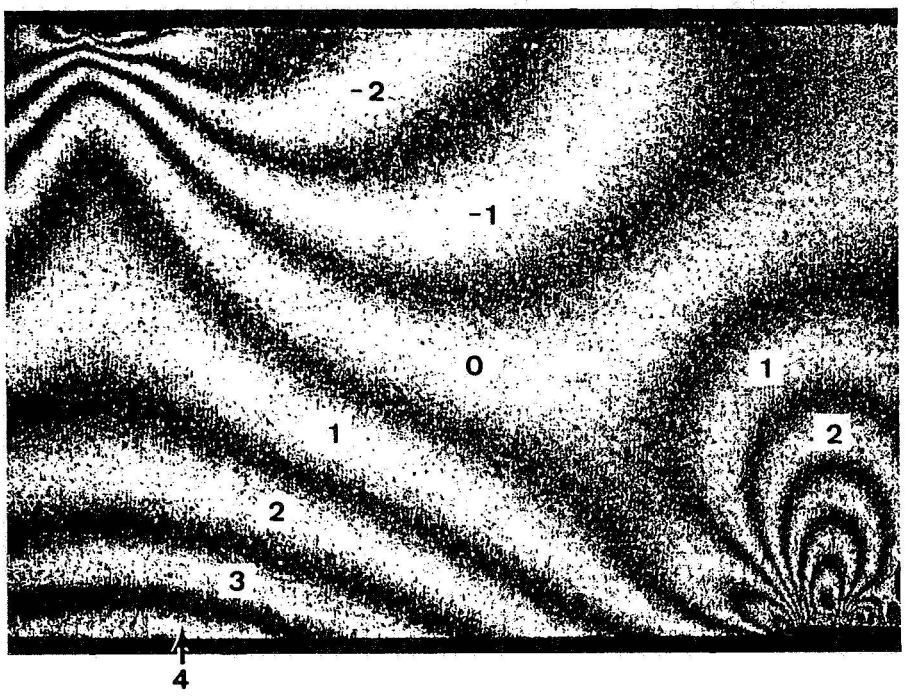

ϵ_x

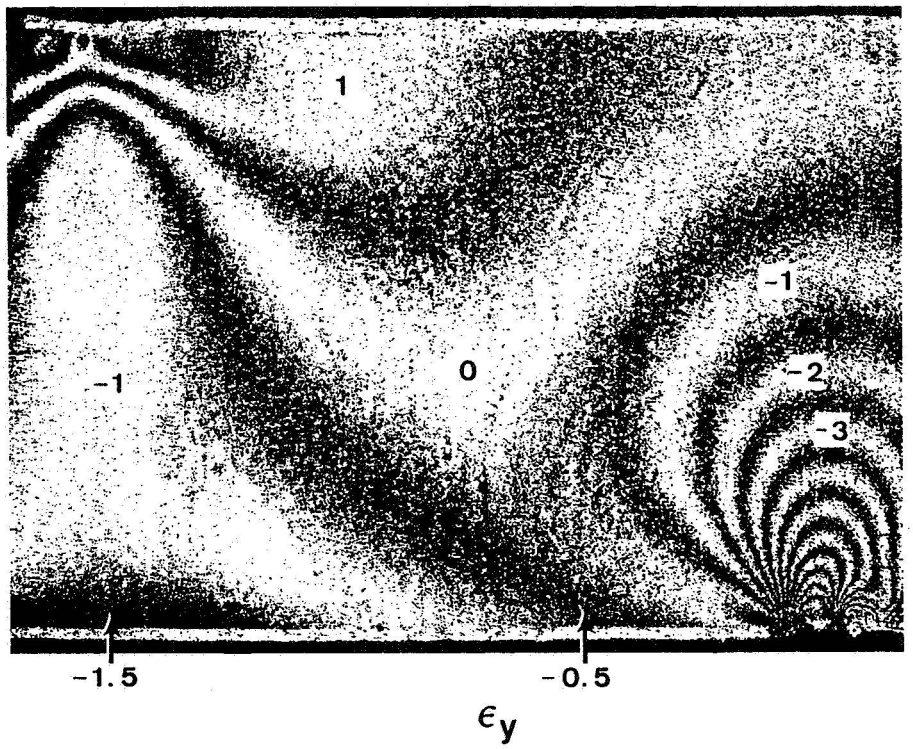

ϵ_y

Fig. 11 Patterns depicting normal strain fields ε_x and ε_y.

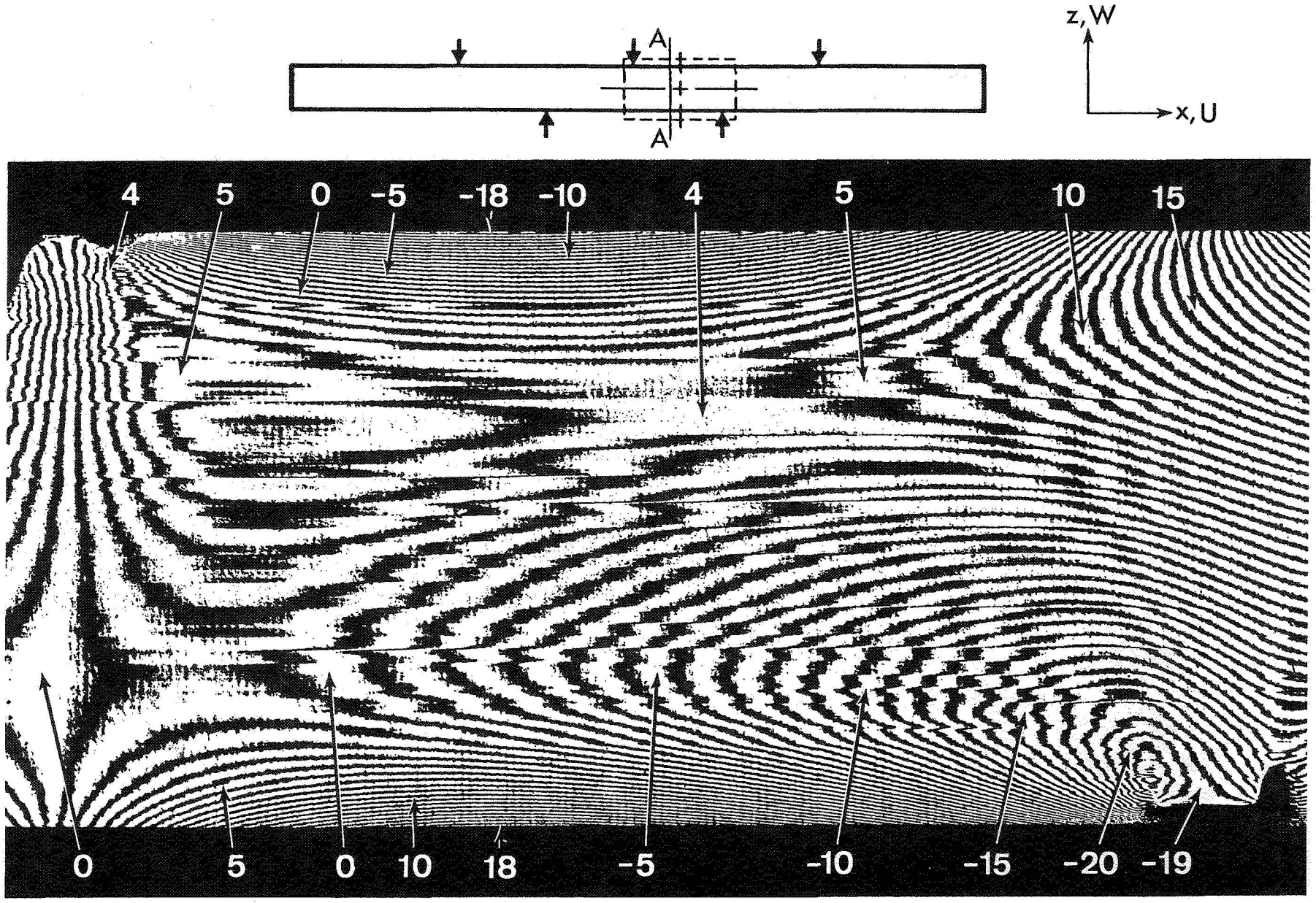

Fig. 12a U-displacement field; unidirectional composite; 5-point beam; P/P_f = 50%. The numbers are fringe orders N_x which specify U-displacements when multiplied by 16.4 μin. (0.417 μm).

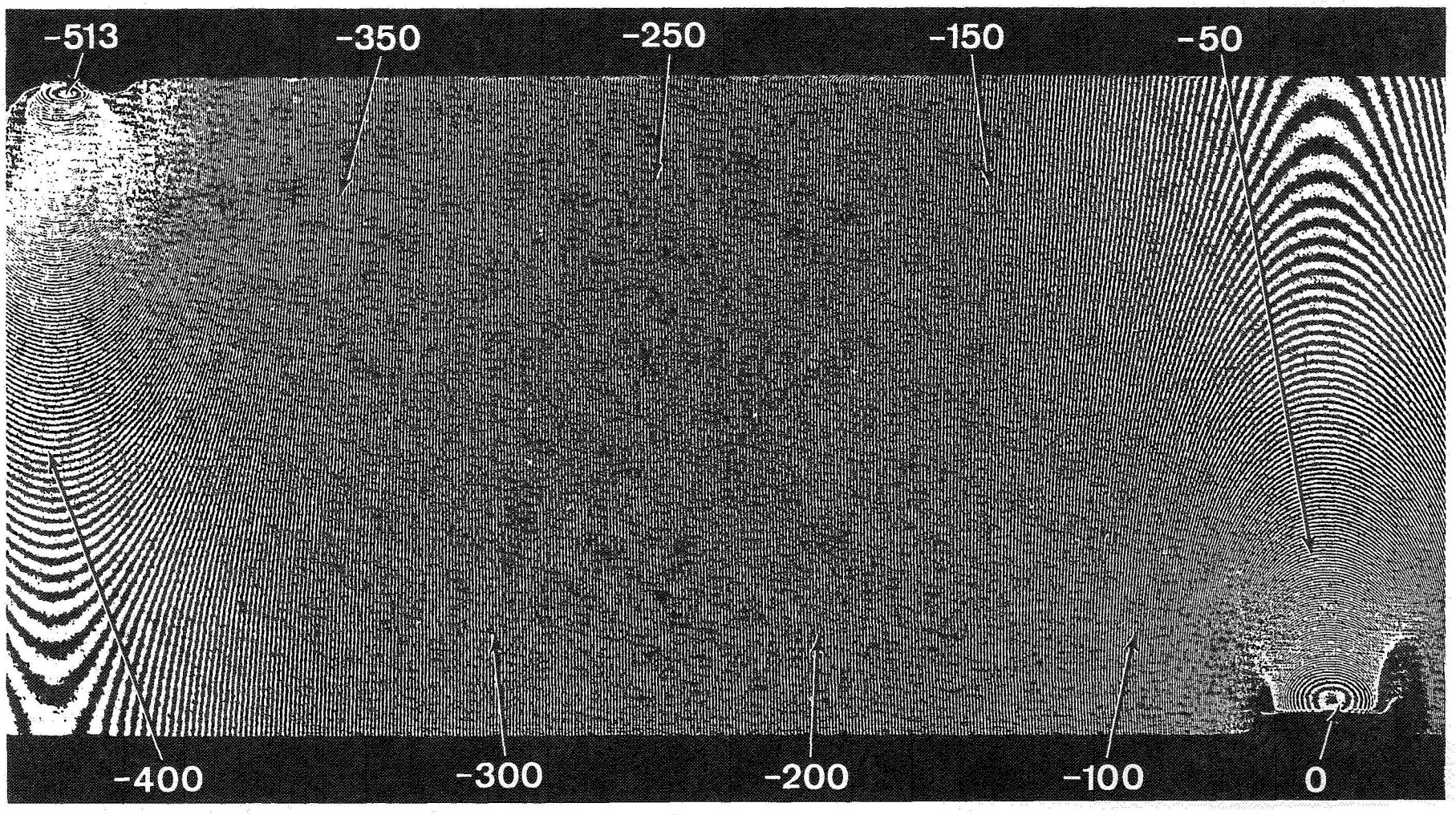

Fig. 12b W-displacement field; P/P_f = 50%. The numbers are fringe orders N_z which specify W-displacements when multiplied by 16.4 μin. (0.417 μm).

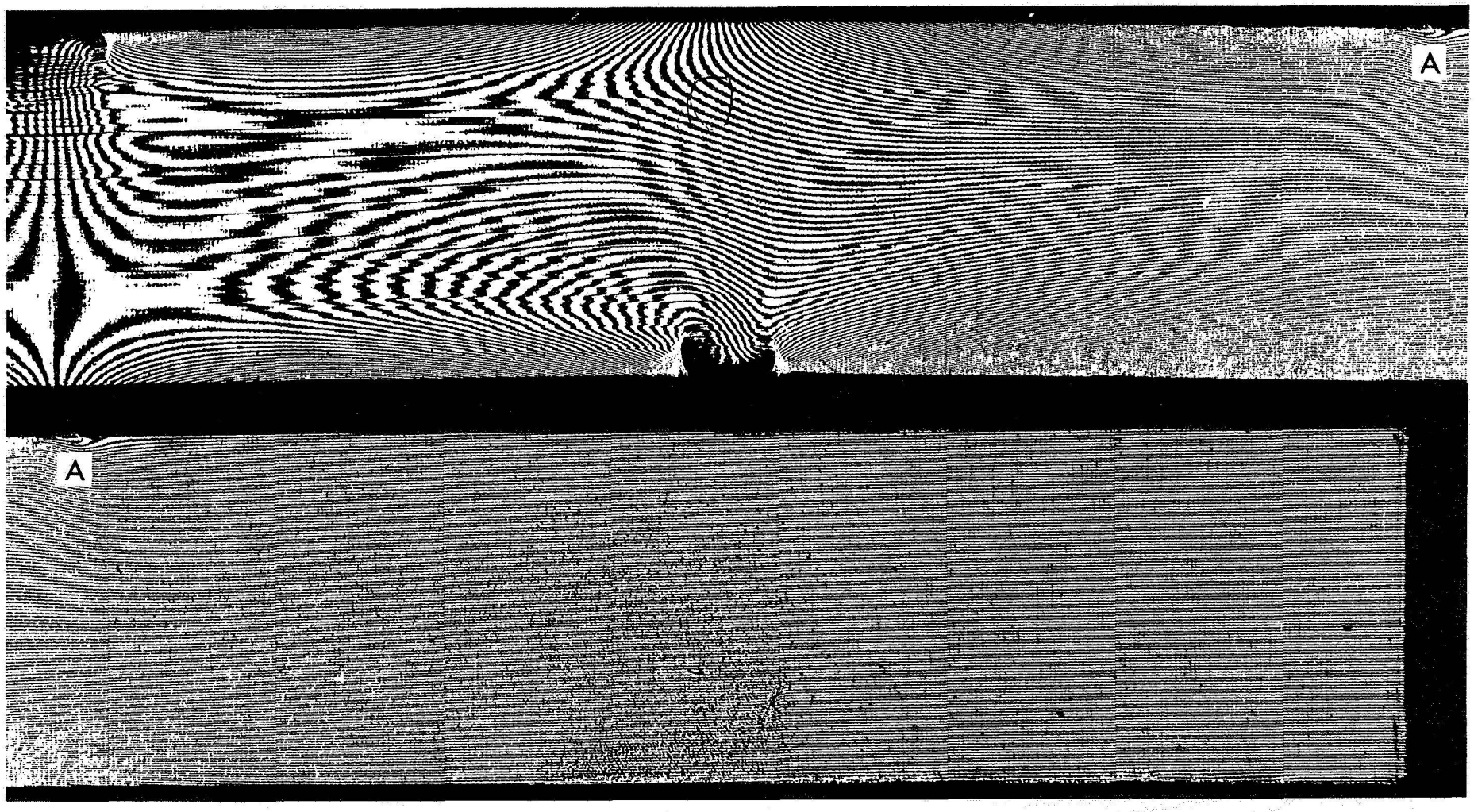

Fig. 12c U-displacement field, multiple bays; P/P_f = 50%.

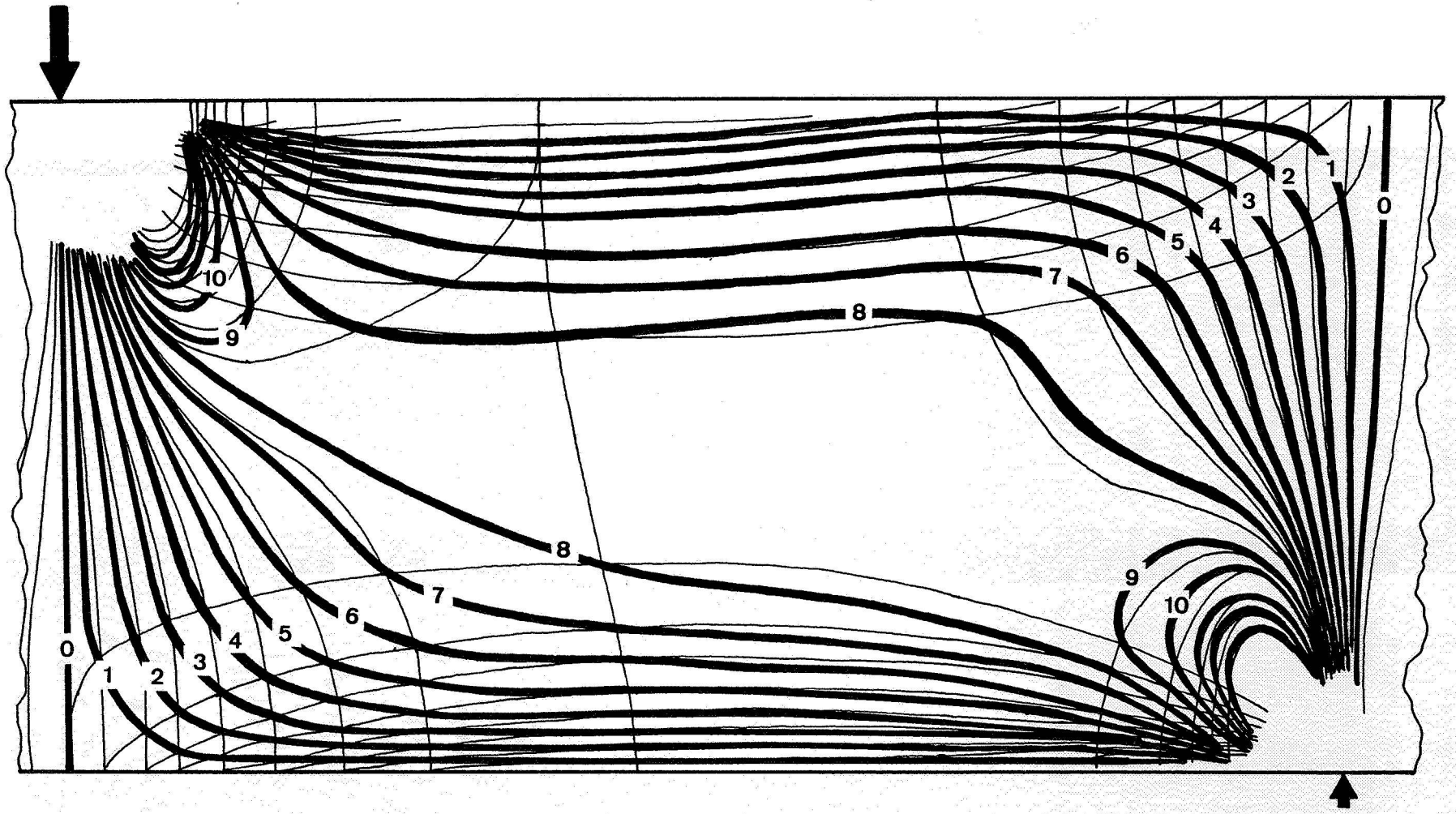

Fig. 12d Contour map of shear strains γ_{zx} (smoothed); $\Delta x,z$ = 0.010 in., P/P_f = 50%. The numbers are contour levels which signify shear strains when multiplied by 0.00167 m/m.

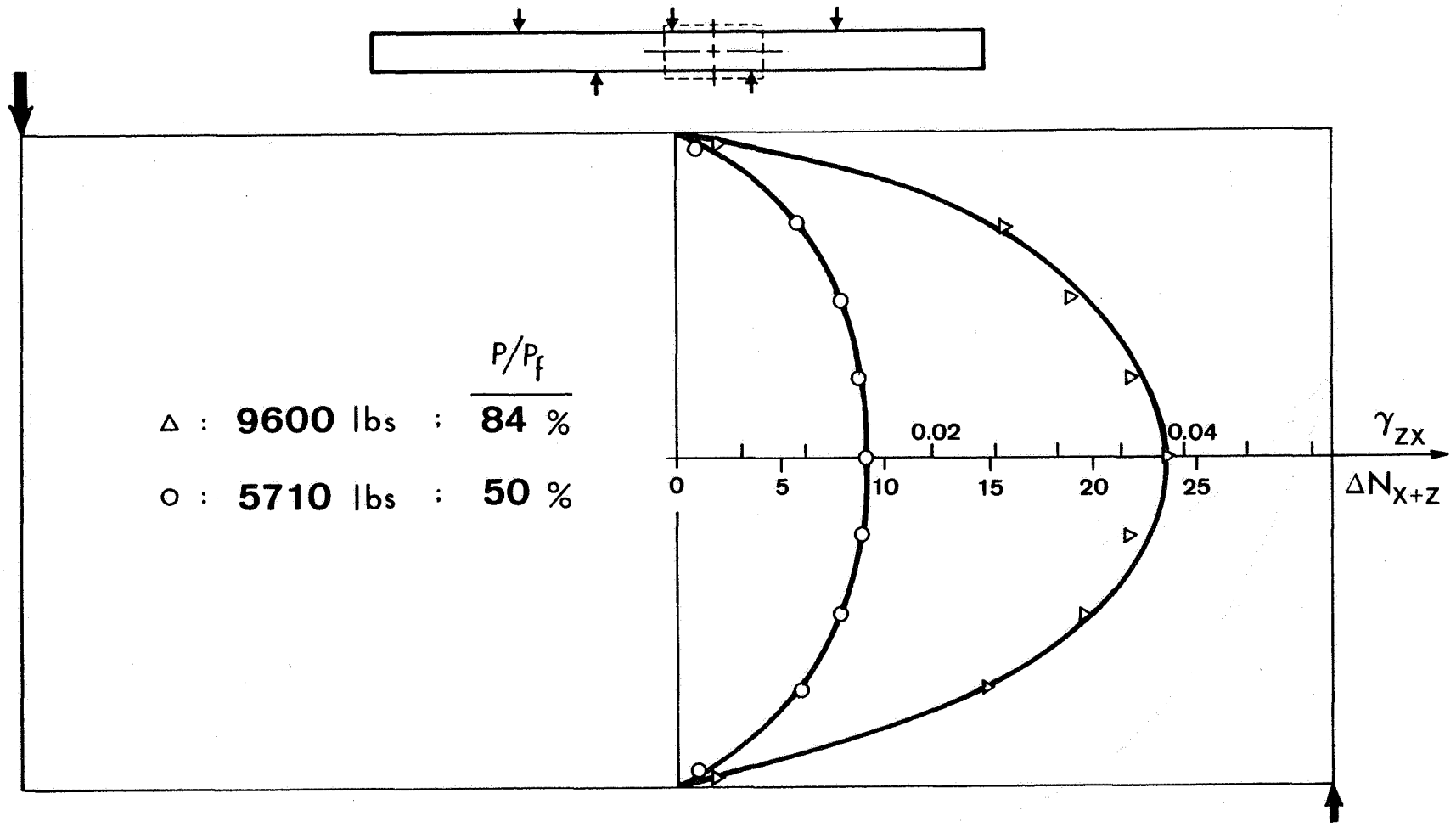

Fig. 12e$_1$ Shear strains (smoothed) along vertical centerline of bay denoted by dashed box.

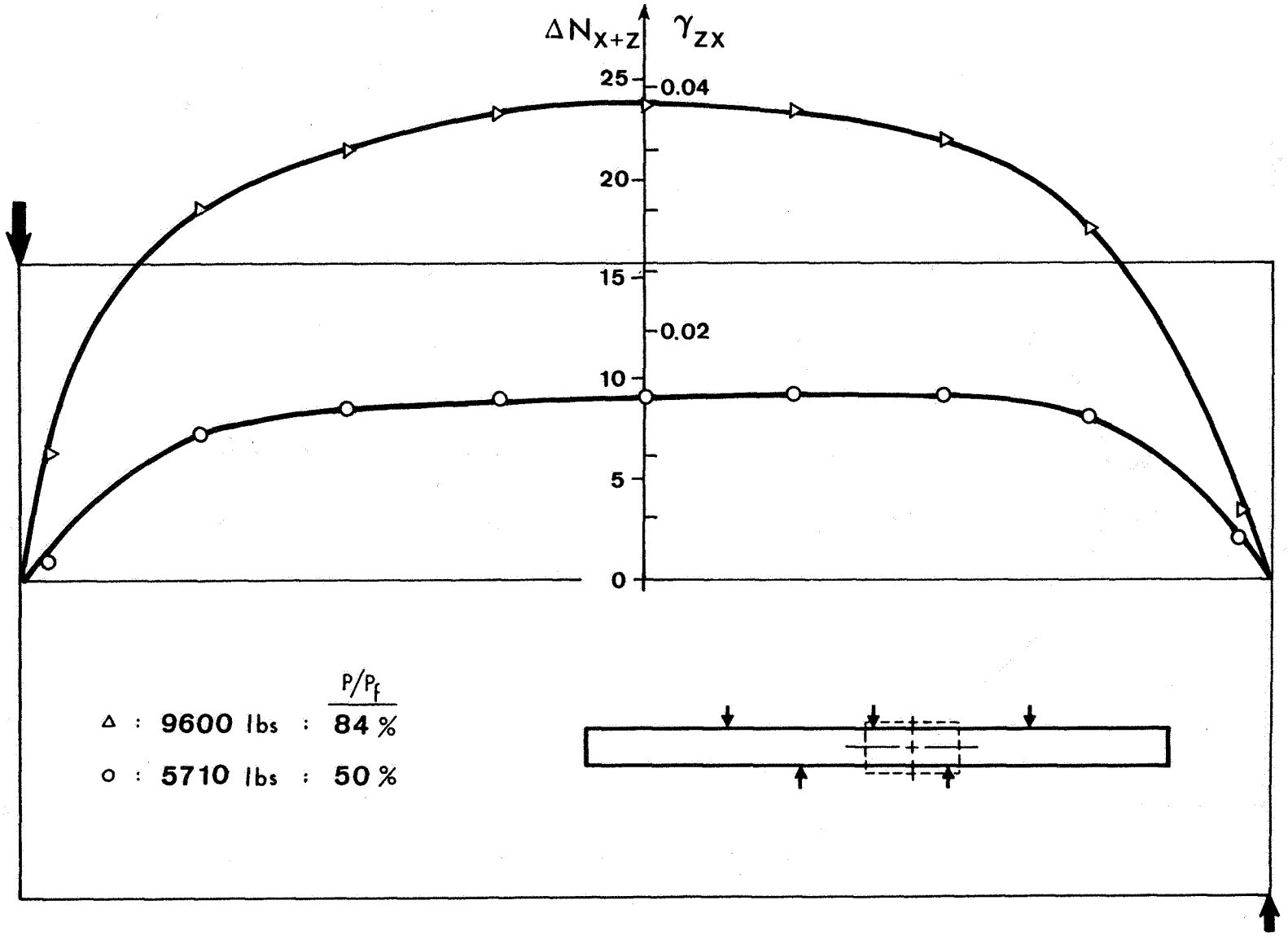

Fig. 12e_2 Shear strains (smoothed) along horizontal centerline of bay denoted by dashed box.

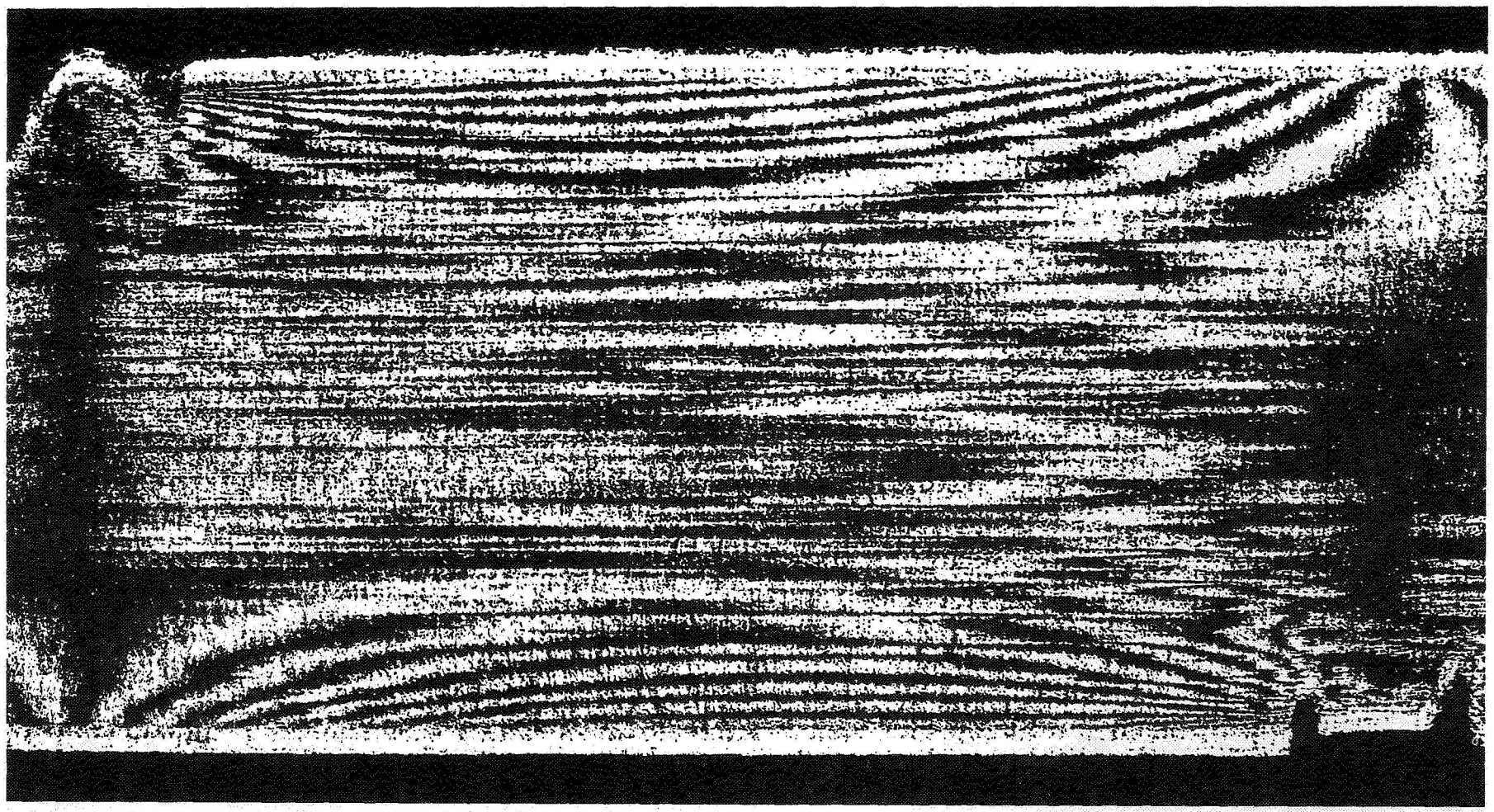

Fig. 12f Pattern of $\Delta U/\Delta z$ by mechanical differentiation; Δz = 0.010 in.; P/P_f = 50%.

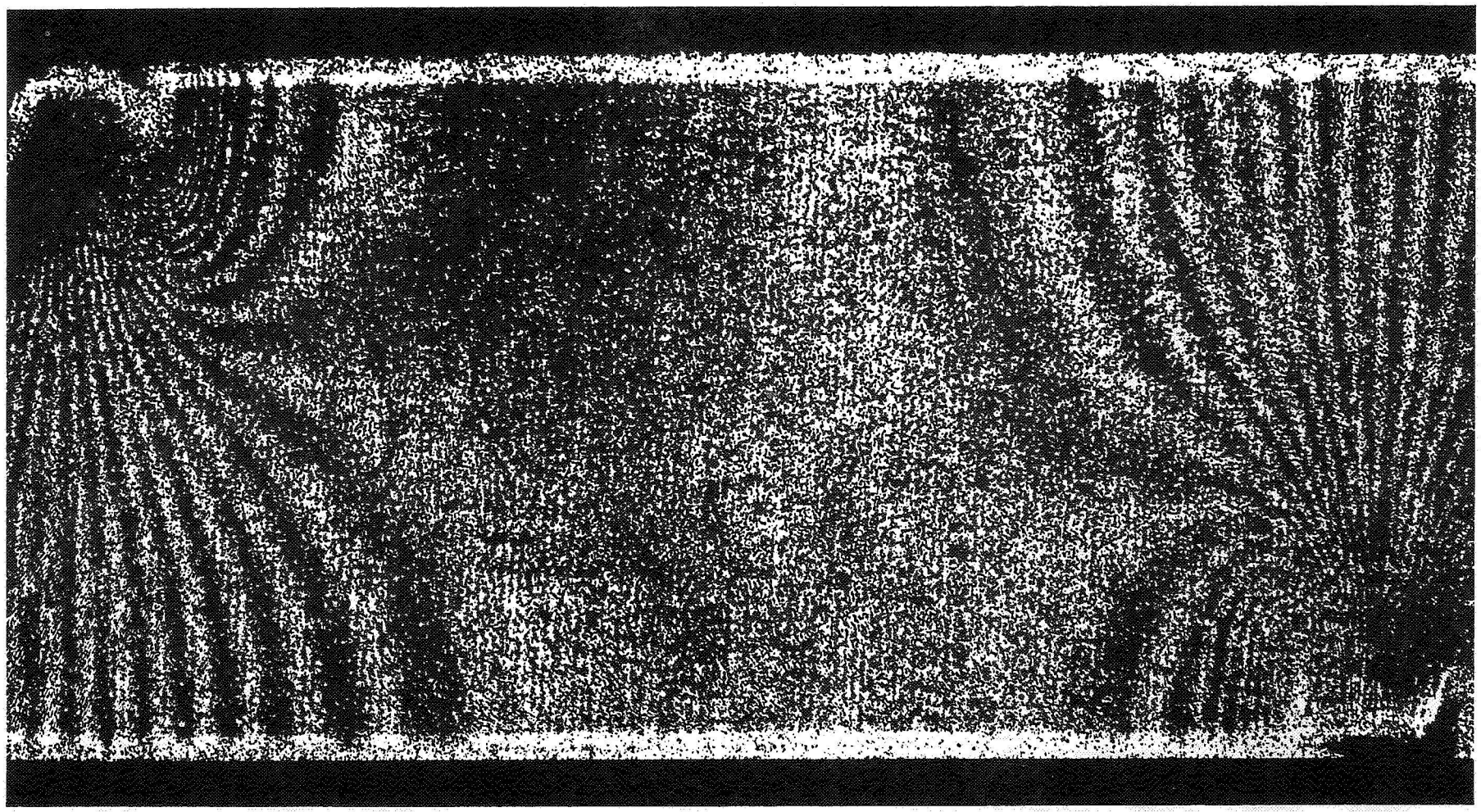

Fig. 12g Pattern of $\Delta W/\Delta x$ by mechanical differentiation; Δx = 0.010 in.; P/P_f = 50%.

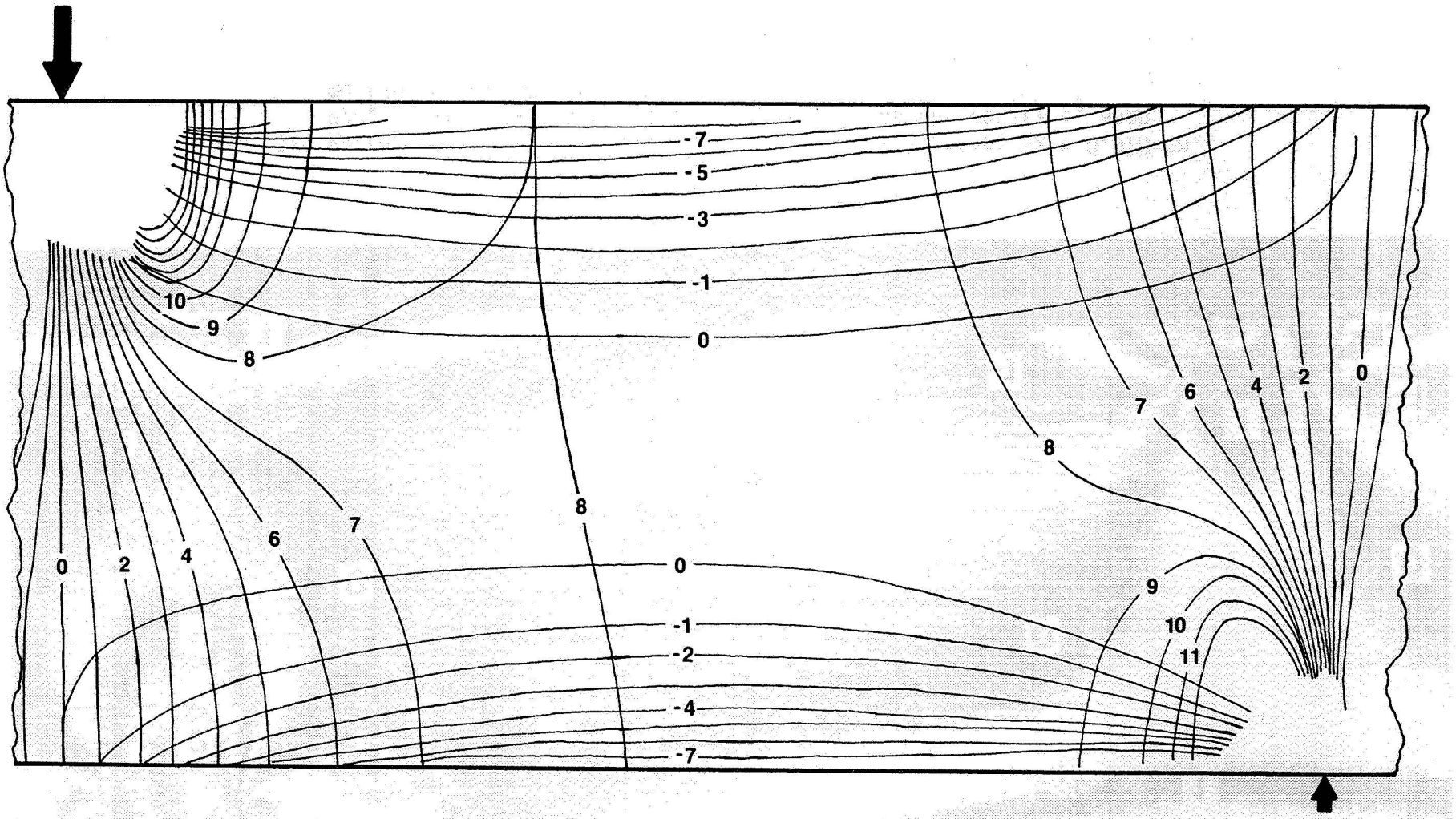

Fig. 12h Tracings of $\Delta U/\Delta z$ and $\Delta W/\Delta x$ contours; P/P_f = 50%. The numbers are contour levels which specify displacement gradients when multiplied by 0.00167 m/m.

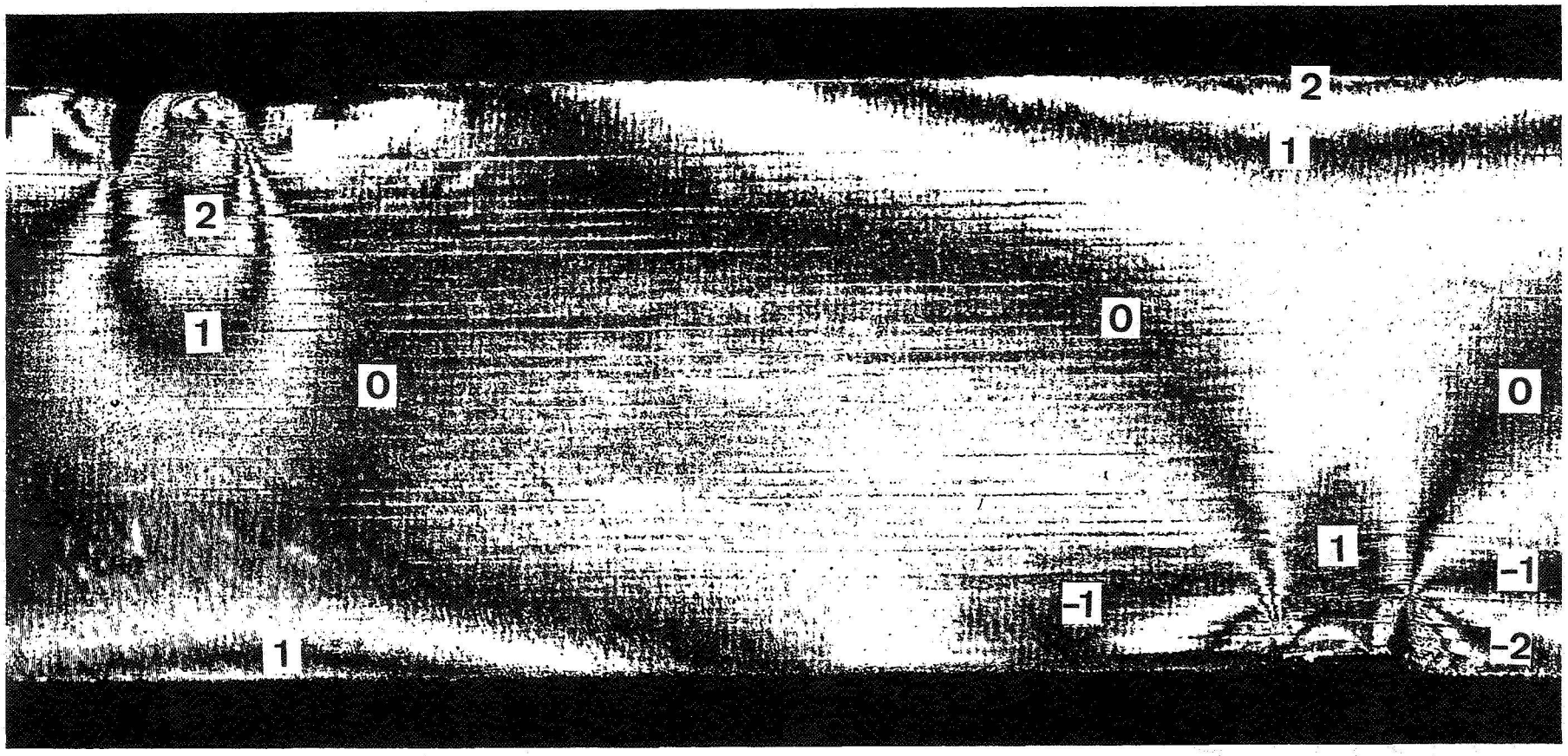

Fig. 12i Pattern of ε_x or $\Delta U/\Delta x$ by mechanical differentiation; Δx = 0.010 in.; P/P_f = 50%. The numbers are fringe orders which specify ε_z when multiplied by 0.00167 m/m.

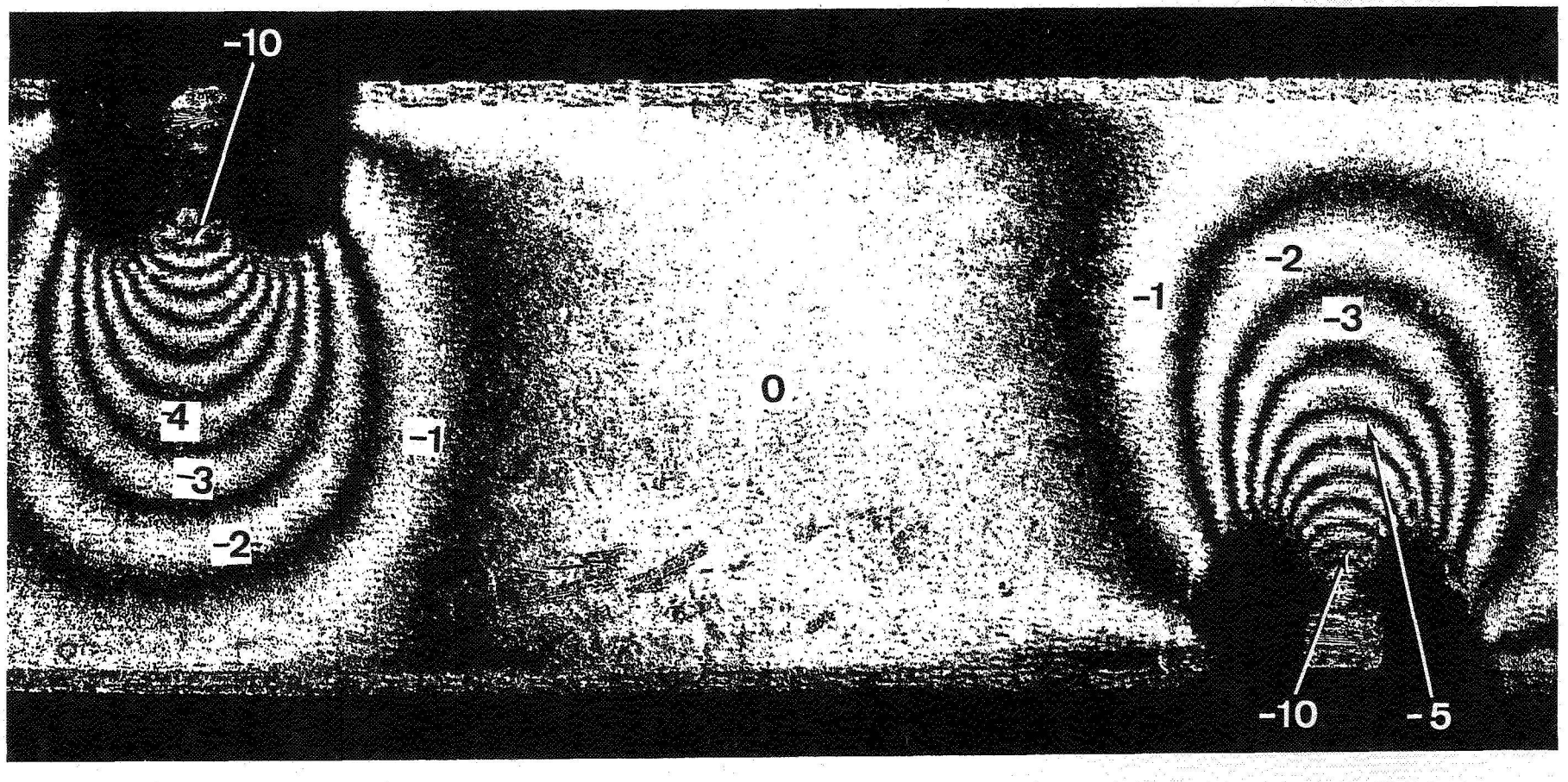

Fig. 12j Pattern of ε_z or $\Delta W/\Delta z$ by mechanical differentation; Δz = 0.010 in.; P/P_f = 50%. The numbers are fringe orders which specify ε_z when multiplied by 0.00167 m/m.

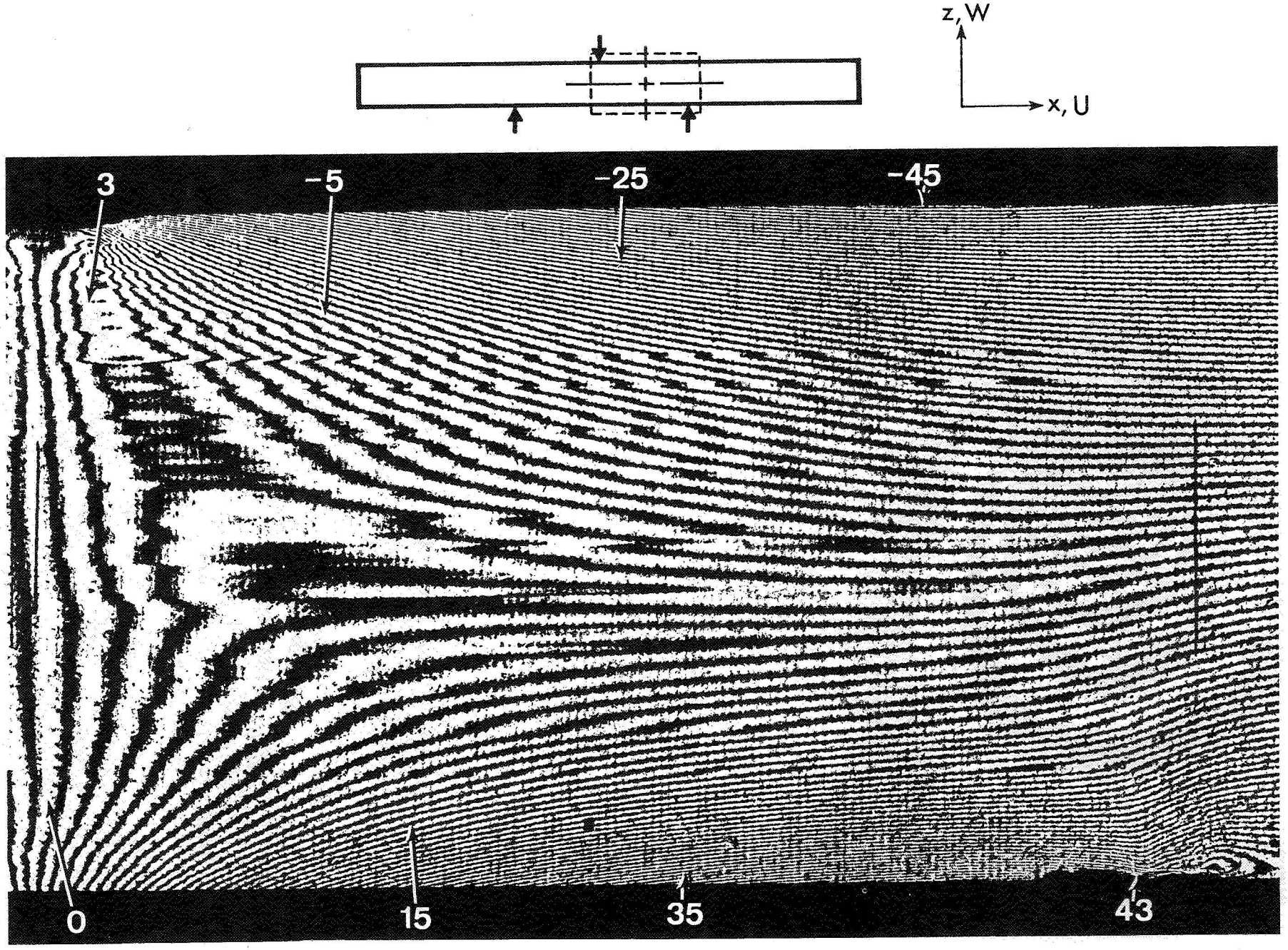

Fig. 13a U-displacement field; unidirectional composite; 3-point beam with overhang; P/P_f = 38%. The numbers are fringe orders N_x which specify U-displacements when multiplied by 16.4 μin. (0.417 μm).

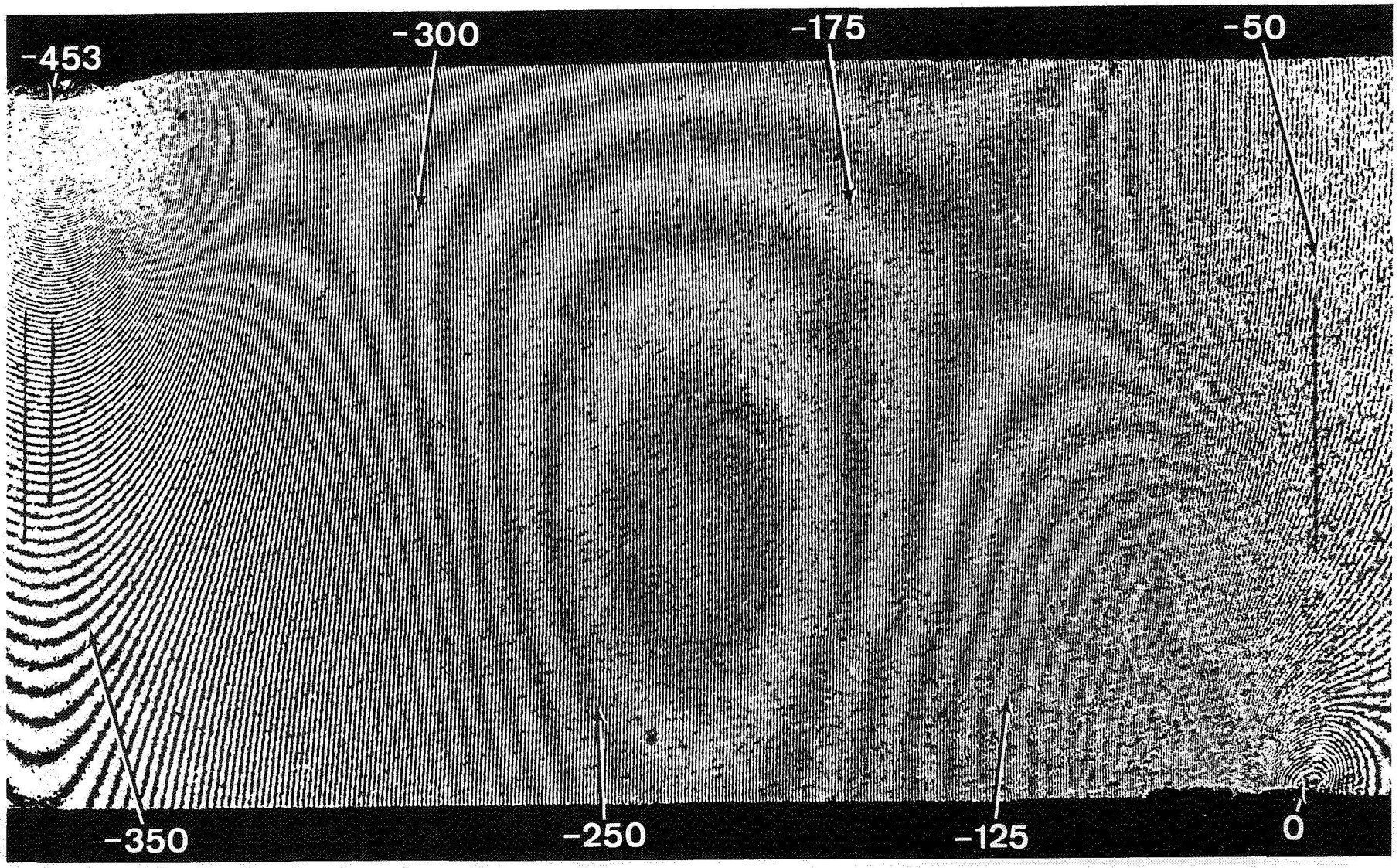

Fig. 13b W-displacement field; P/P_f = 38%. The numbers are fringe orders N_z which specify W-displacements when multiplied by 16.4 μin. (0.417 μm).

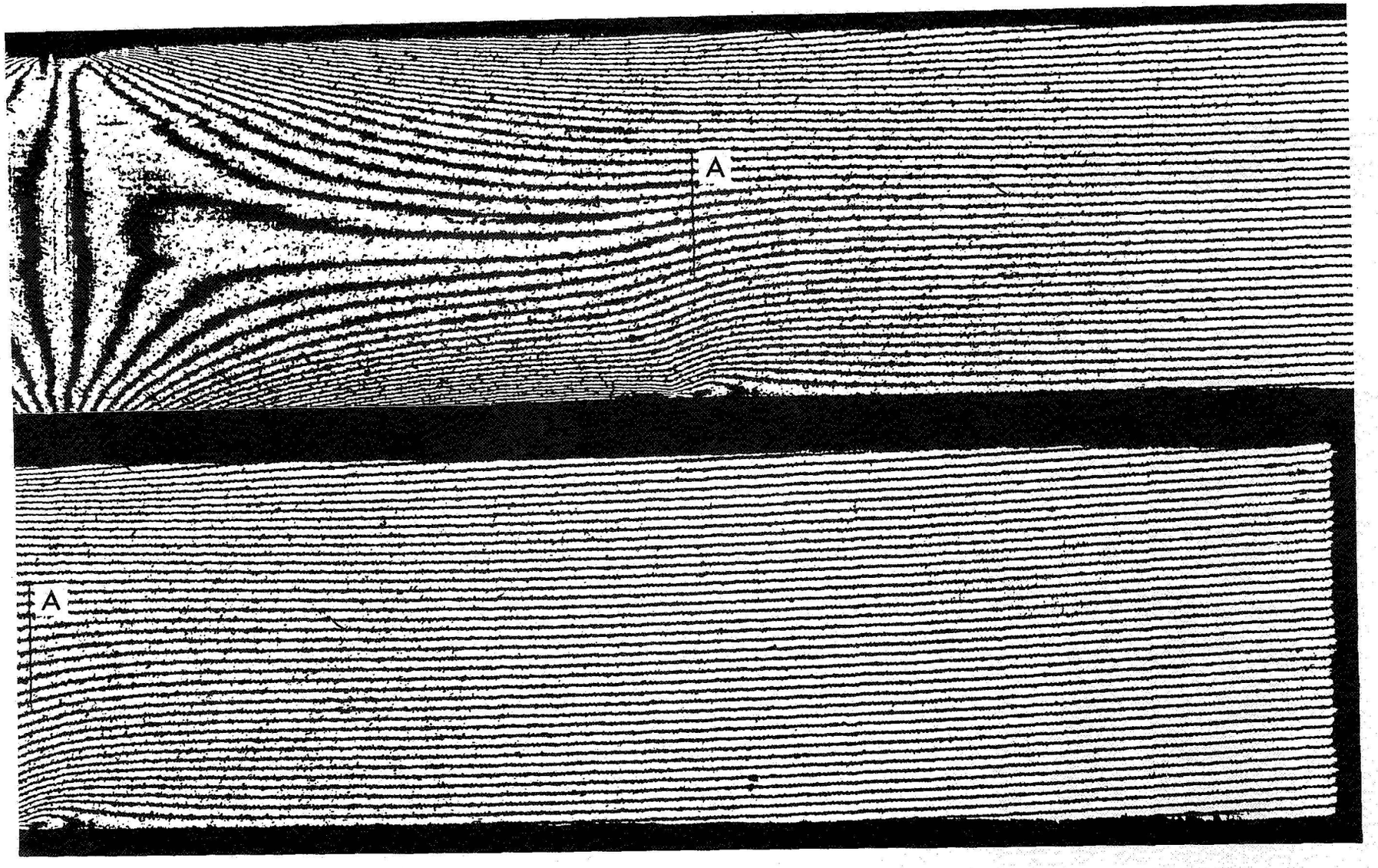

Fig. 13c U-displacement field, multiple bays; P/P_f = 19%.

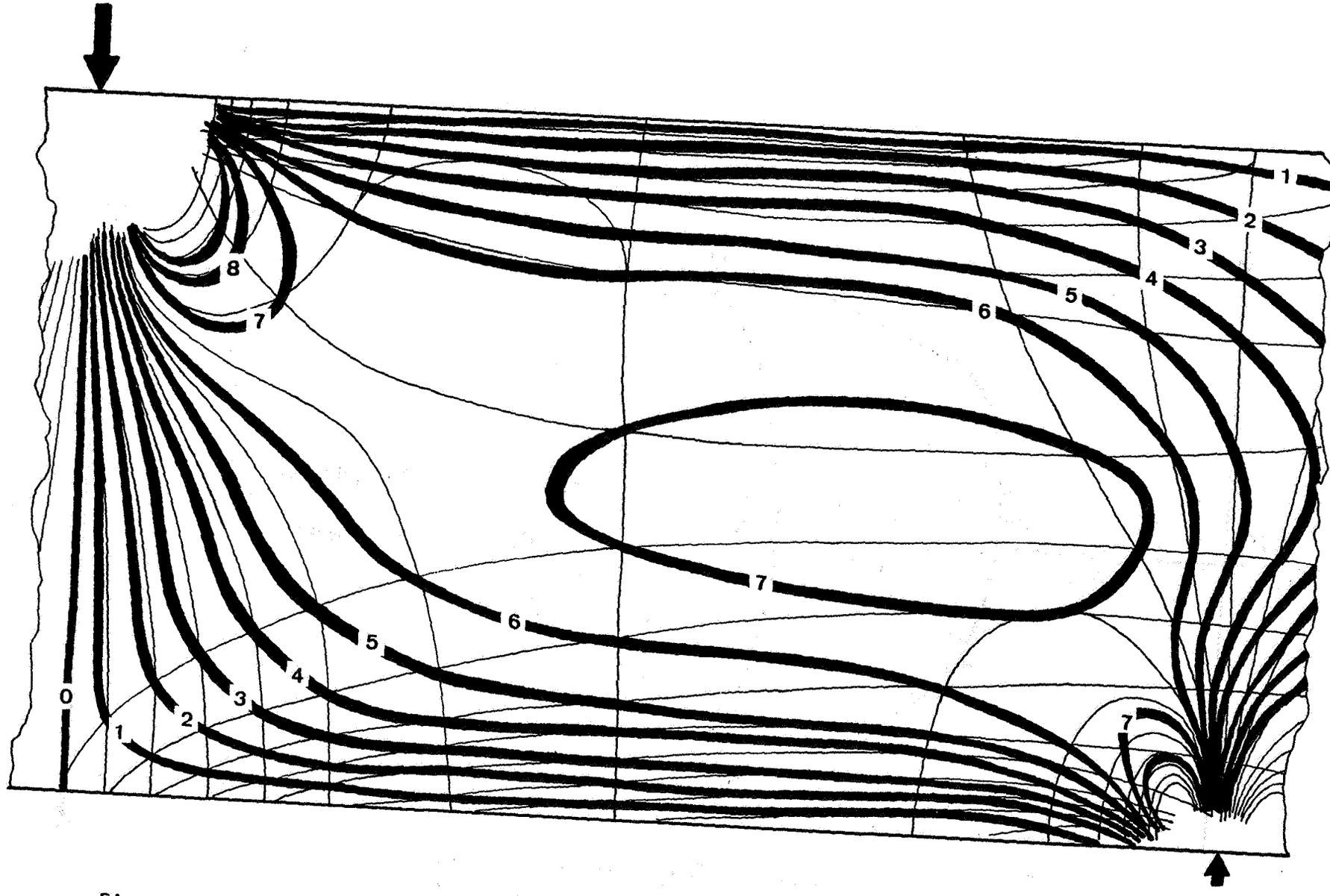

Fig. 13d Contour map of shear strains γ_{zx} (smoothed); $\Delta x,z = 0.010$ in.; $P/P_f = 38\%$. The numbers are contour levels which signify shear strains when multiplied by 0.00167 m/m.

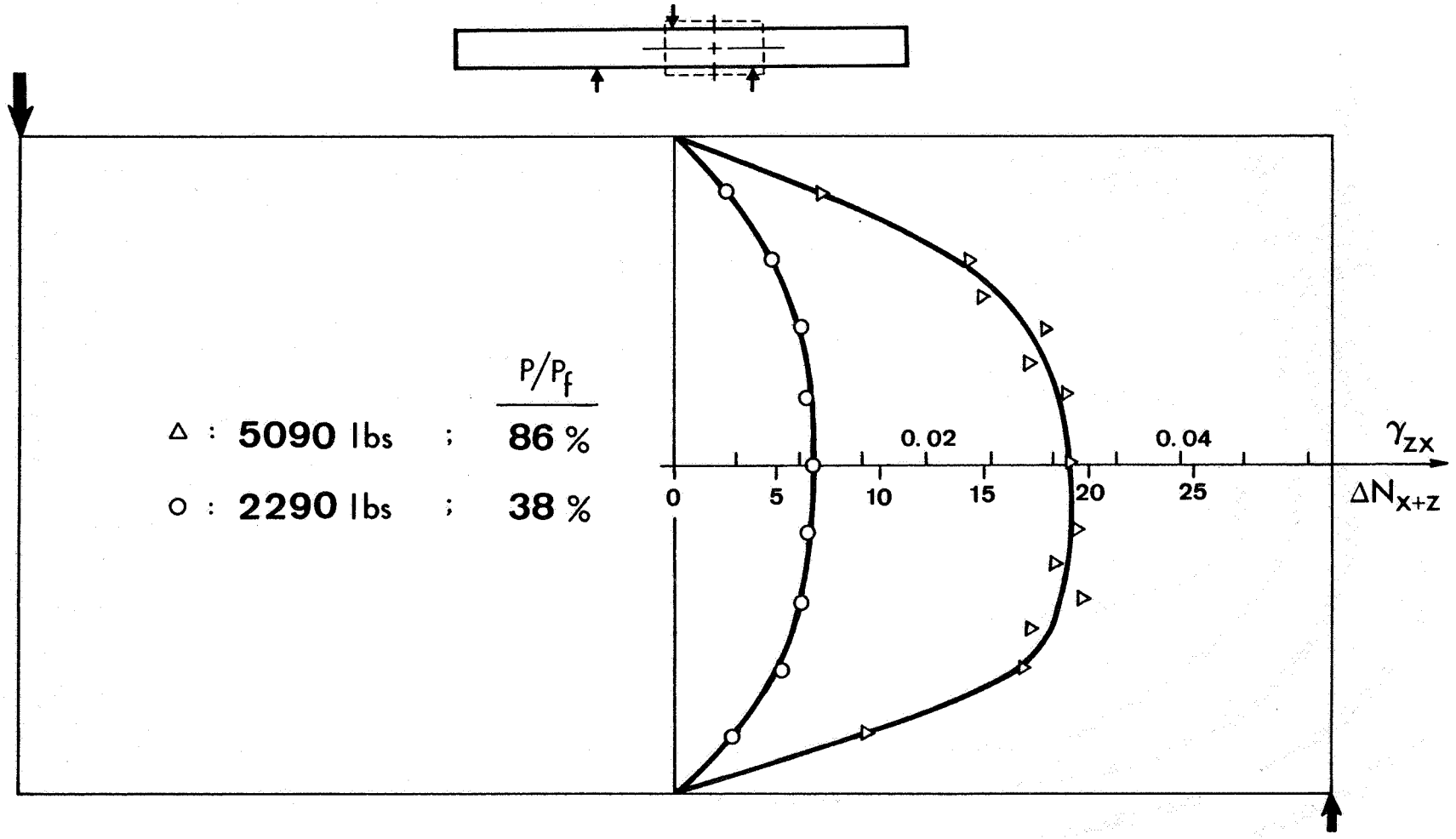

Fig. 13e$_1$ Shear strains (smoothed) along vertical centerline of bay denoted by dashed box.

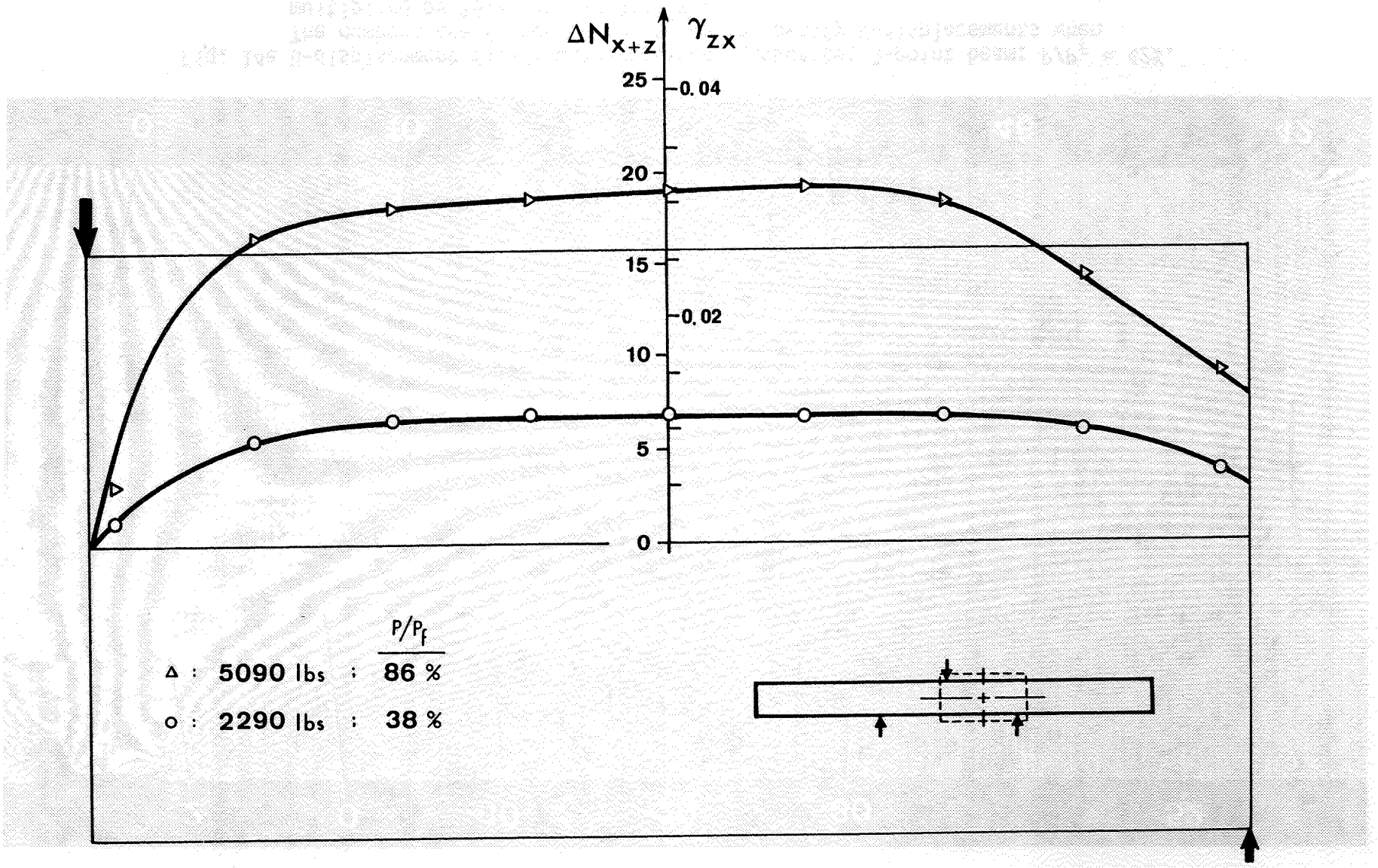

Fig. 13e$_2$ Shear strains (smoothed) along horizontal centerline of bay denoted by dashed box.

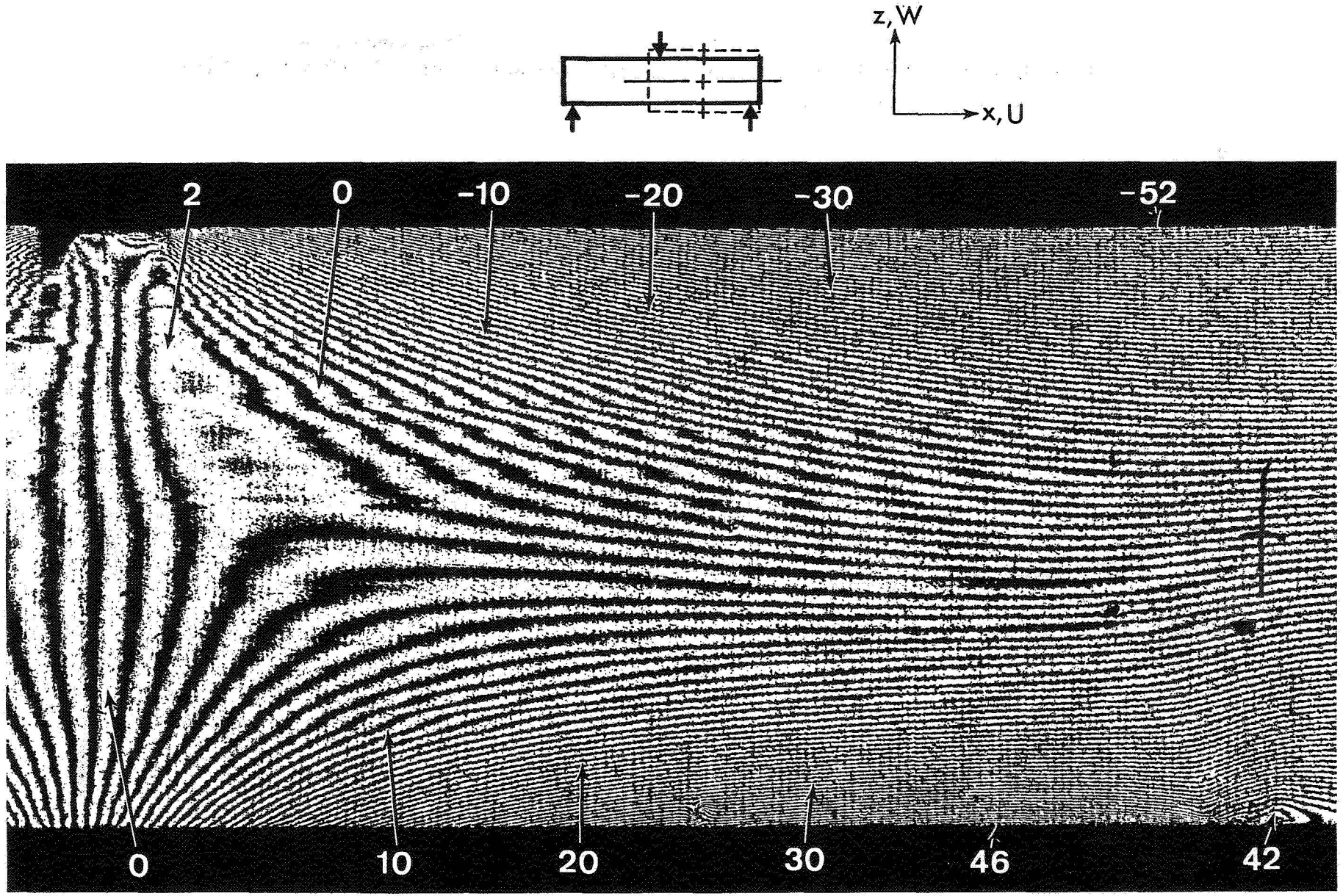

Fig. 14a U-displacement field; unidirectional composite; 3-point beam; P/P_f = 42%. The numbers are fringe orders N_x which specify U-displacements when multiplied by 16.4 μin. (0.417 μm).

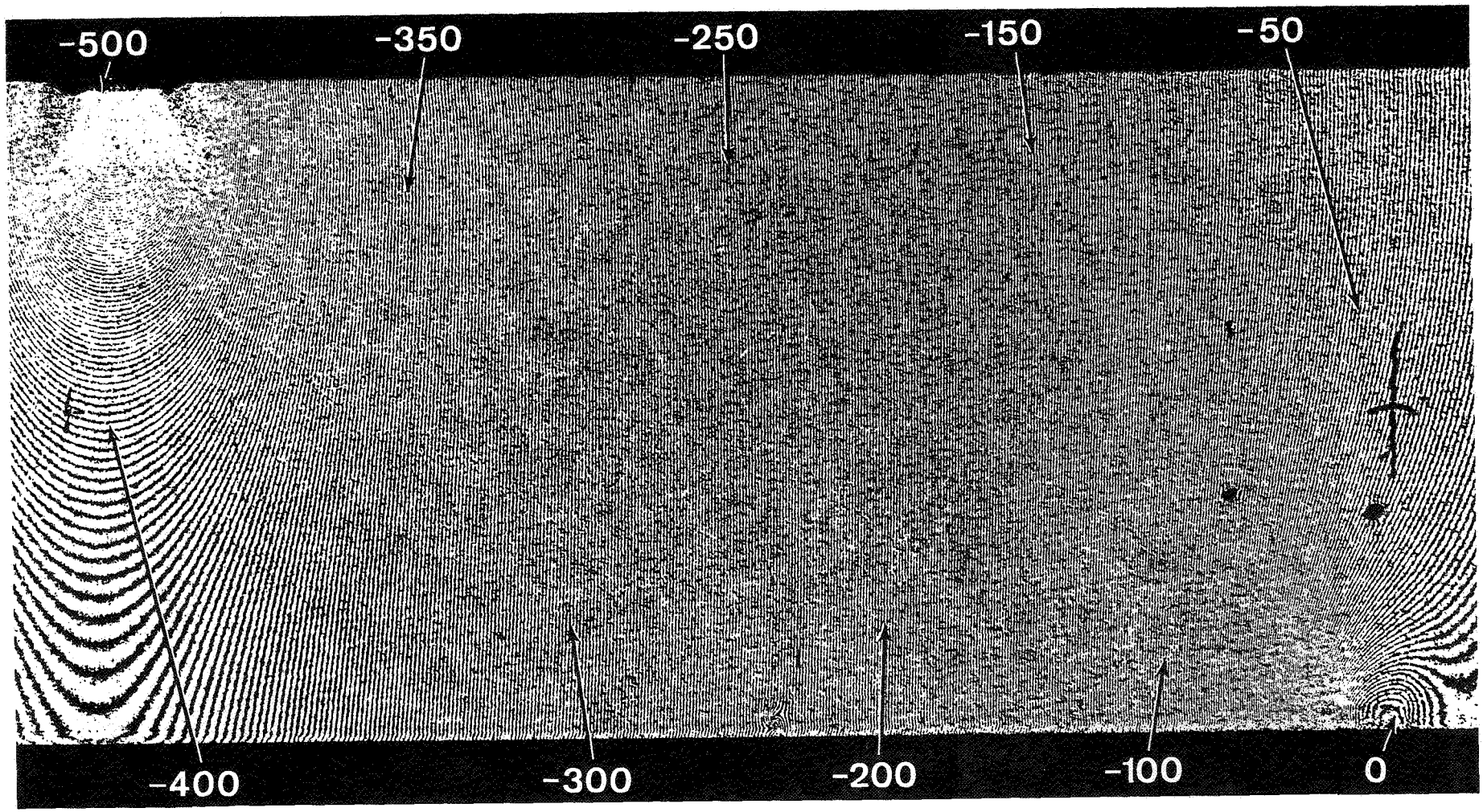

Fig. 14b W-displacement field; P/P_f = 42%. The numbers are fringe orders N_z which specify W-displacements when multiplied by 16.4 μin. (0.417 μm).

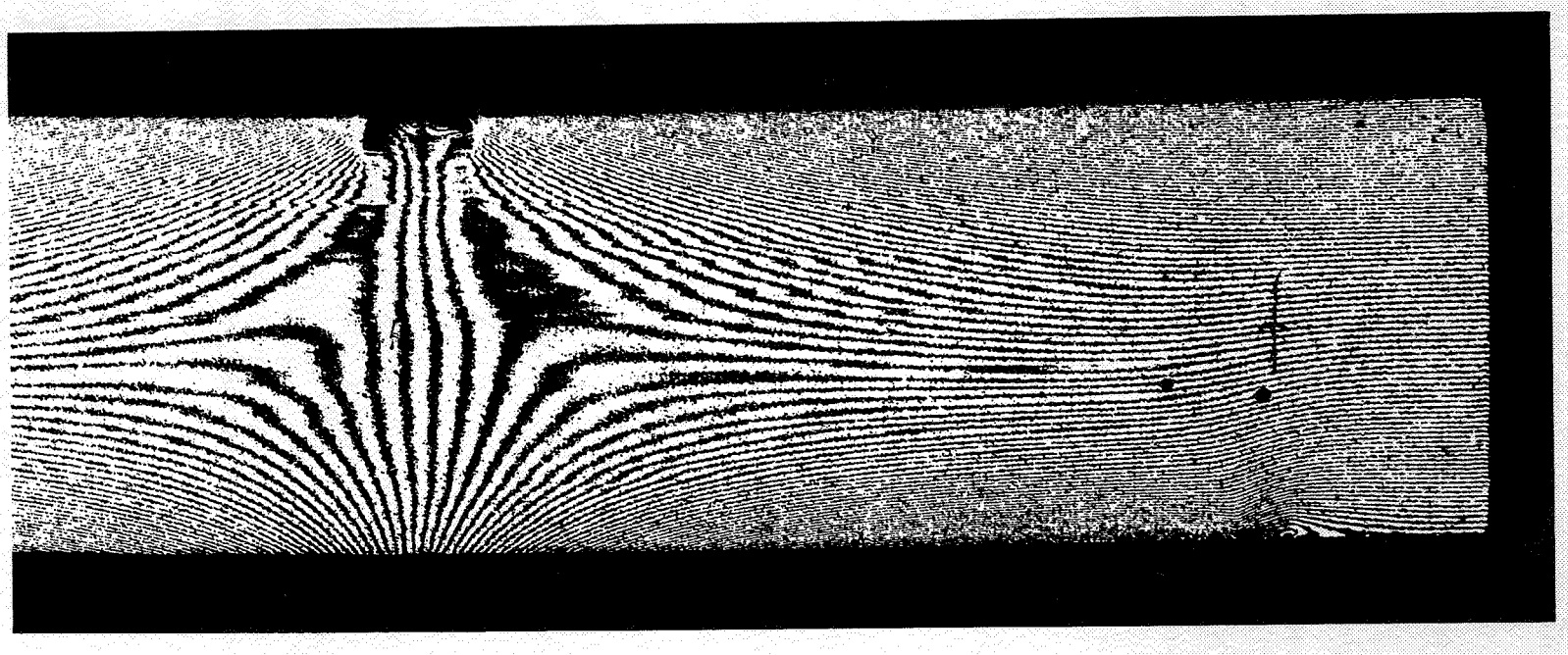

Fig. 14c U-displacement field, multiple bays; P/P_f = 42%.

Fig. 14d Contour map of shear strains γ_{zx} (smoothed); $\Delta x,z = 0.010$ in.; $P/P_f = 42\%$. The numbers are contour levels which signify shear strains when multiplied by 0.00167 m/m.

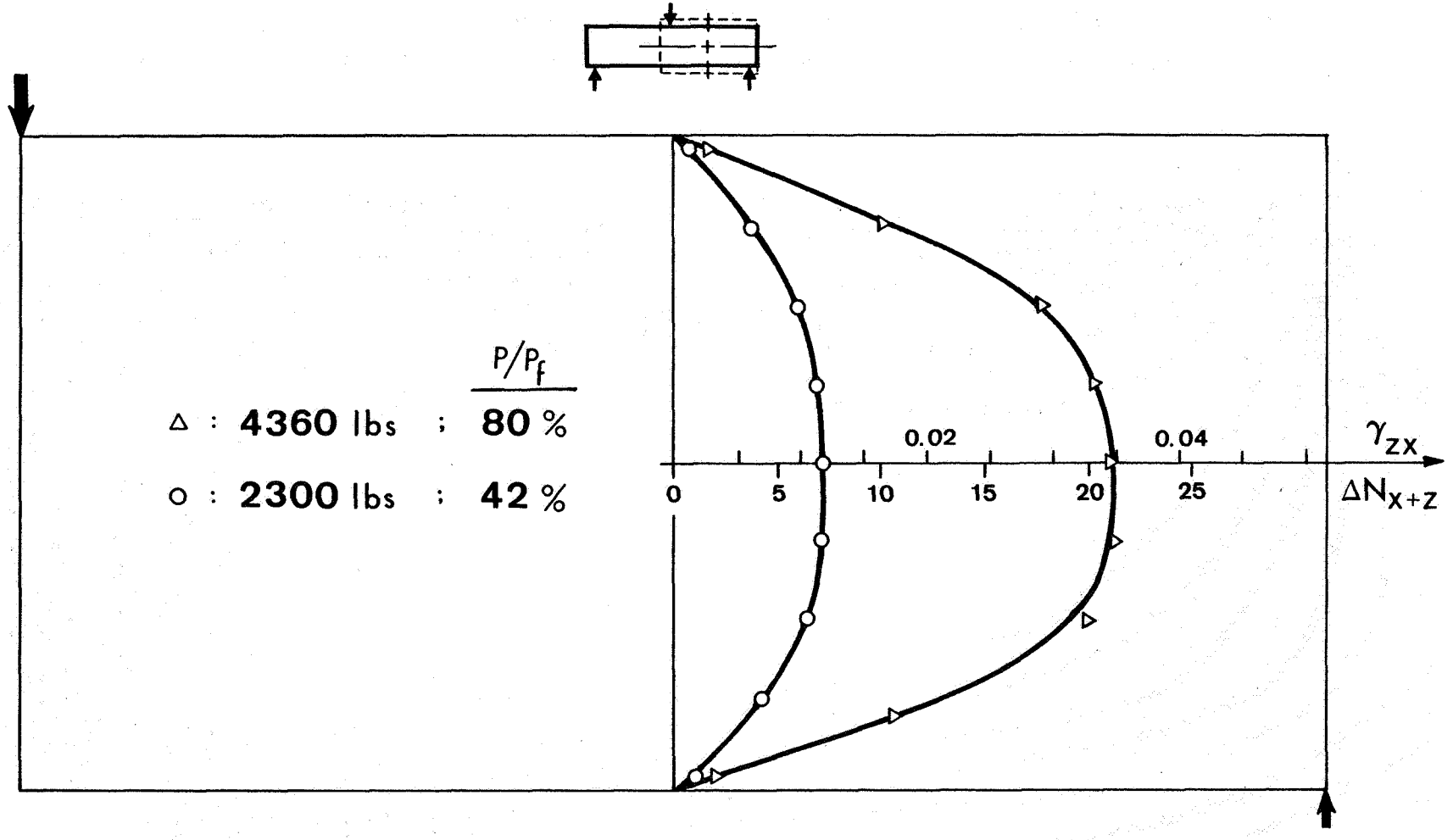

Fig. 14e$_1$ Shear strains (smoothed) along vertical centerline of bay denoted by dashed box.

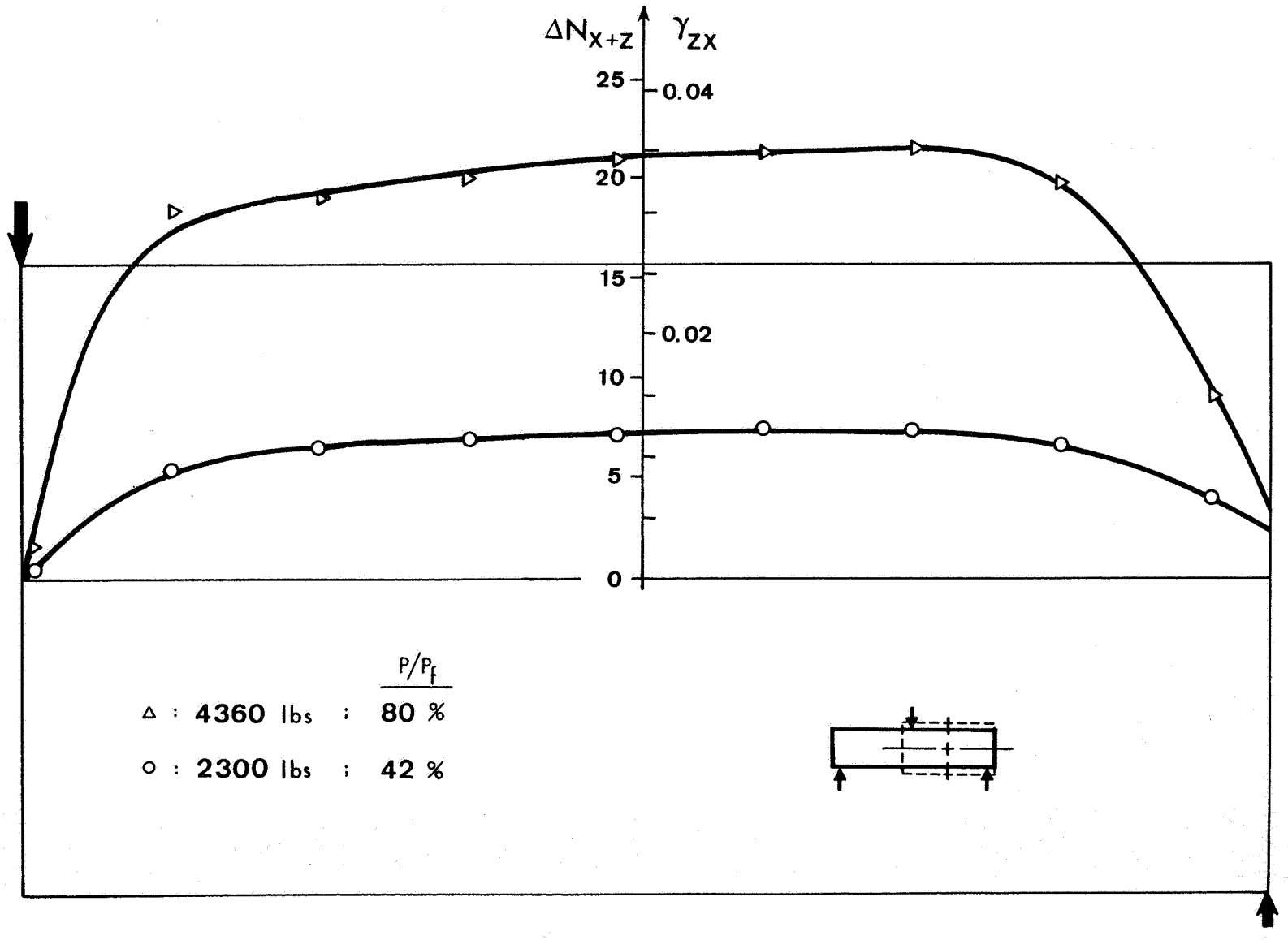

Fig. 14e$_2$ Shear strains (smoothed) along horizontal centerline of bay denoted by dashed box.

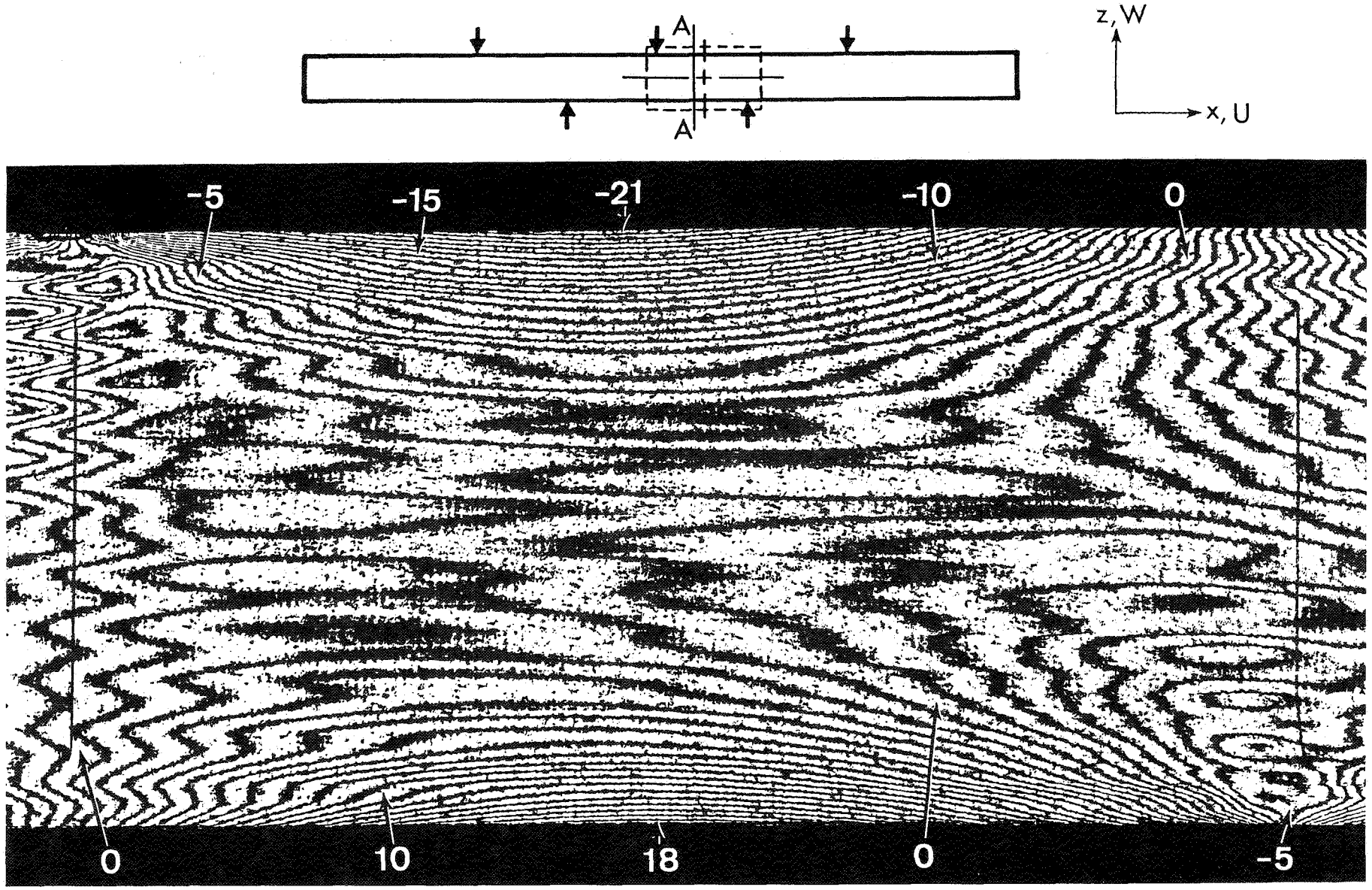

Fig. 15a U-displacement field; quasi-isotropic composite; 5-point beam; P/P_f = 50%. The numbers are fringe orders N_x which specify U-displacements when multiplied by 16.4 μin. (0.417 μm).

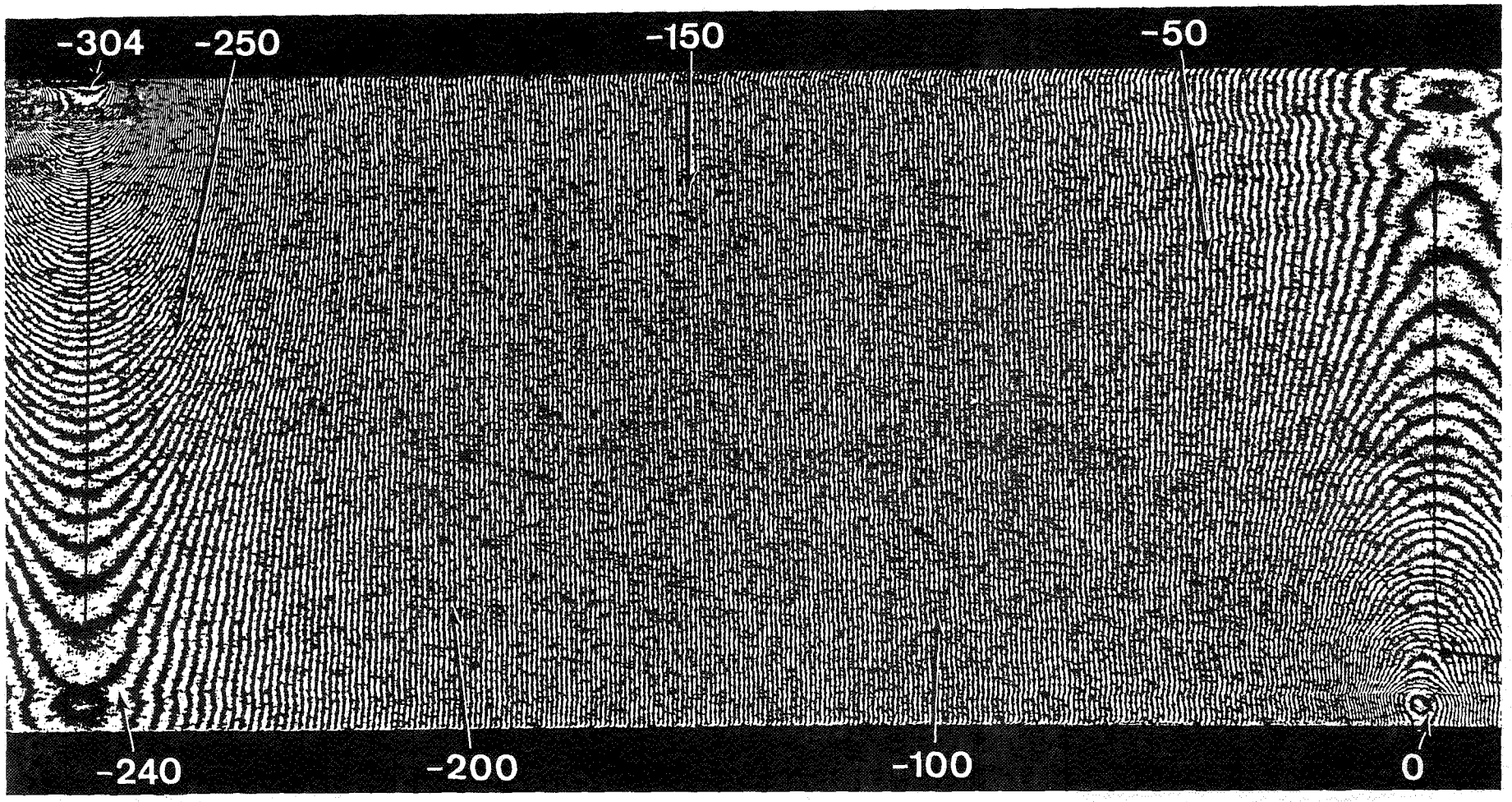

Fig. 15b W-displacement field; P/P_f = 50%. The numbers are fringe orders N_z which specify W-displacements when multiplied by 16.4 μin. (0.417 μm).

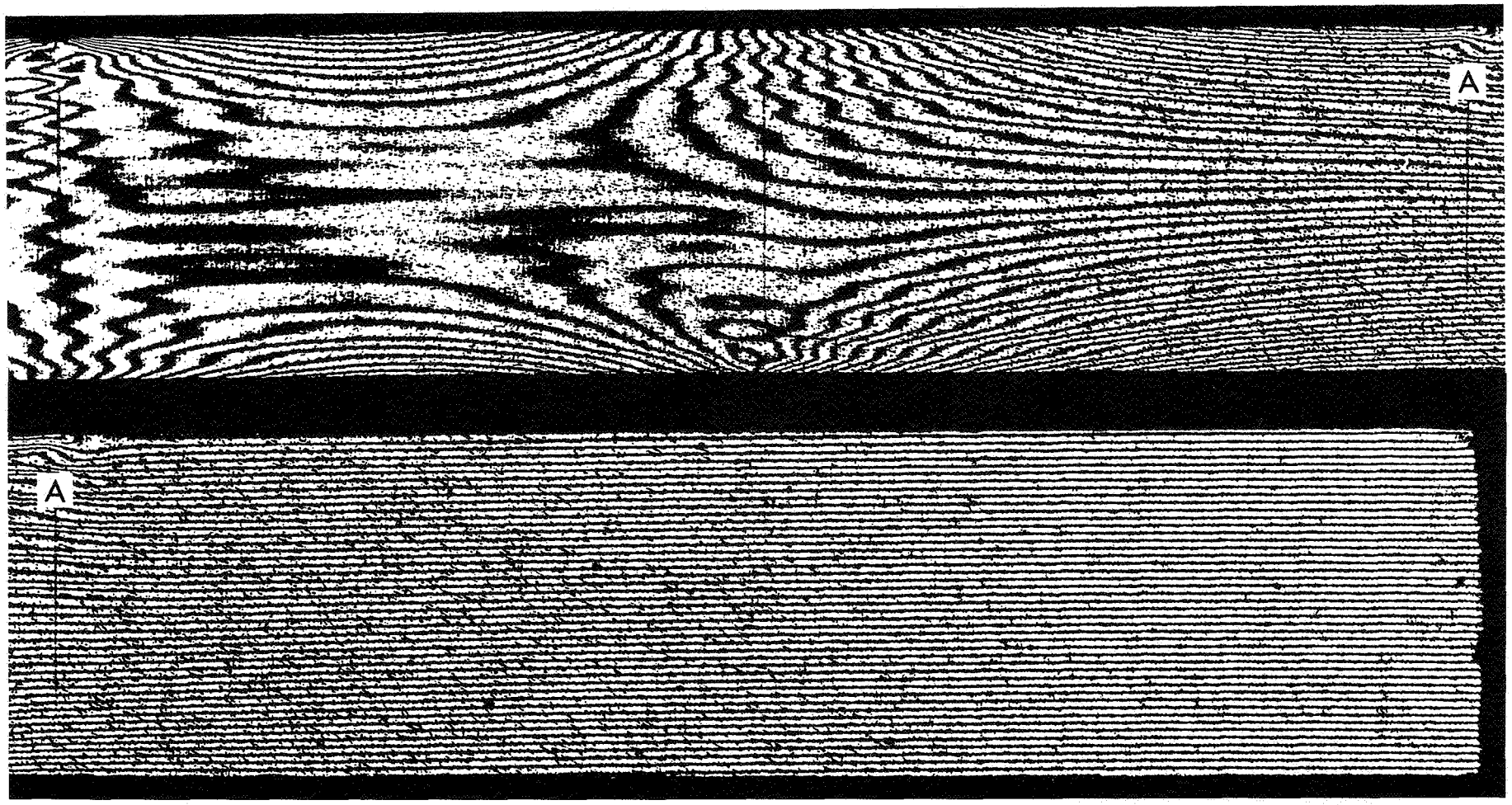

Fig. 15c U-displacement field, multiple bays; P/P_f = 29%.

Fig. 15d Contour map of shear strains γ_{zx} (smoothed); $\Delta x,z = 0.010$ in.; $P/P_f = 50\%$. The numbers are contour levels which signify shear strains when multiplied by 0.00167 m/m.

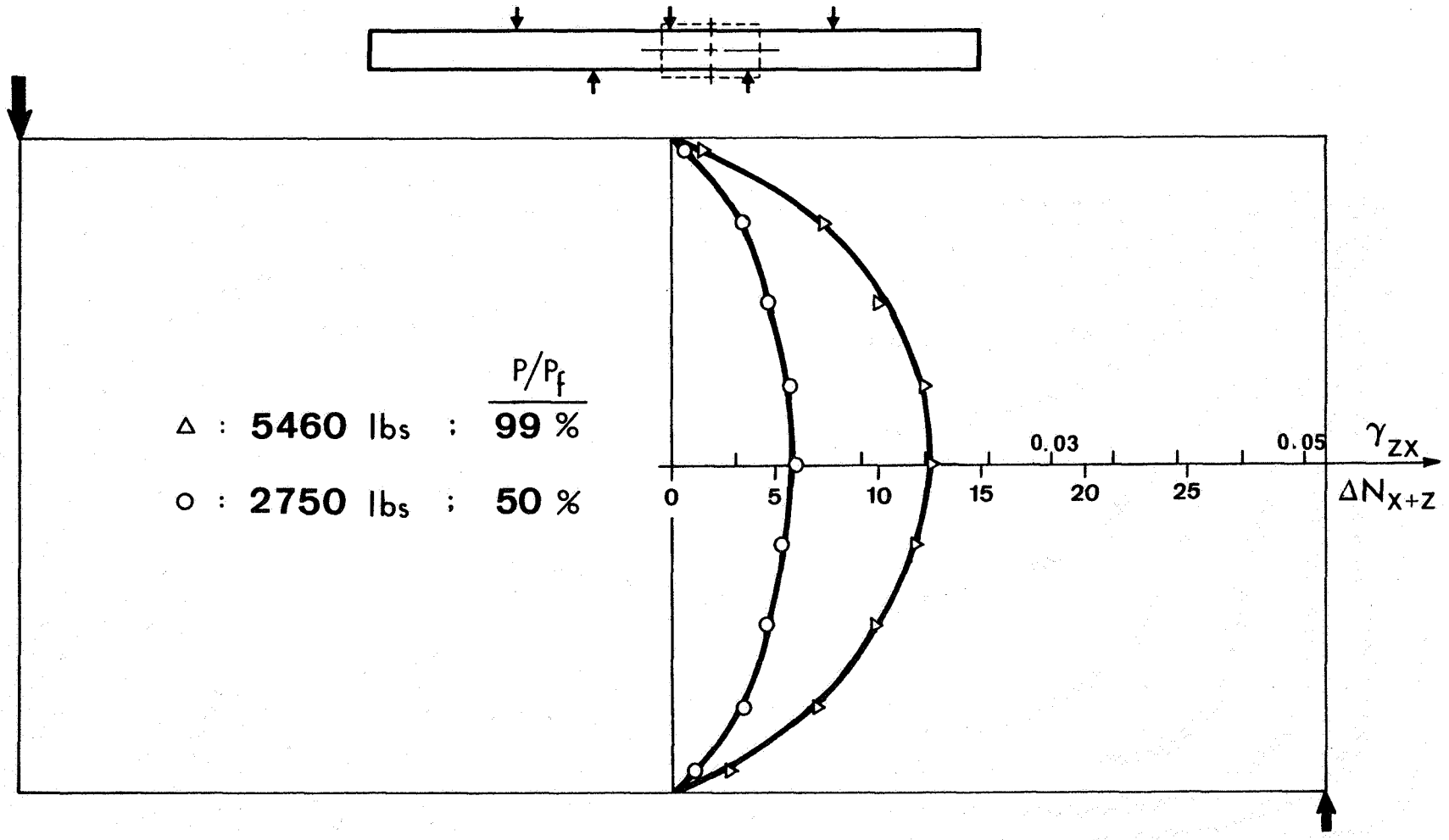

Fig. 15e$_1$ Shear strains (smoothed) along vertical centerline of bay denoted by dashed box.

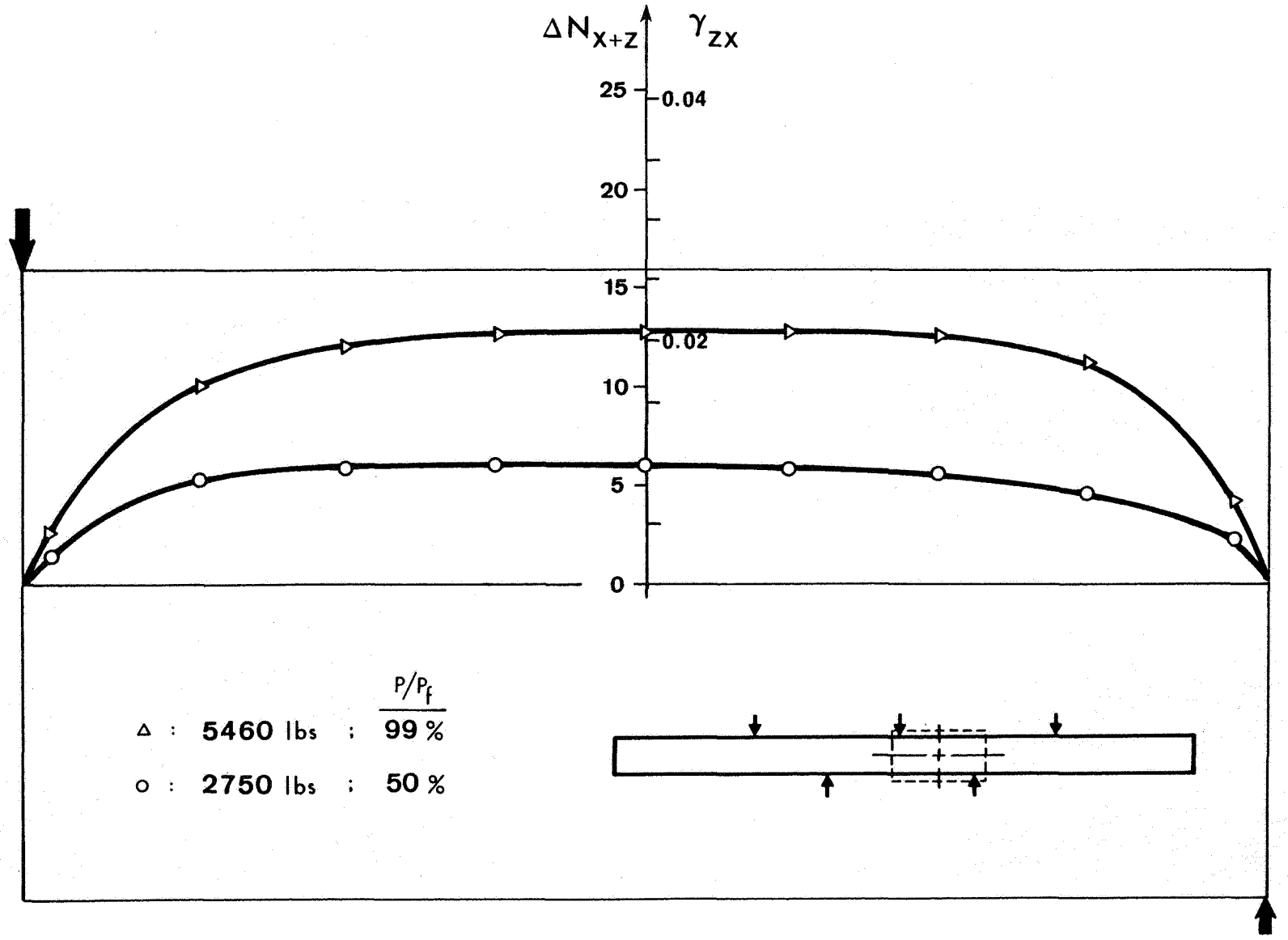

Fig. 15e$_2$ Shear strains (smoothed) along horizontal centerline of bay denoted by dashed box.

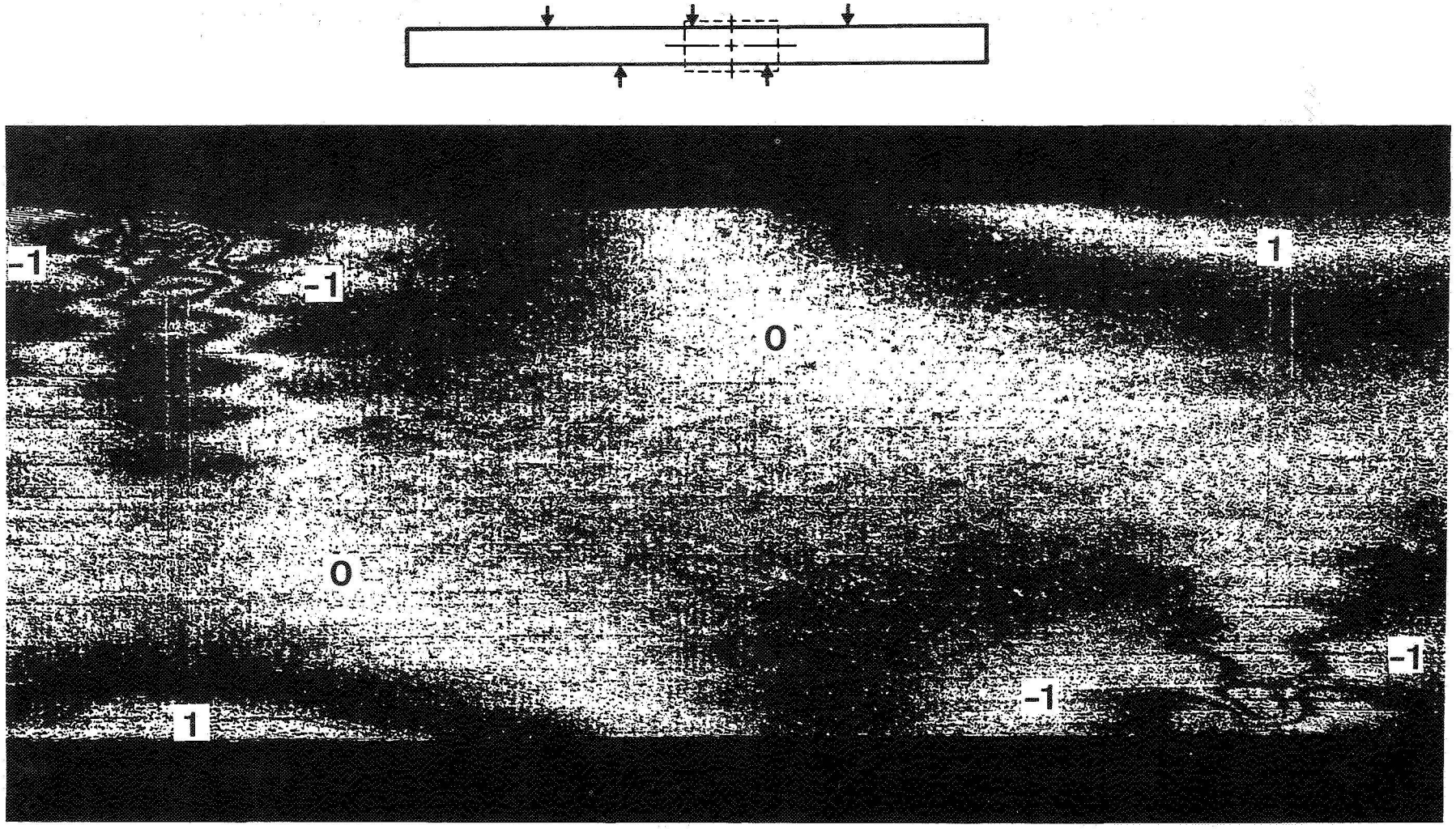

Fig. 15i Pattern of ε_x or $\Delta U/\Delta x$ by mechanical differentiation; Δx = 0.010 in.; P/P_f = 50%. The numbers are fringe orders which specify ε_z when multiplied by 0.00167 m/m.

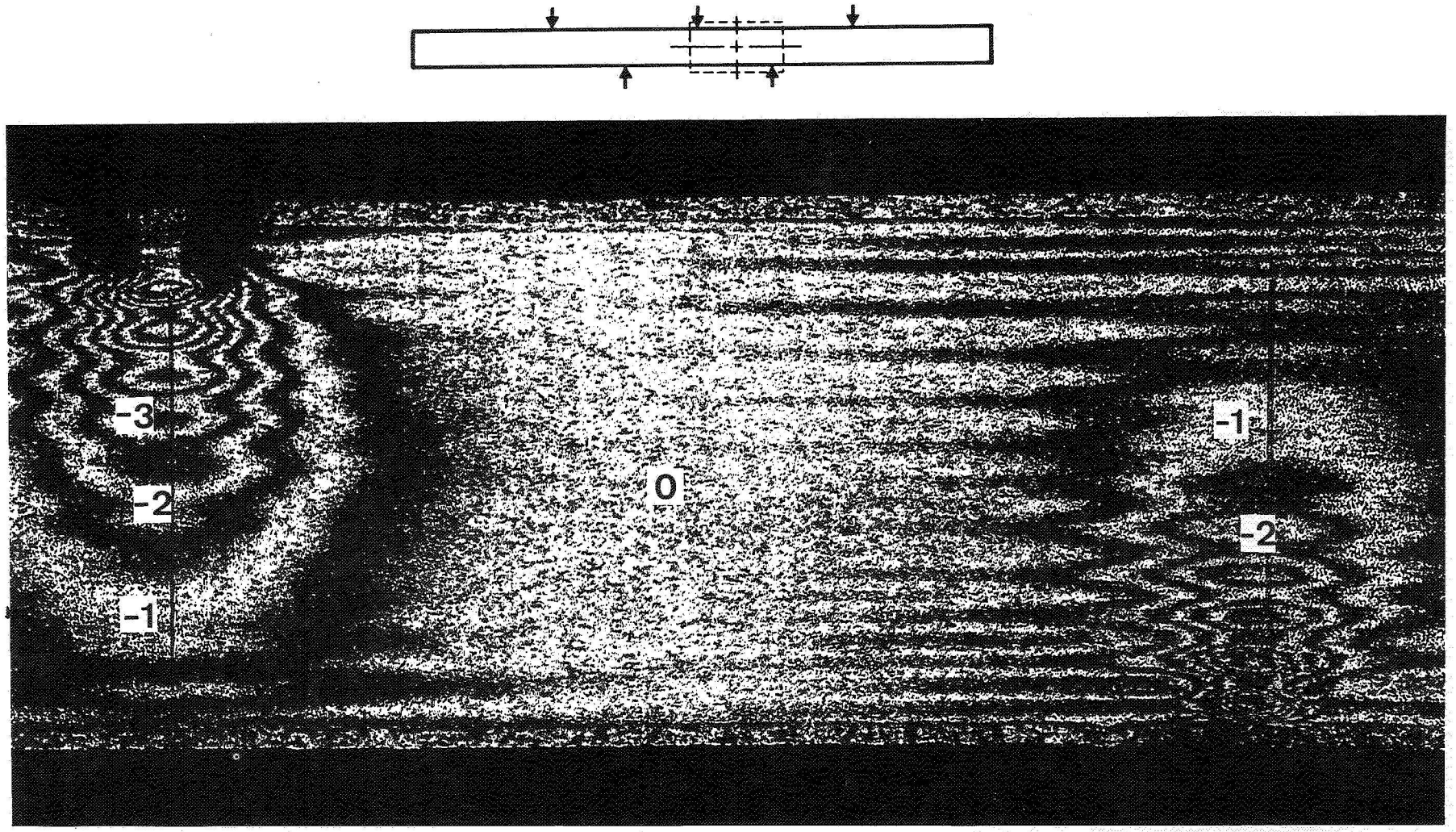

Fig. 15j Pattern of ε_z or $\Delta W/\Delta z$ by mechanical differentation; Δz = 0.010 in.; P/P_f = 50%. The numbers are fringe orders which specify ε_z when multiplied by 0.00167 m/m.

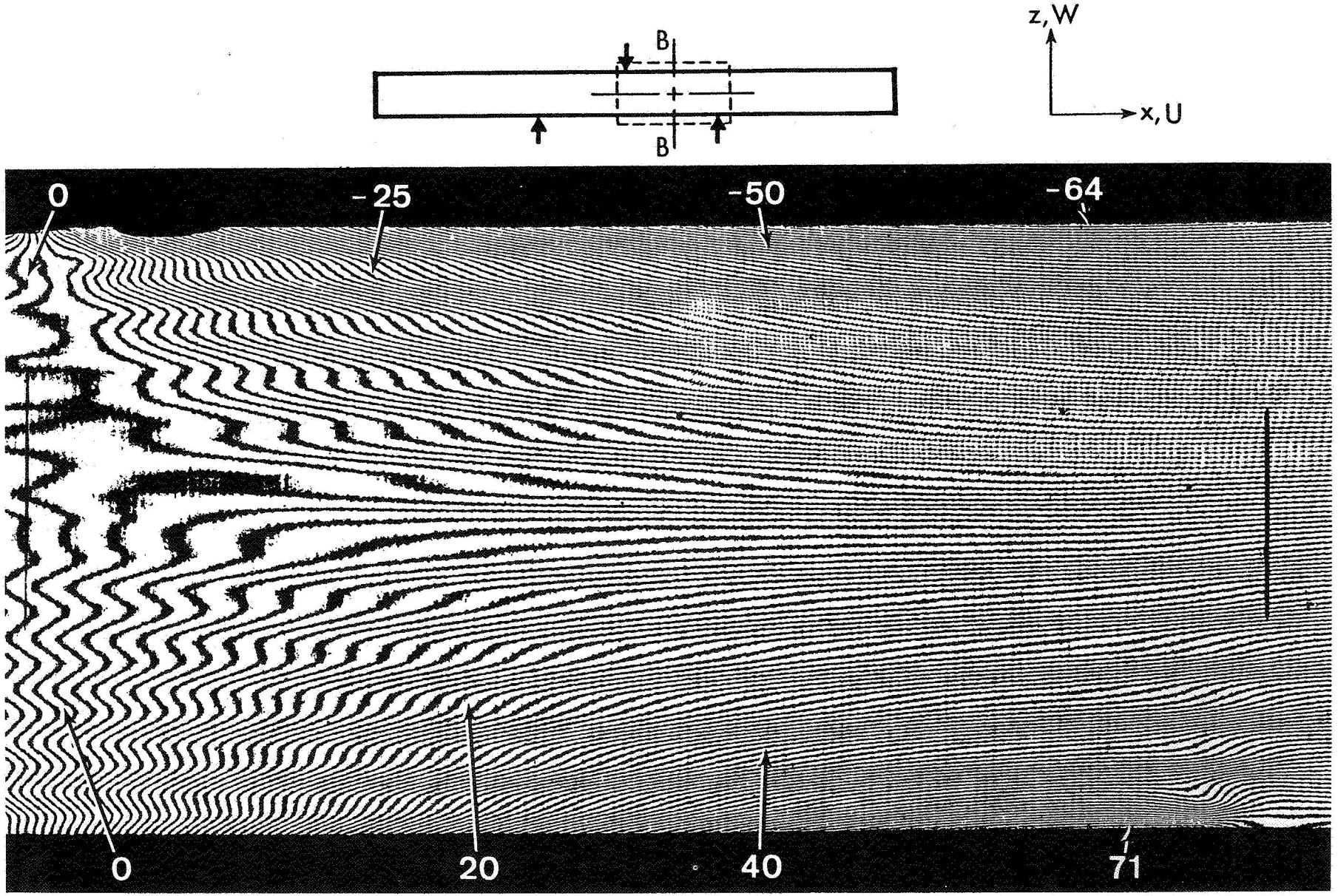

Fig. 16a U-displacement field; quasi-isotropic composite; 3-point beam with overhang; P/P_f = 38%. The numbers are fringe orders N_x which specify U-displacements when multiplied by 16.4 μin. (0.417 μm).

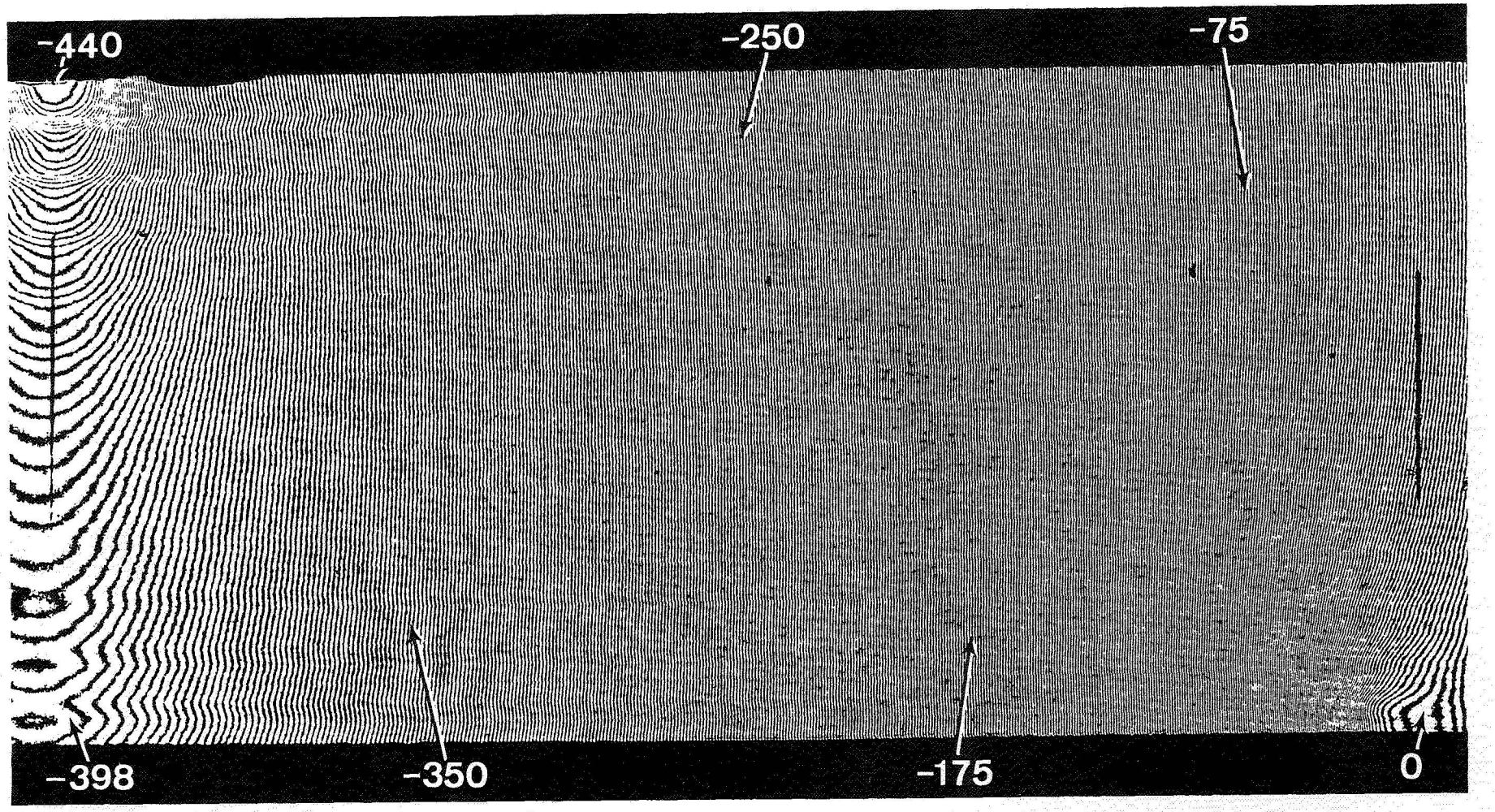

Fig. 16b W-displacement field; P/P_f = 38%. The numbers are fringe orders N_z which specify W-displacements when multiplied by 16.4 μin. (0.417 μm).

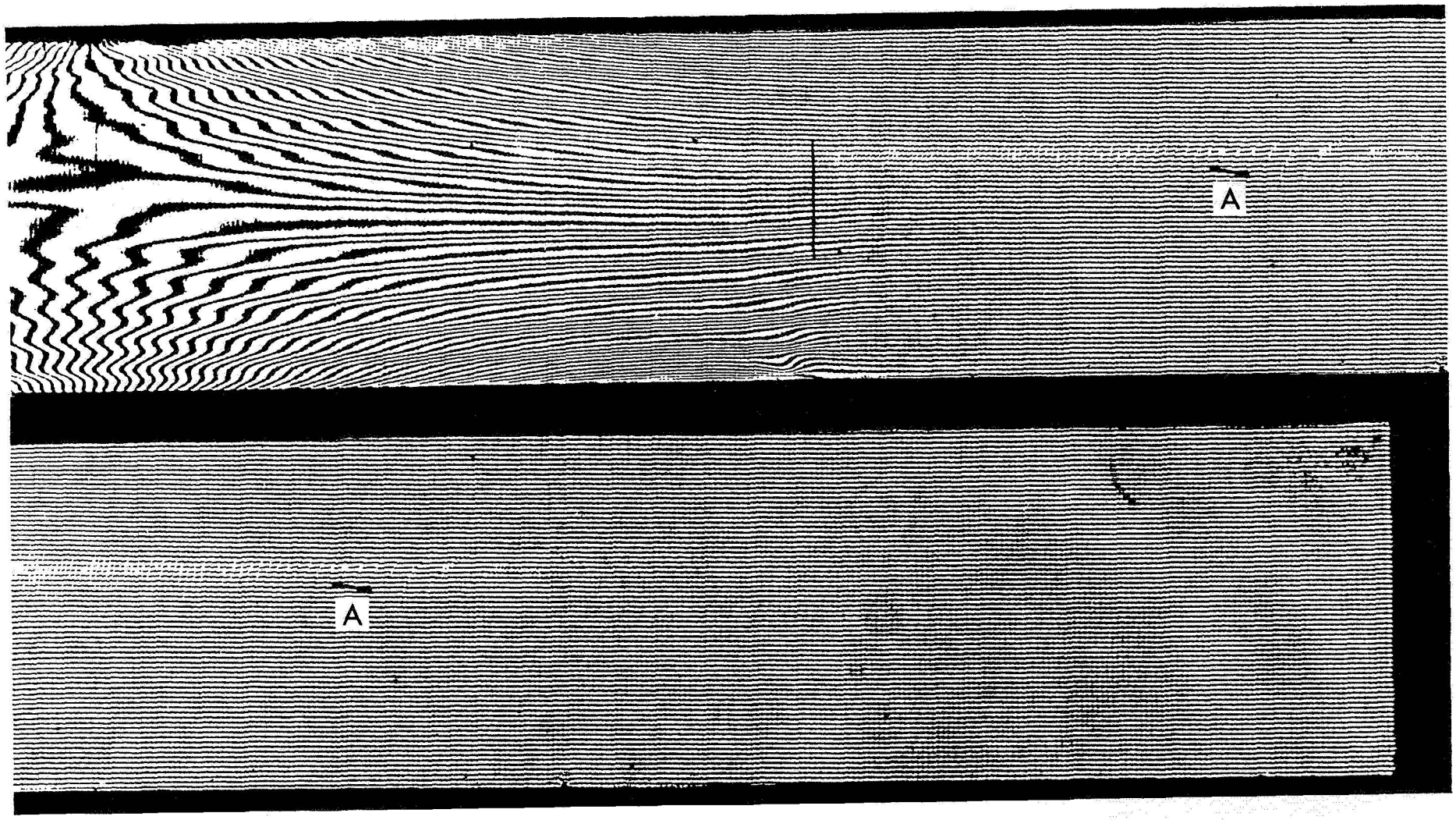

Fig. 16c U-displacement field, multiple bays; P/P_f = 19%.

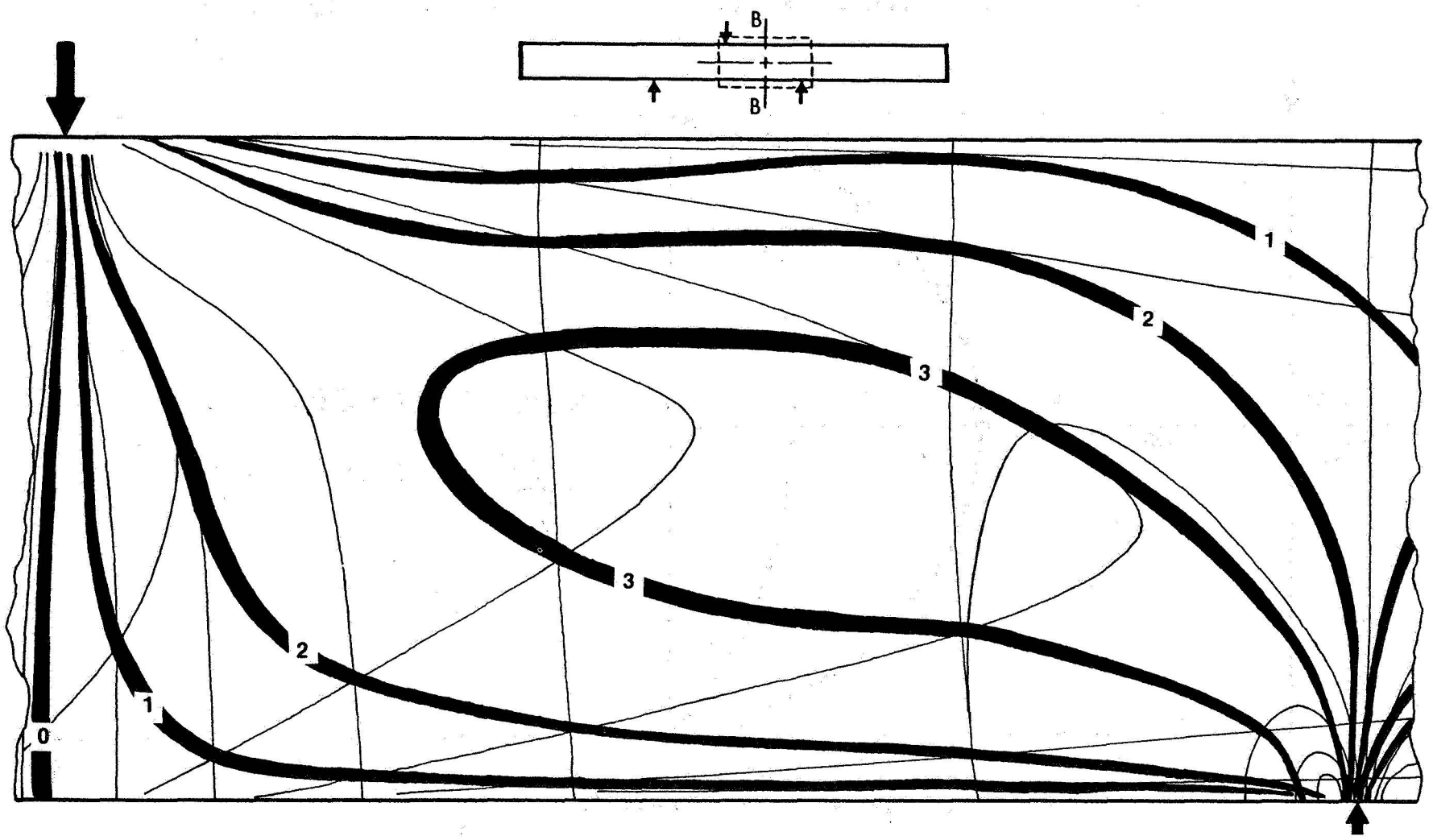

Fig. 16d Contour map of shear strains γ_{zx} (smoothed); $\Delta x,z$ = 0.005 in.; P/P_f = 38%. The numbers are contour levels which specify shear strains when multiplied by 0.00333 m/m.

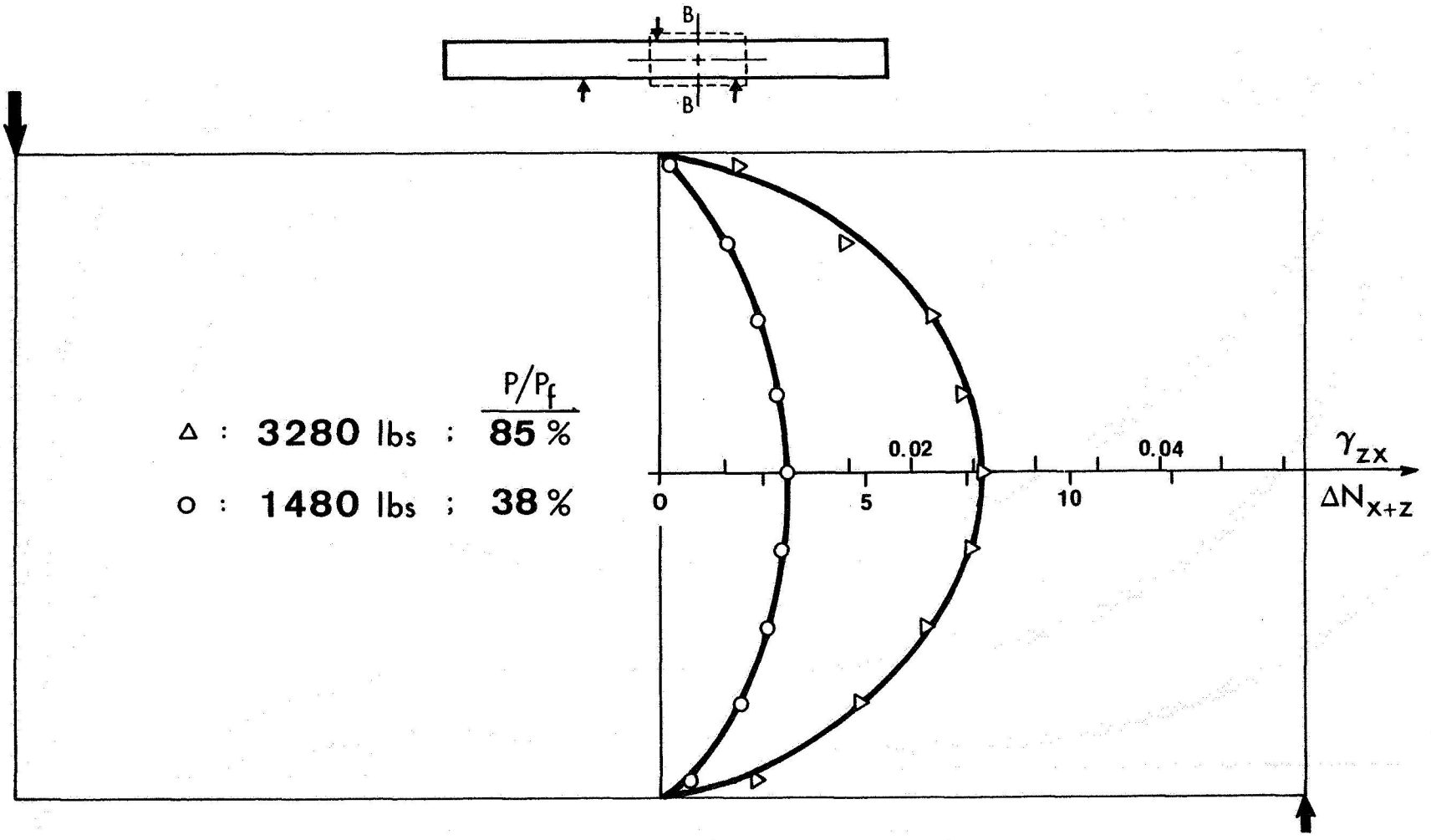

Fig. 16e$_1$ Shear strains (smoothed) along vertical centerline of bay denoted by dashed box.

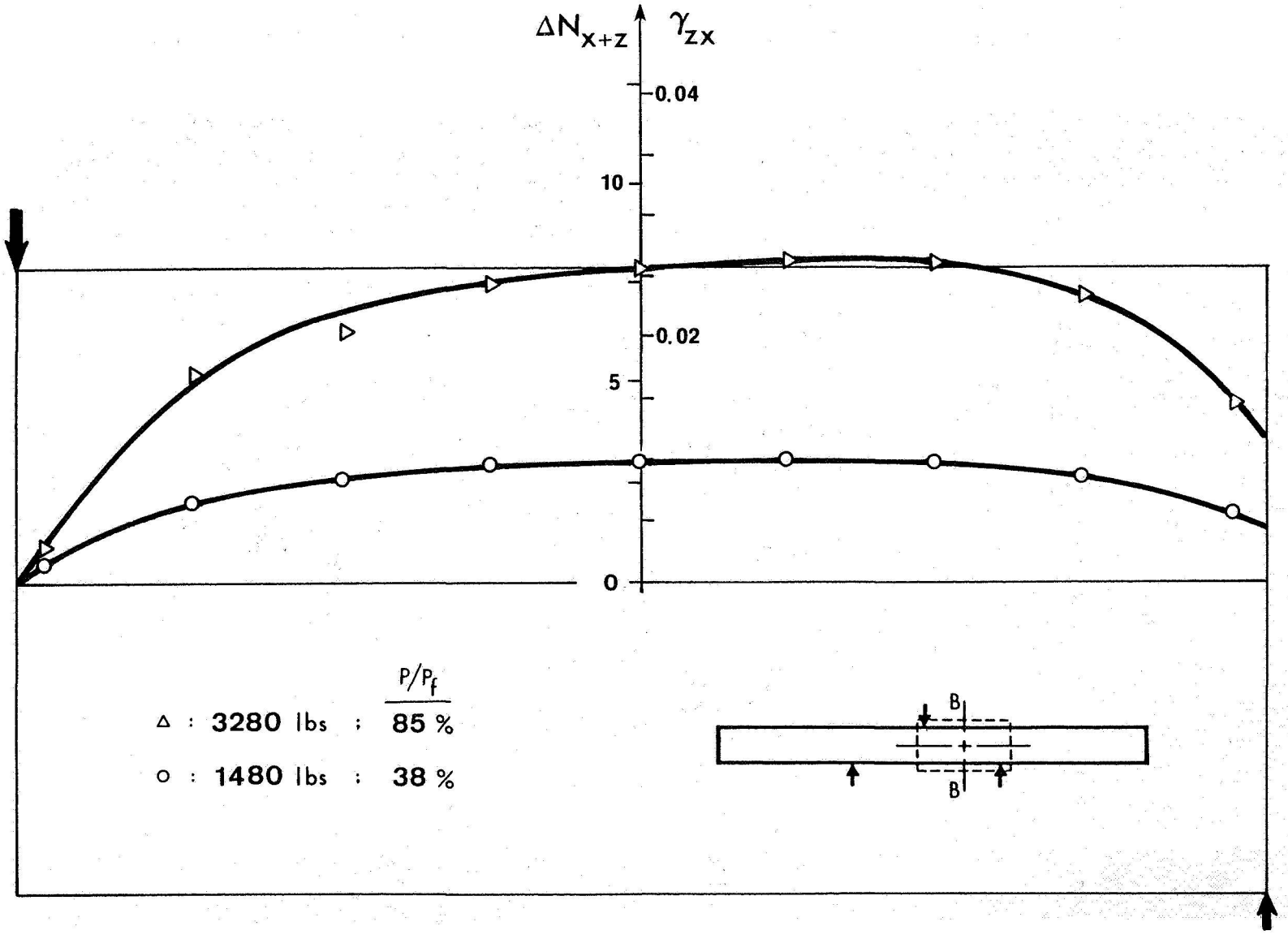

Fig. 16e$_2$ Shear strains (smoothed) along horizontal centerline of bay denoted by dashed box.

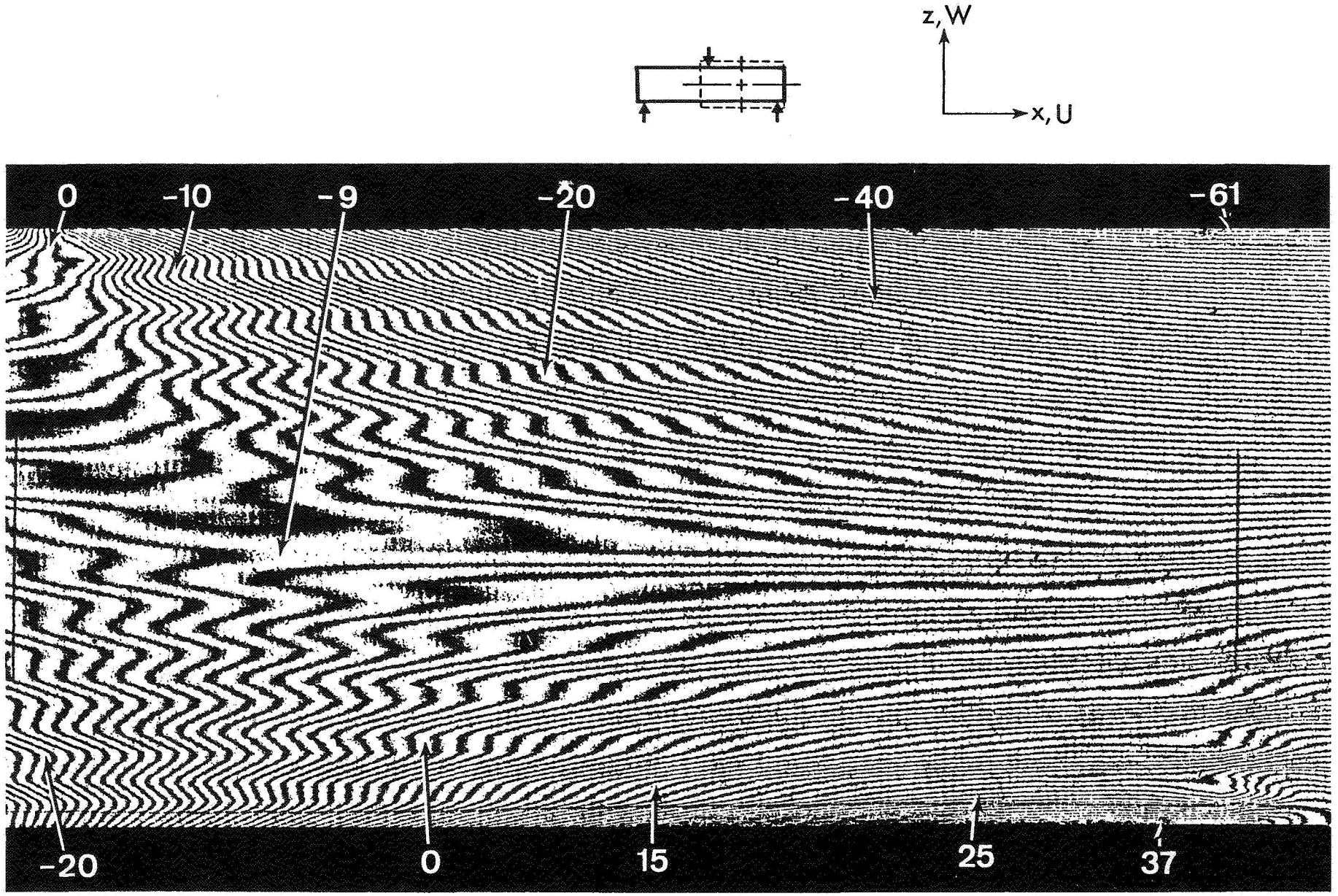

Fig. 17a U-displacement field; quasi-isotropic composite; 3-point beam; P/P_f = 36%. The numbers are fringe orders N_x which specify U-displacements when multiplied by 16.4 μin. (0.417 μm).

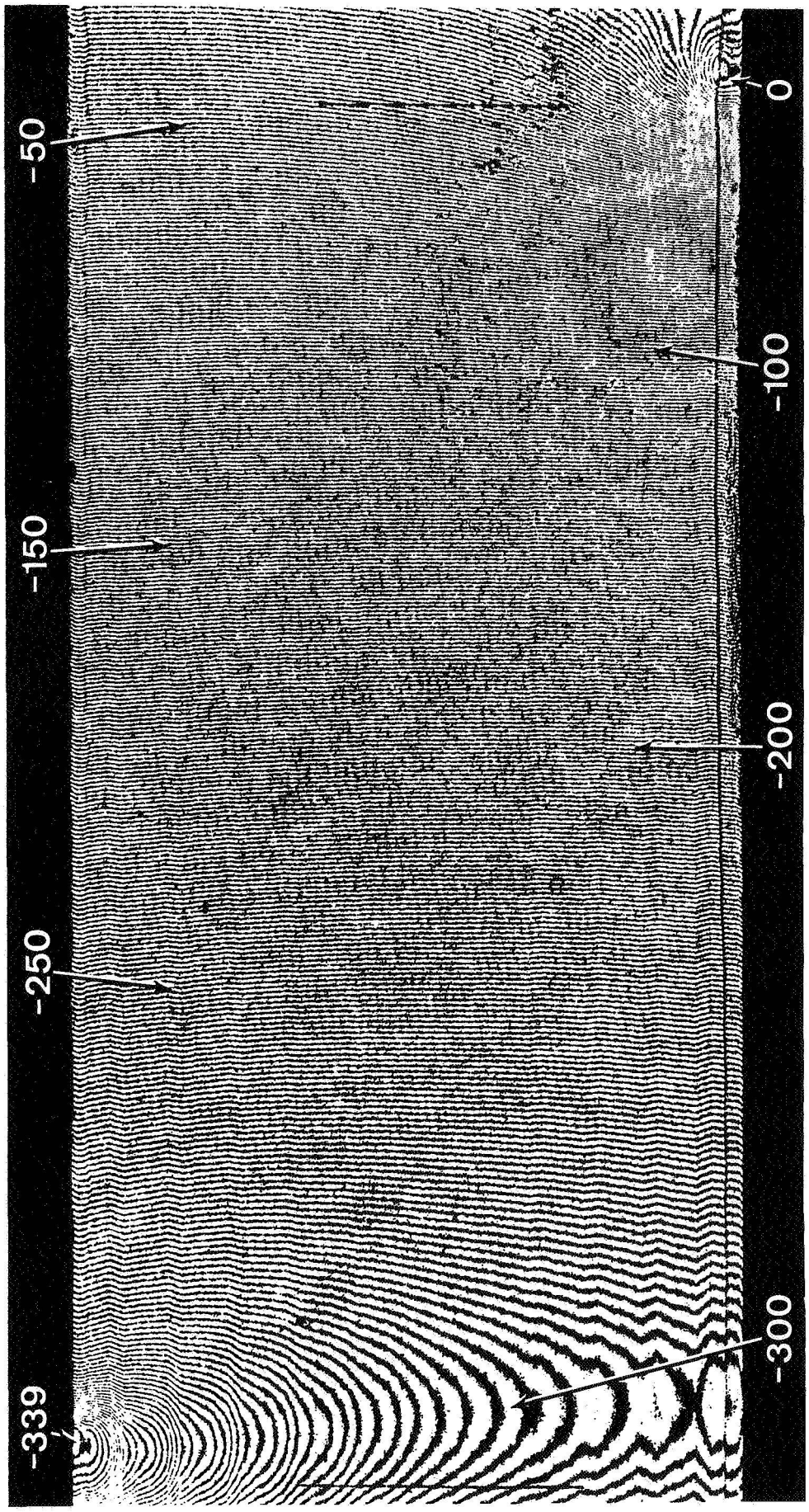

Fig. 17b W-displacement field; P/P_f = 36%. The numbers are fringe orders N_z which specify W-displacements when multiplied by 16.4 μin. (0.417 μm).

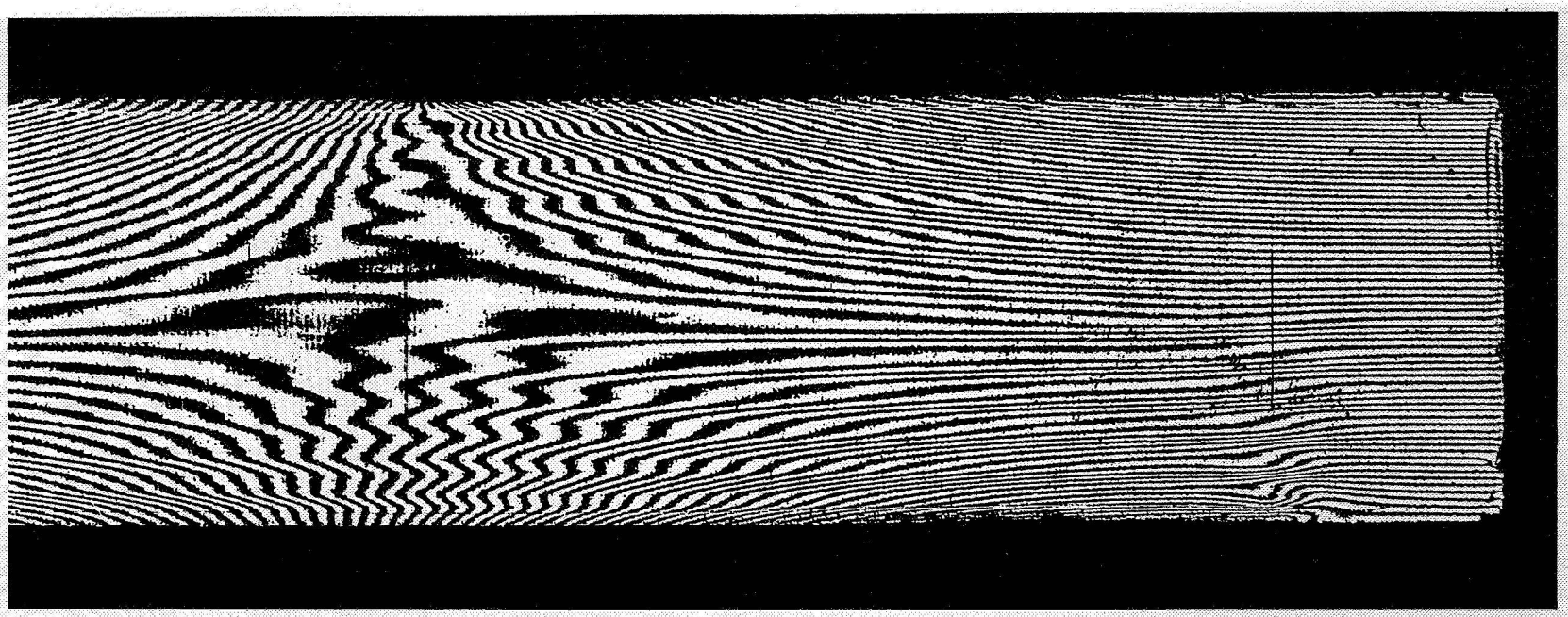

Fig. 17c U-displacement field, multiple bays; P/P_f = 18%.

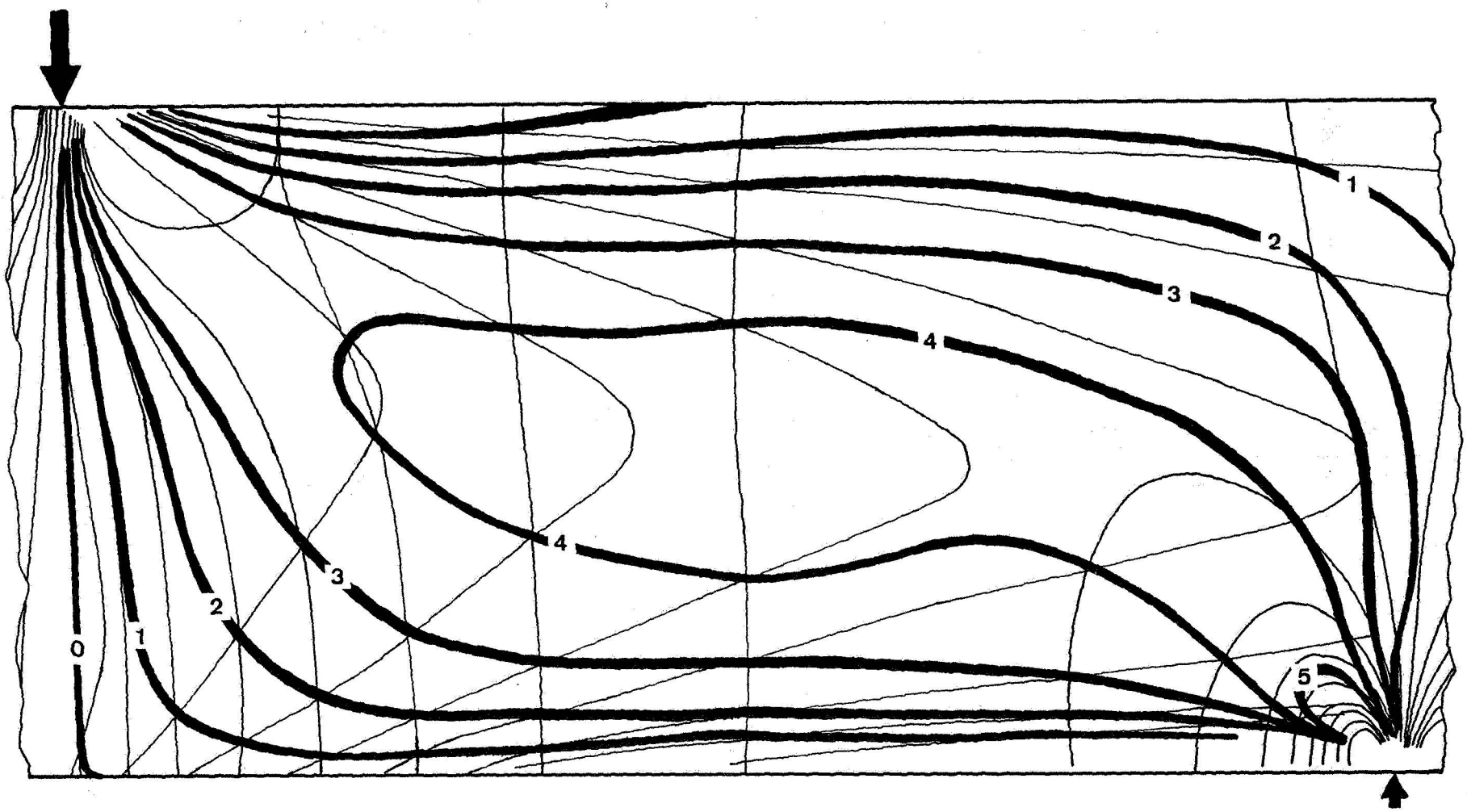

Fig. 17d Contour map of shear strains γ_{zx} (smoothed); $\Delta x,z = 0.010$ in.; $P/P_f = 36\%$. The numbers are contour levels which signify shear strains when multiplied by 0.00167 m/m.

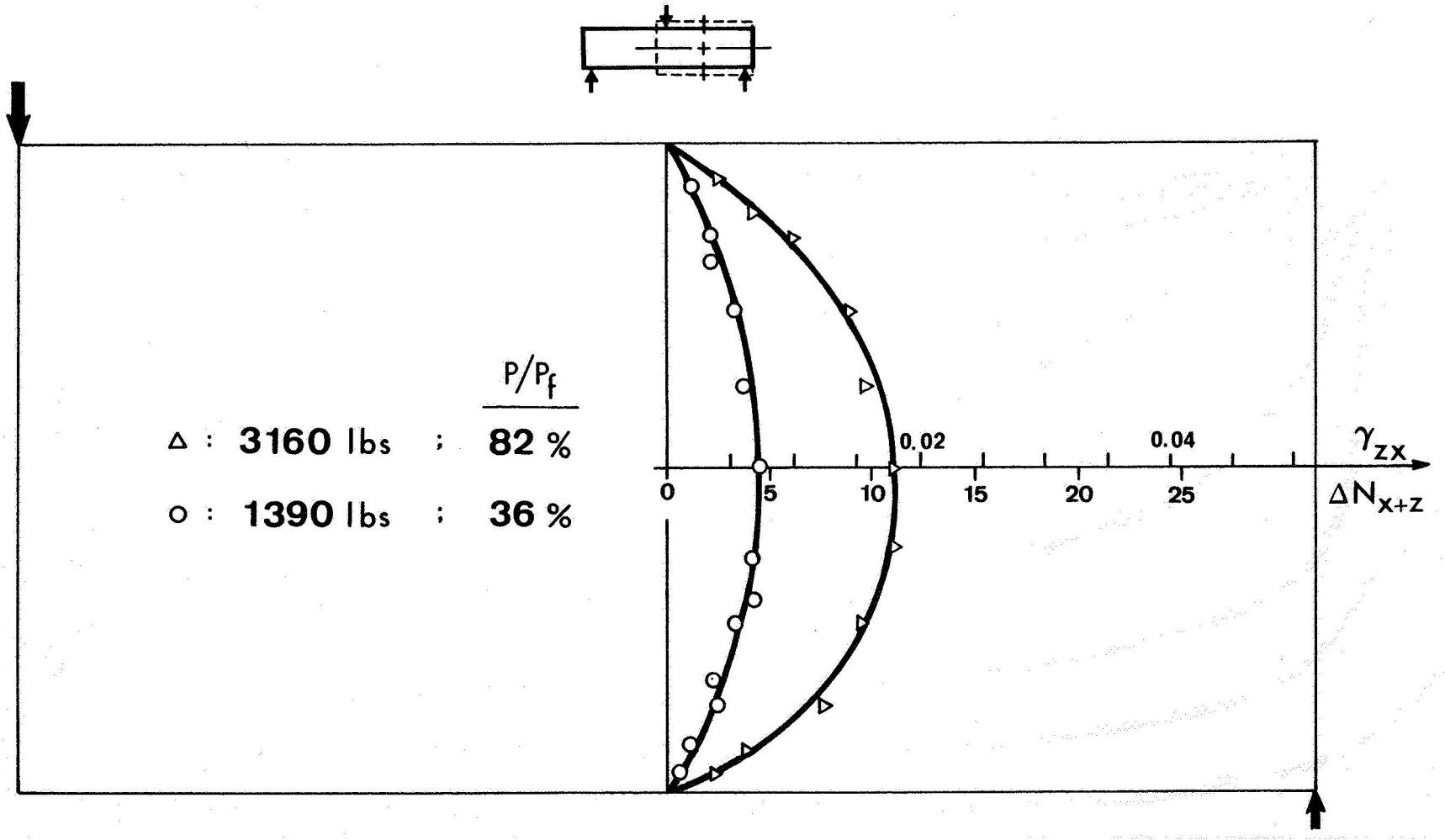

Fig. 17e$_1$ Shear strains (smoothed) along vertical centerline of bay denoted by dashed box.

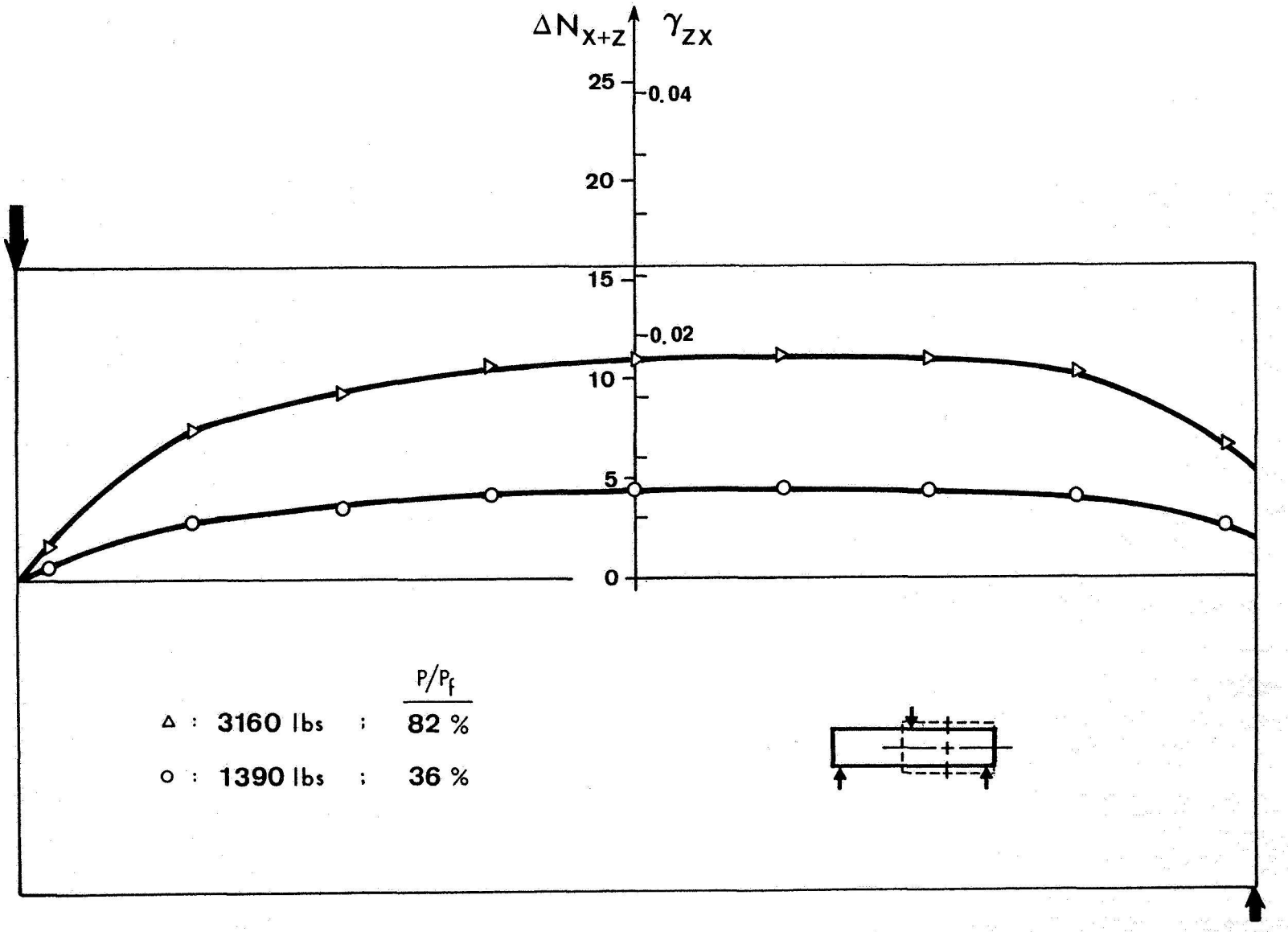

Fig. 17e$_2$ Shear strains (smoothed) along horizontal centerline of bay denoted by dashed box.

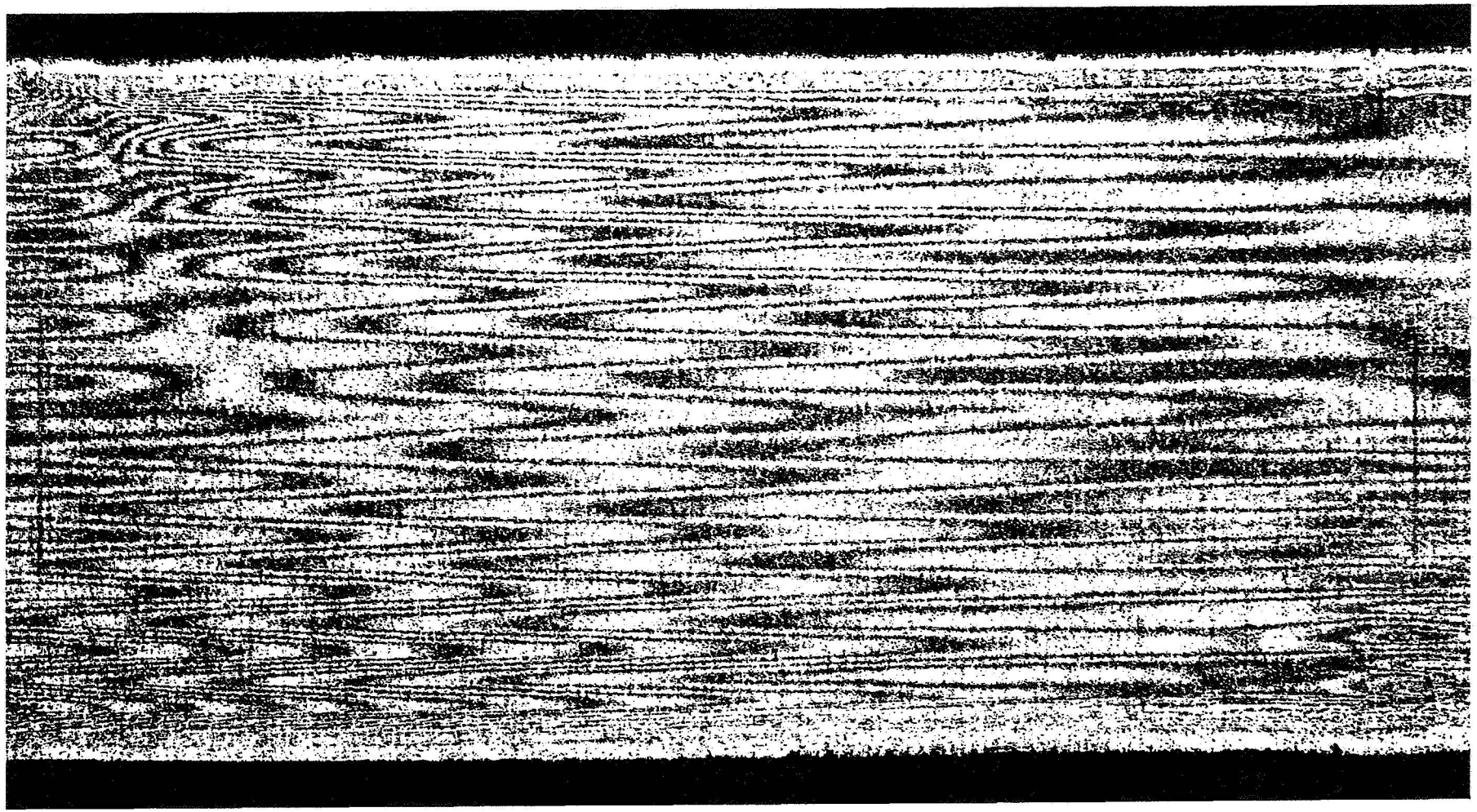

Fig. 17f Pattern of $\Delta U/\Delta z$ by mechanical differentiation; Δz = 0.010 in.; P/P_f = 36%.

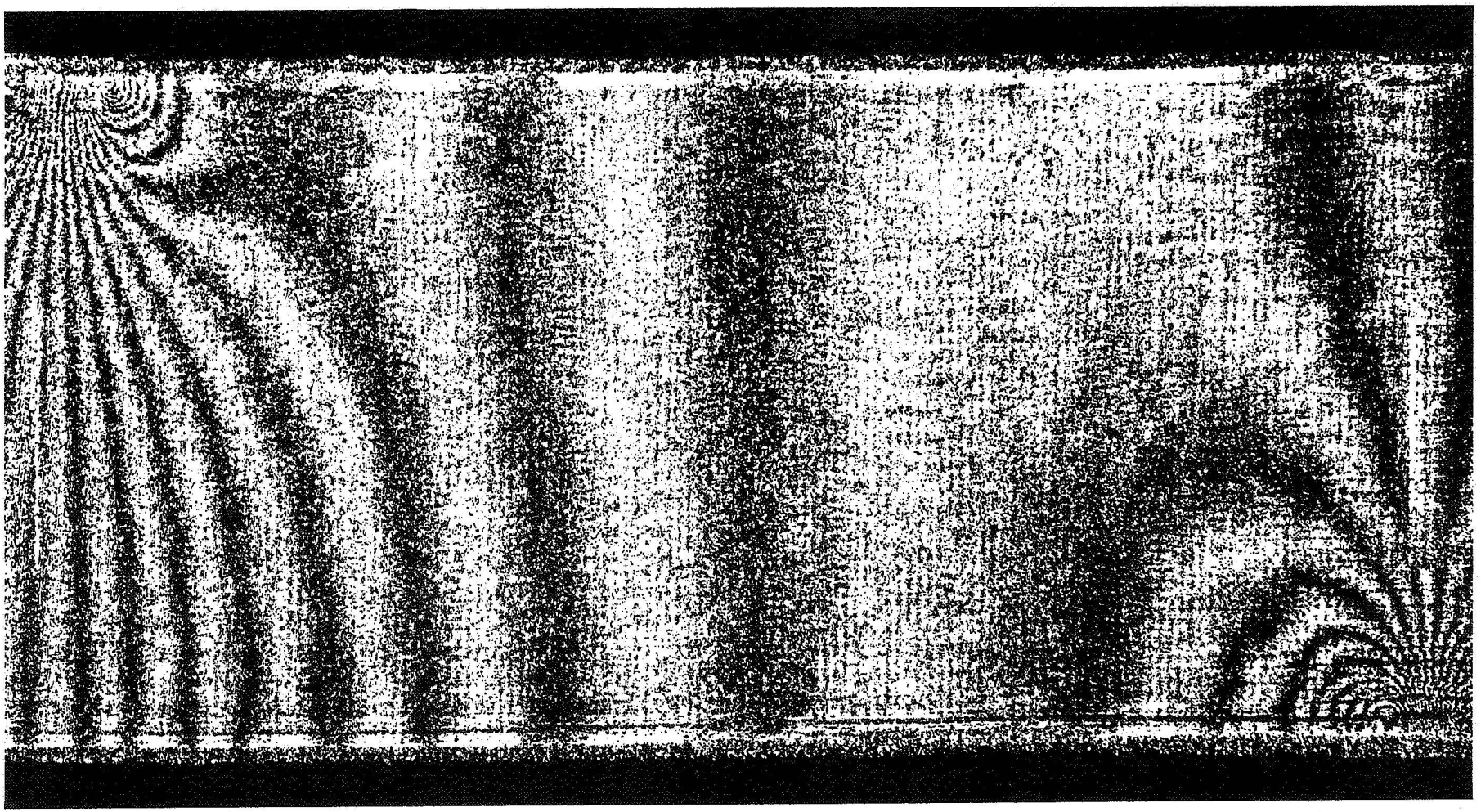

Fig. 17g Pattern of $\Delta W/\Delta x$ by mechanical differentiation; Δx = 0.010 in.; P/P_f = 36%.

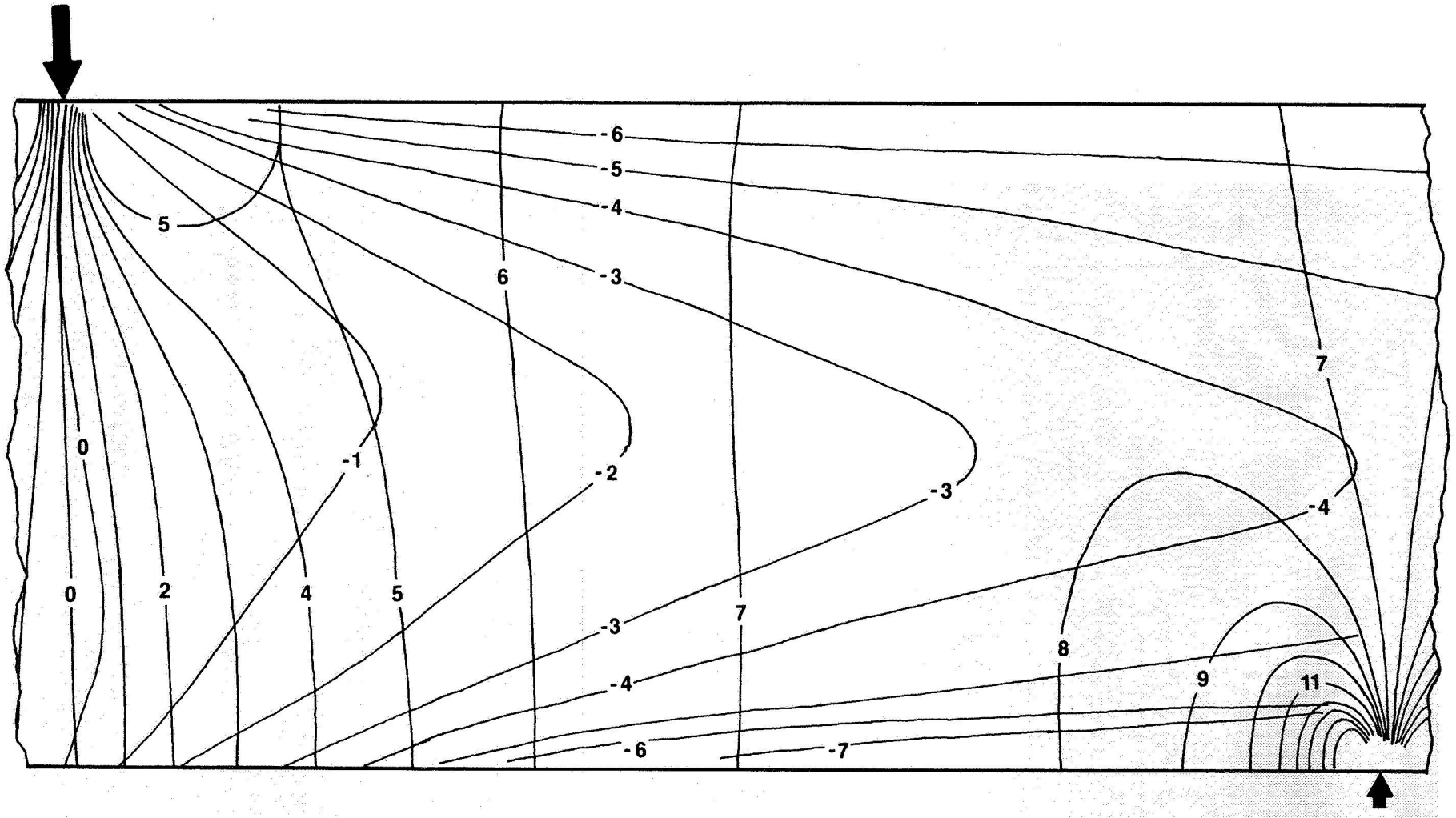

Fig. 17h Tracings of $\Delta U/\Delta z$ and $\Delta W/\Delta x$ contours; P/P_f = 36%. The numbers are contour levels which specify displacement gradients when multiplied by 0.00167 m/m.

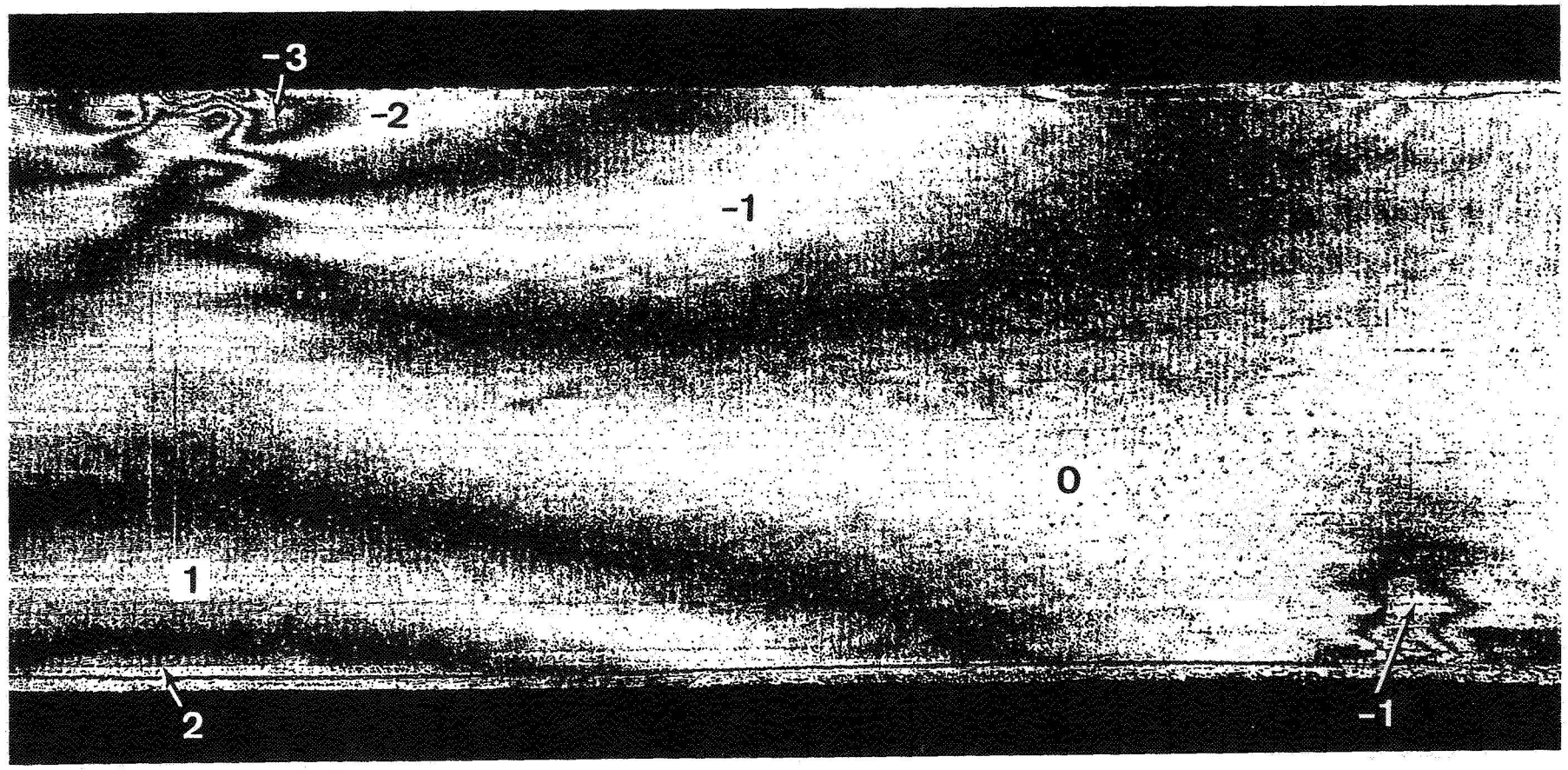

Fig. 17i Pattern of ε_x or $\Delta U/\Delta x$ by mechanical differentiation; Δx = 0.010 in.; P/P_f = 36%. The numbers are fringe orders which specify ε_z when multiplied by 0.00167 m/m.

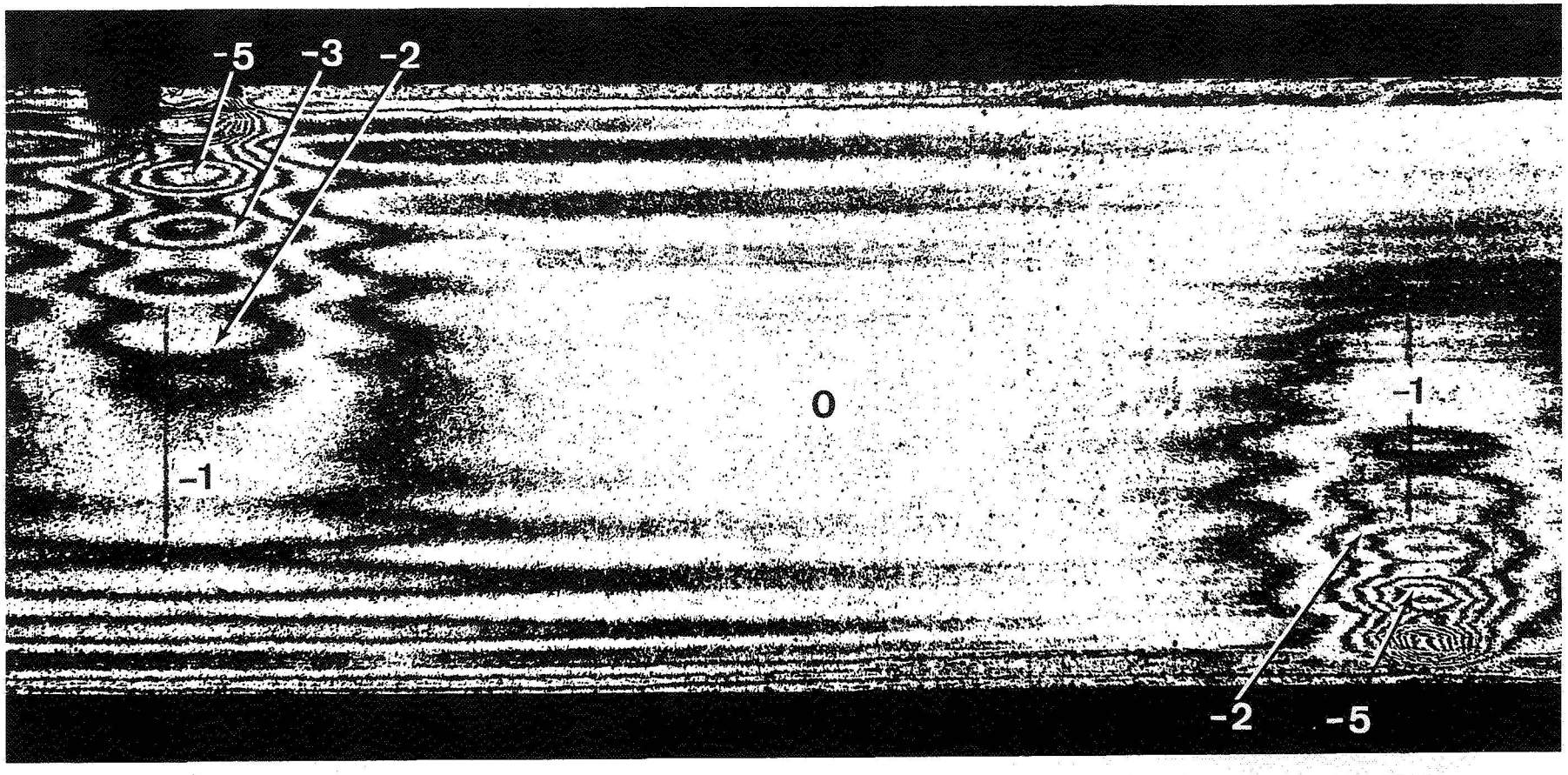

Fig. 17j Pattern of ε_z or $\Delta W/\Delta z$ by mechanical differentation; Δz = 0.010 in.; P/P_f = 36%. The numbers are fringe orders which specify ε_z when multiplied by 0.00167 m/m.

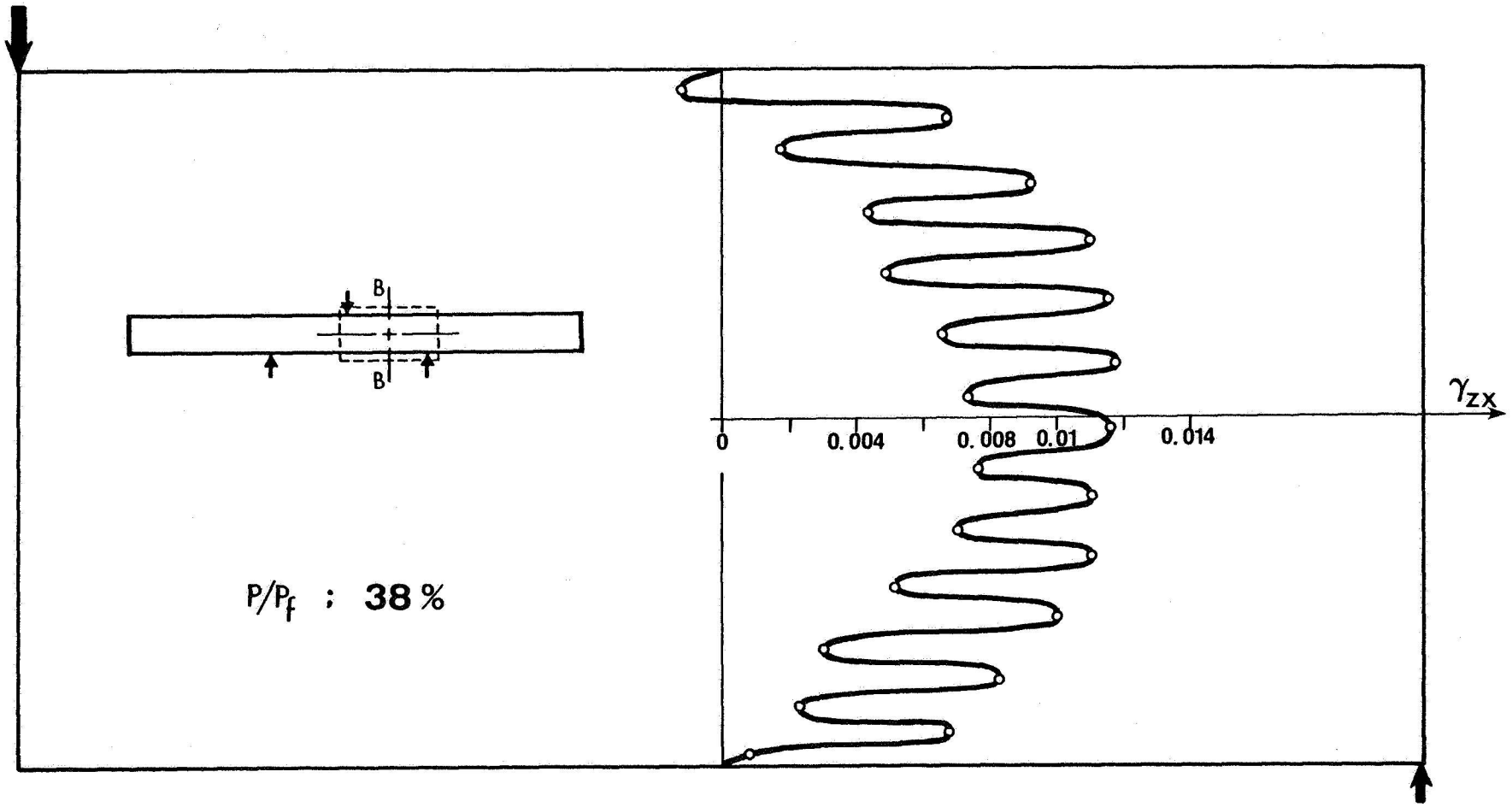

Fig. 18 Shear stresses from Figs. 16a and 16b along vertical centerline B-B of bay, showing the anomalous effect of cyclic fringe gradients in U displacement fields for the quasi-isotropic specimens. The corresponding smoothed graph is shown in Fig. $16e_1$.

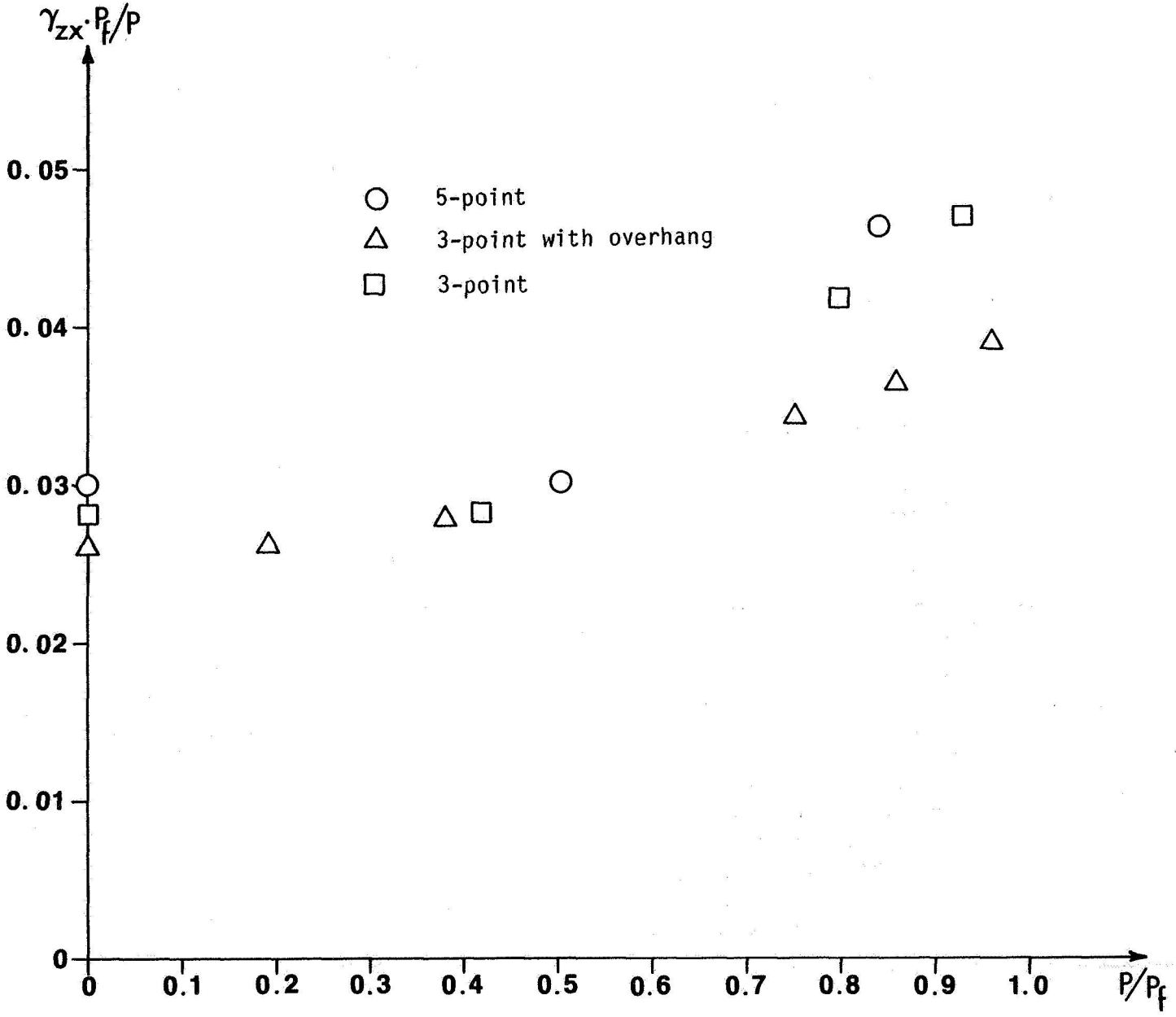

Fig. 19a Shear strains (normalized) at the center of the bay (the bay adjacent to the central load) vs. load level. Unidirectional composite.

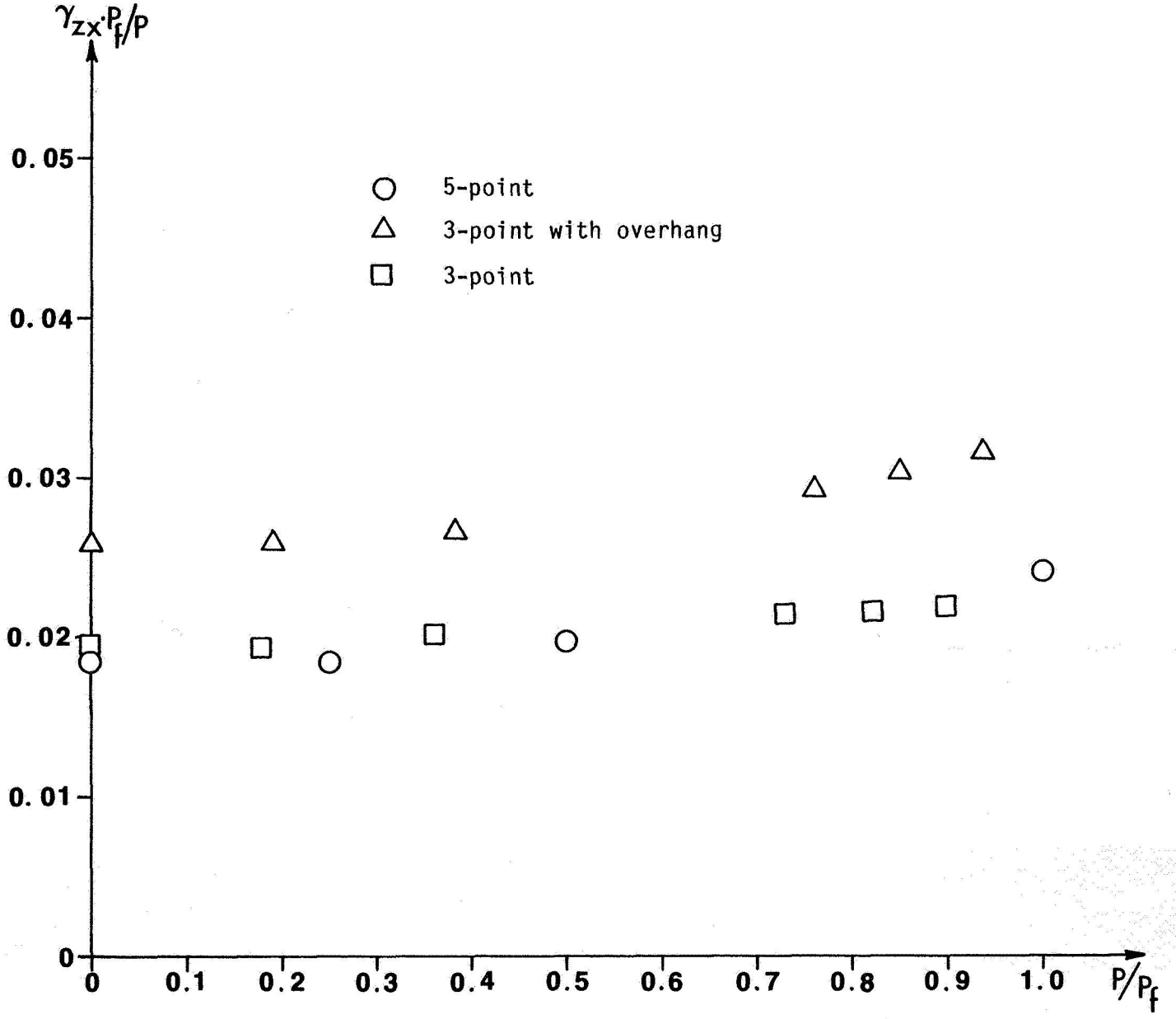

Fig. 19b Shear strains (normalized) at the center of the bay (the bay adjacent to the central load) vs. load level. Quasi-isotropic composite.

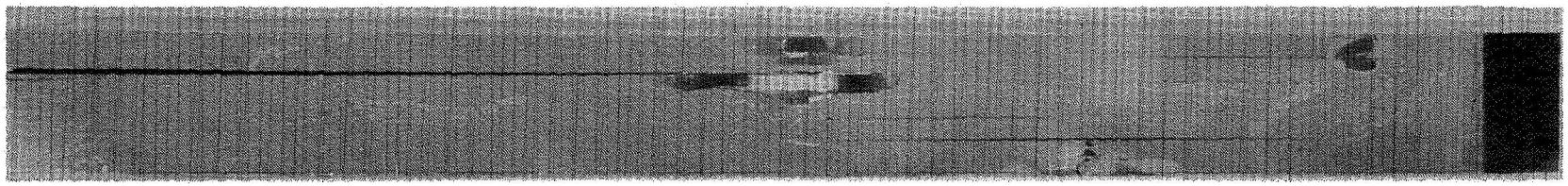

Unidirectional, 5-point

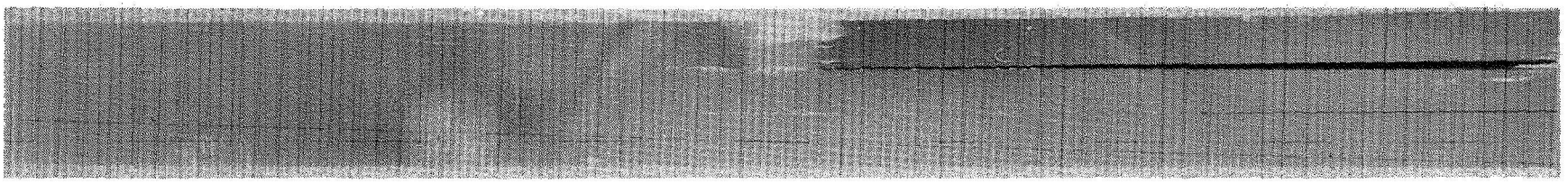

Unidirectional, 3-point with overhang

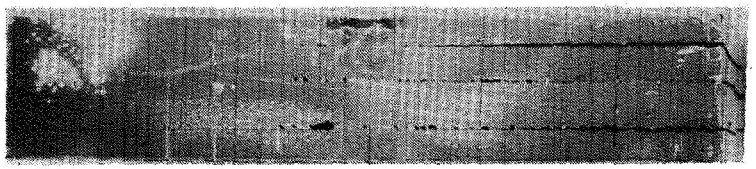

Unidirectional, 3-point

Fig. 20a Edge view of specimen after failure.

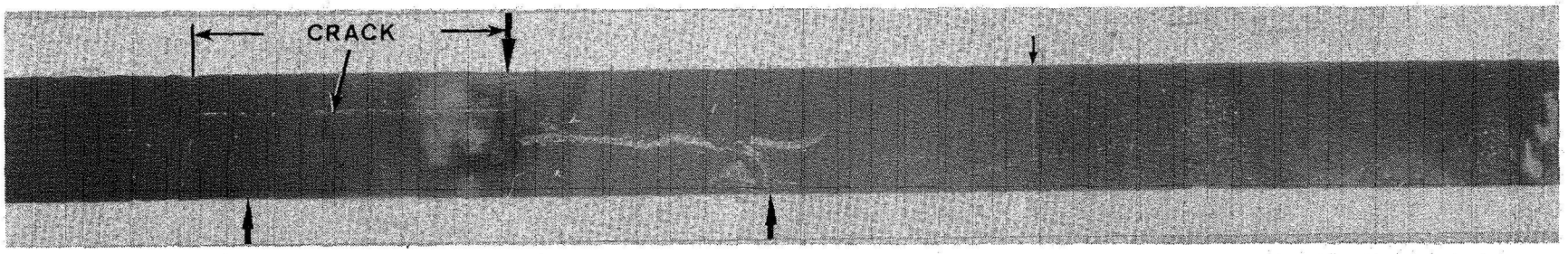

Quasi-isotropic, 5-point

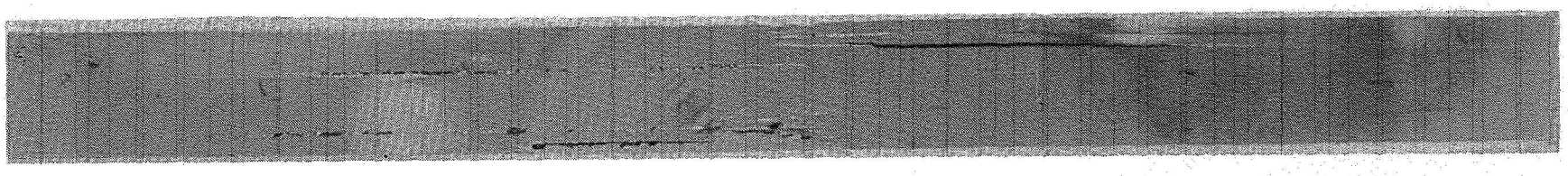

Quasi-isotropic, 3-point with overhang

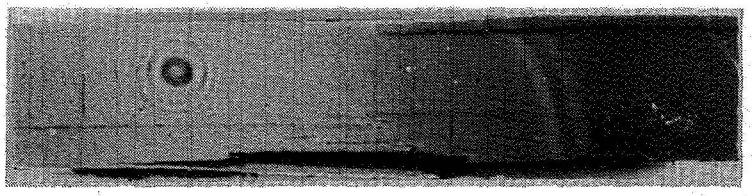

Quasi-isotropic, 3-point

Fig. 20b Edge view of specimen after failure.

Fig. 21a Microphotograph of cross-section of specimen W 36-5 (unidirectional fibers, 5-point loading) showing resin-rich zones.

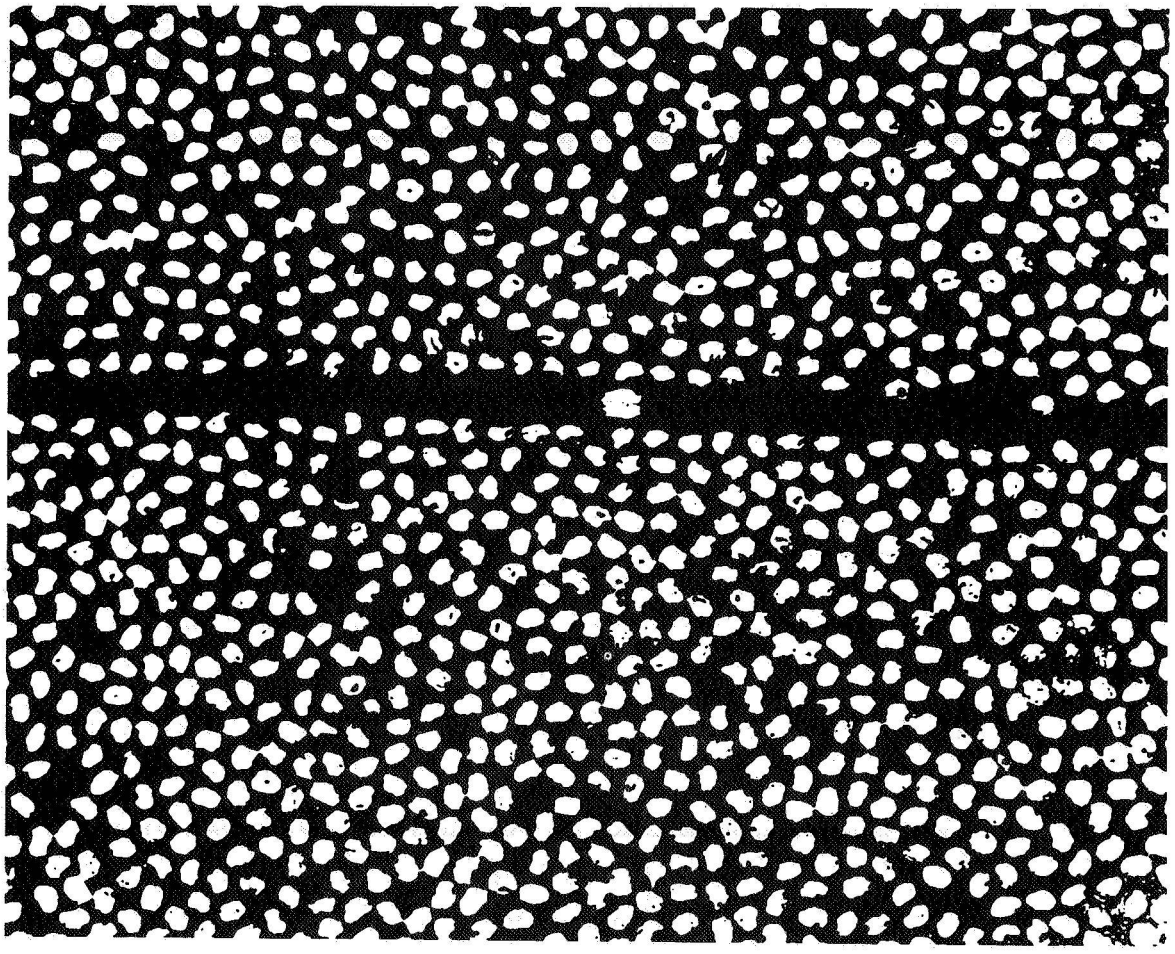

Fig. 21b Microphotograph with higher magnification.

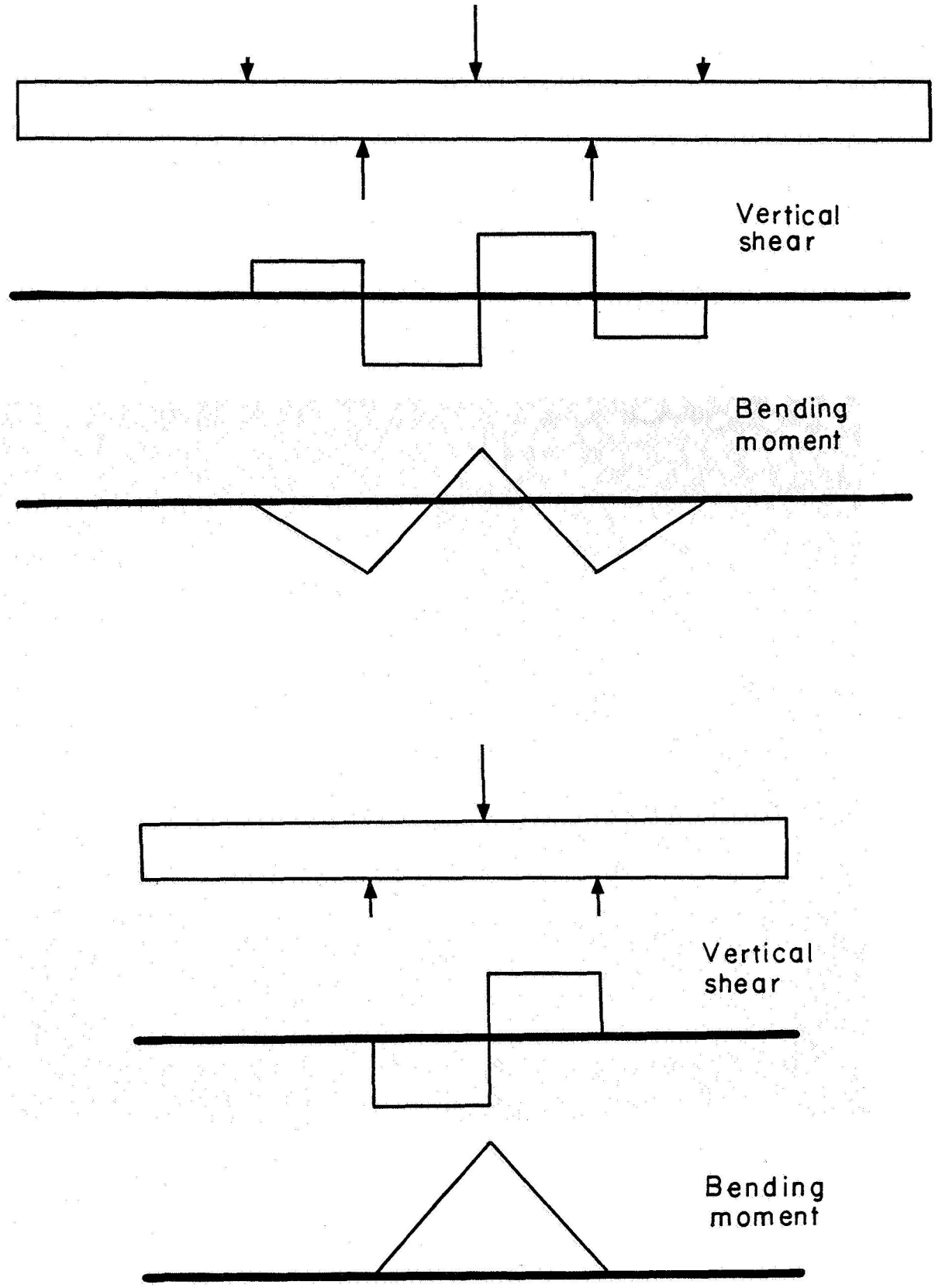

Fig. 22 Bending moment and vertical shear diagrams for 5-point and 3-point beam loadings.

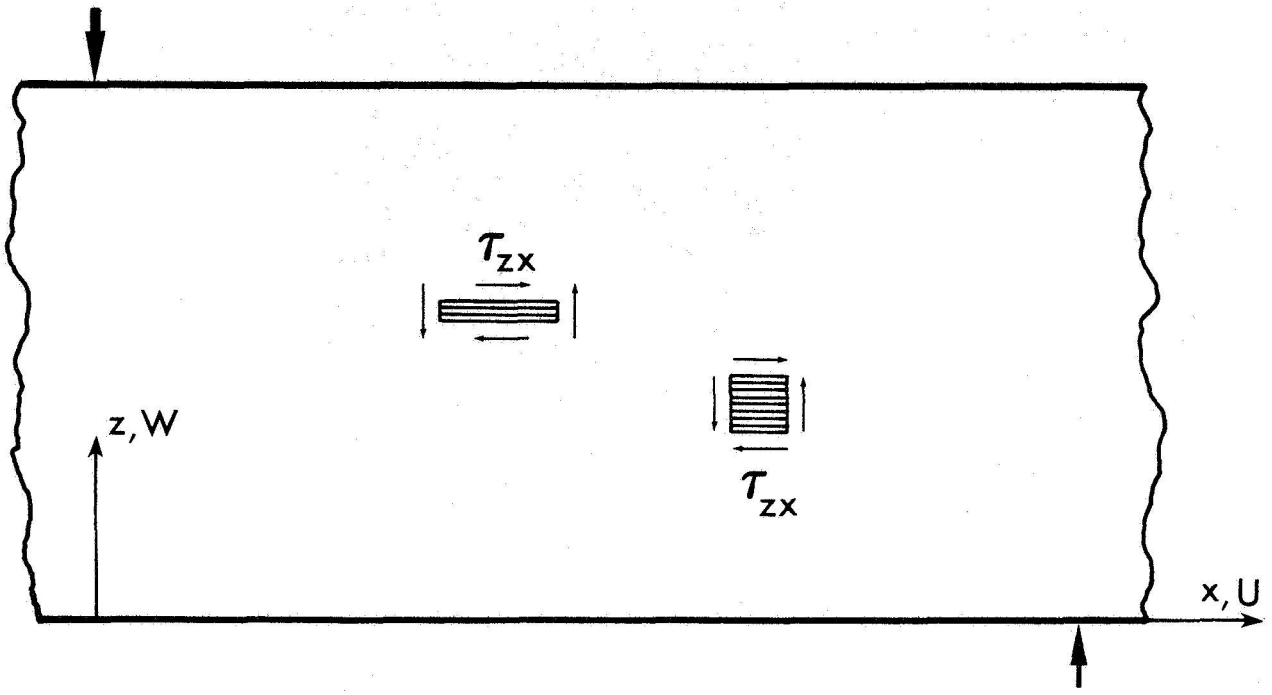

Fig. 23 Shear stresses acting on xy planes have a common sign throughout the bay (in the absence of anomalous effects).

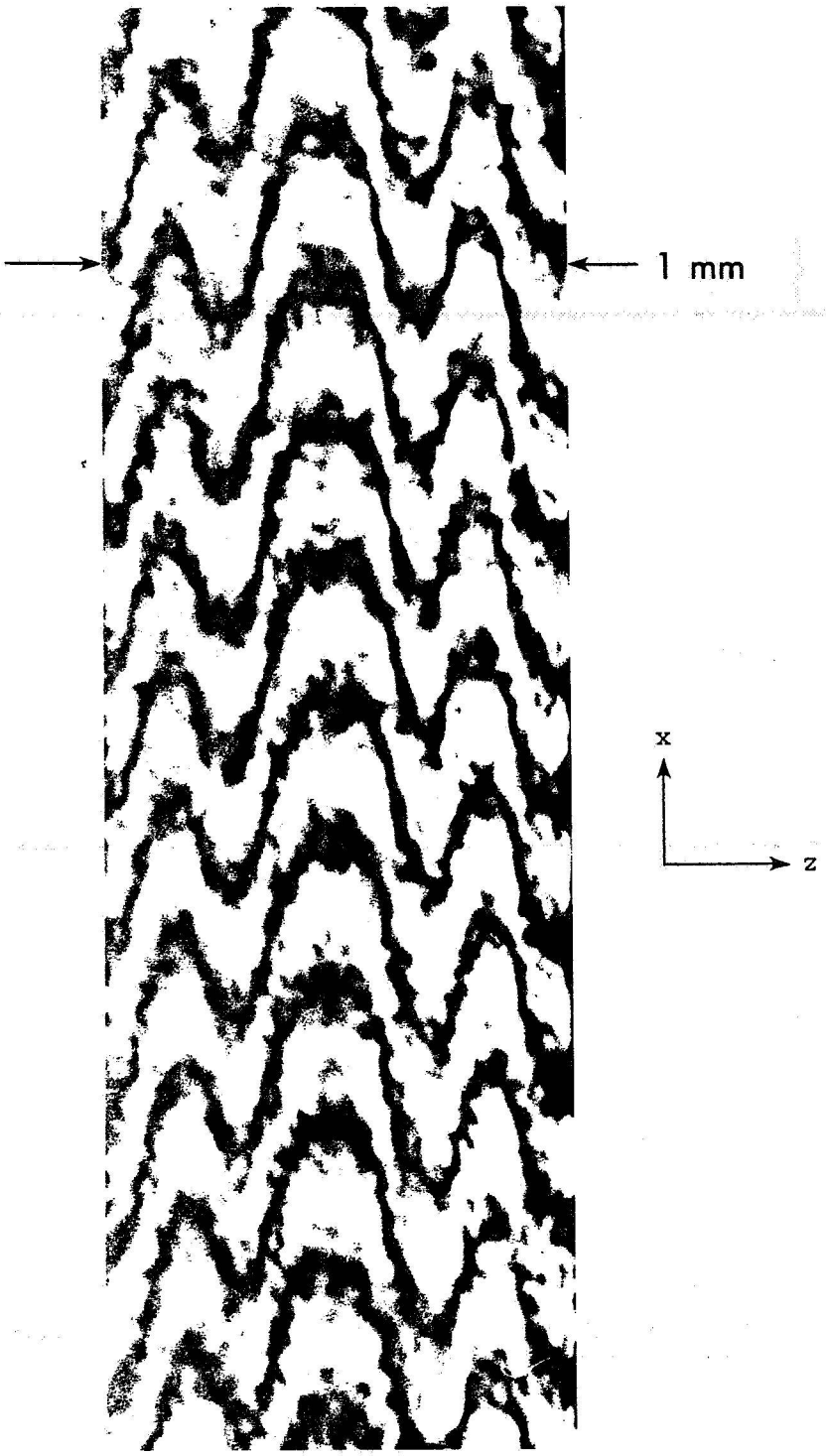

Fig. 24 U displacement field on the free edge of a graphite-epoxy $[30/-30]_{2s}$ specimen in tension. The slope of fringes at the interface between crossed plies is proportional to $\gamma_{zx}/\varepsilon_x$.

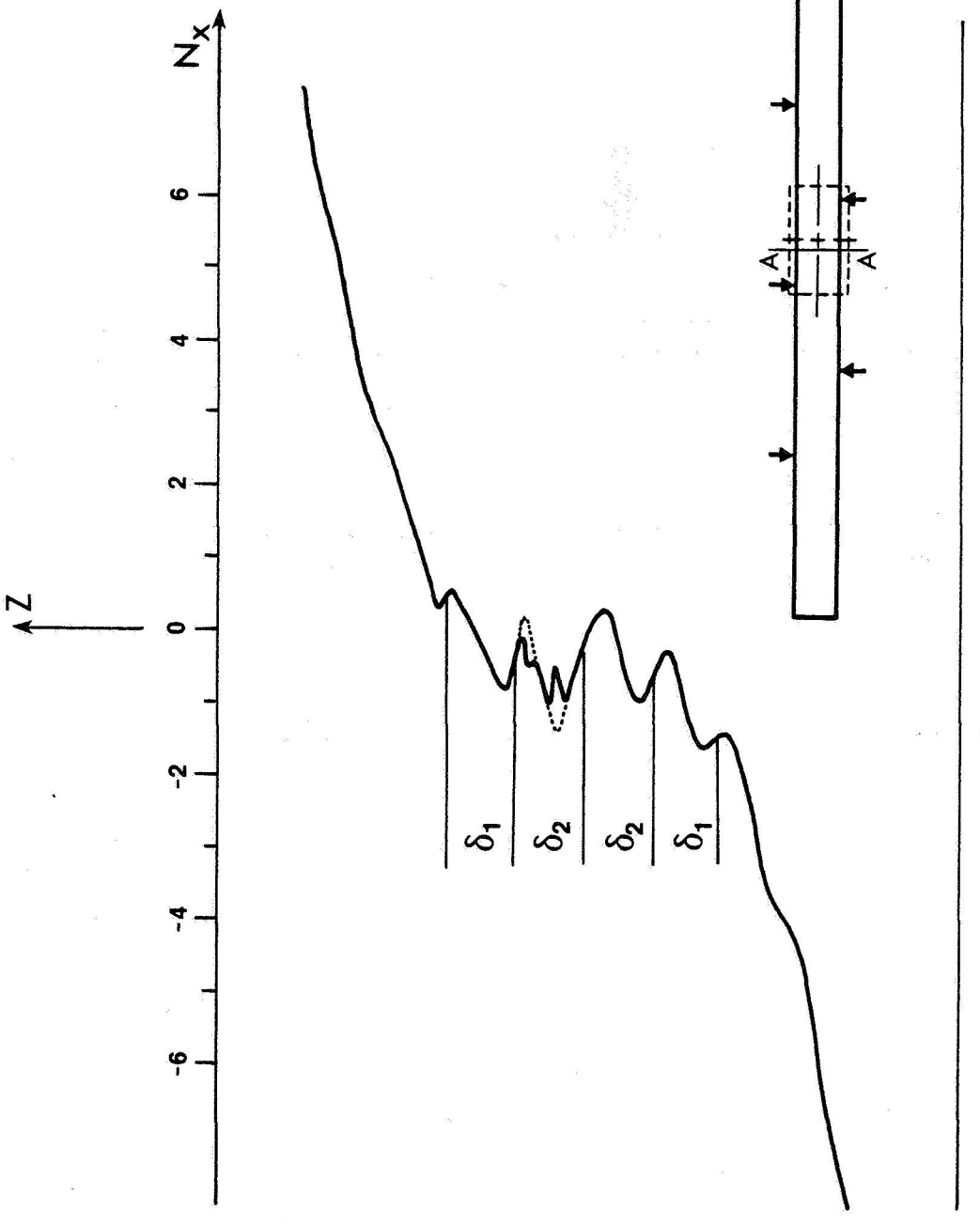

Fig. 25 Fringe order N_x in Fig. 15a vs. z for section A-A of nominally zero ϵ_x.

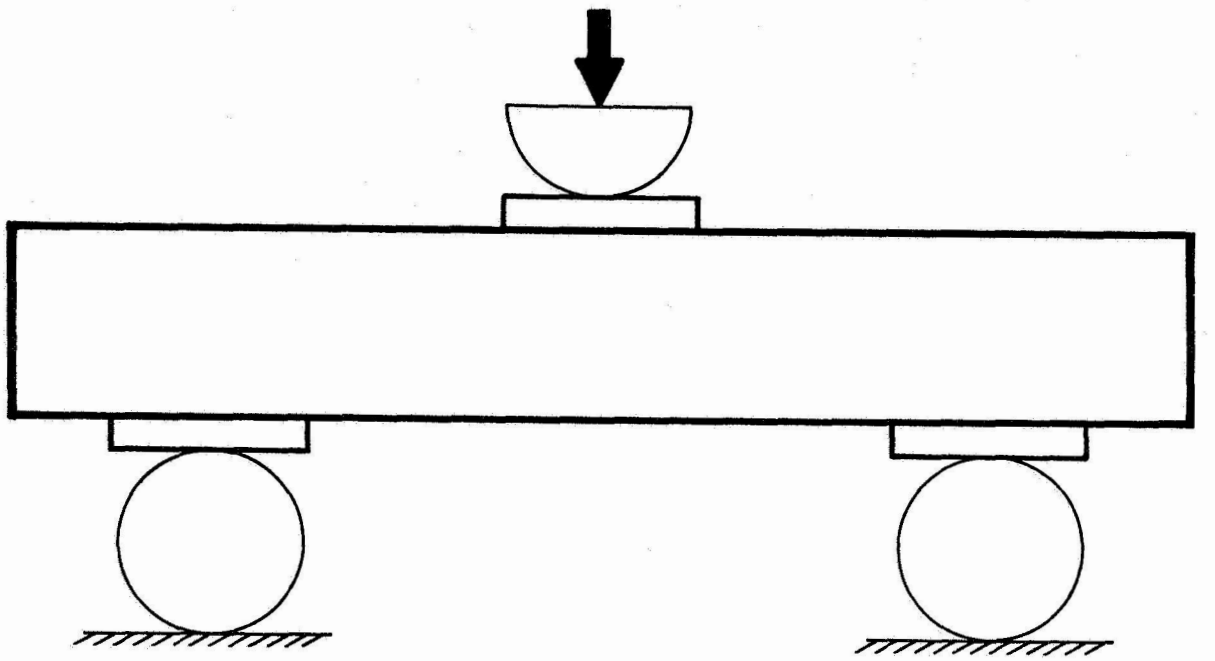

Fig. 26. Loading arrangement to distribute contact pressures.

1. Report No.	2. Government Accession No.	3. Recipient's Catalog No.
NASA CR-3844		

4. Title and Subtitle	5. Report Date
DEFORMATION MEASUREMENTS OF COMPOSITE MULTI-SPAN BEAM SHEAR SPECIMENS BY MOIRE INTERFEROMETRY	November 1984
	6. Performing Organization Code

7. Author(s)	8. Performing Organization Report No.
Daniel Post, Robert Czarnek, Duksung Joh, and Judy Wood	
	10. Work Unit No.

9. Performing Organization Name and Address	11. Contract or Grant No.
Virginia Polytechnic Institute & State University Engineering Science & Mechanics Dept. Blacksburg, VA 24061	NAG1-359
	13. Type of Report and Period Covered
12. Sponsoring Agency Name and Address	Contractor Report
National Aeronautics and Space Administration Washington, D.C. 20546	14. Sponsoring Agency Code
	534-06-23-08

15. Supplementary Notes

Langley Technical Monitor: Jerry G. Williams
Final Report

16. Abstract

Experimental analyses were performed for determination of in-plane deformations and shear strains in unidirectional and quasi-isotropic graphite-epoxy beams. Forty-eight ply beams were subjected to 5-point and 3-point flexure. Whole-field measurements were recorded at load levels from about 20% to more than 90% of failure loads.

Contour maps of U and W displacement fields were obtained by moire interferometry, using reference gratings of 2400 lines/mm or 60,960 ℓ/in. Clearly defined fringes with fringe orders exceeding 1000 were obtained. Whole-field contour maps of shear strains were obtained by a method developed for these tests.

Various anomalous effects were detected in the displacement fields. Their analysis indicated excess shear strains in resin-rich zones in regions of shear tractions; free-edge shear strains in quasi-isotropic specimens in regions of normal stresses; and shear stresses associated with cyclic shear compliances of quasi-isotropic plies in regions of shear tractions. Their contributions could occur independently or in superposition.

Qualitative analyses addressed questions of relaxation; influence of contact stress distribution; specimen failure; effect of specimen overhang; nonlinearity; and qualities of 5 and 3-point flexure tests.

17. Key Words (Suggested by Author(s))	18. Distribution Statement
Composites Graphite/epoxy Beam shear specimens Unidirectional quasi-isotropic Shear strains Anomalous effects Cyclic shear compliance Moire interferometry Displacement fields	Unclassified - Unlimited Subject Category 24

19. Security Classif. (of this report)	20. Security Classif. (of this page)	21. No. of Pages	22. Price*
Unclassified	Unclassified	98	A05

* For sale by the National Technical Information Service, Springfield, Virginia 22161 NASA-Langley, 1984